One-dimensional topological superconductors with nonsymmorphic symmetries

Max Tymczyszyn and Edward McCann*

Physics Department, Lancaster University, Lancaster, LA1 4YB, UK

We present example four-band Hermitian tight-binding Bogoliubov-de-Gennes (BdG) Hamiltonians and Kramer's degenerate Hamiltonians in one dimension. Starting from a generalized Rice–Mele model, we incorporate superconducting terms to obtain a four-band BdG Hamiltonian with intrinsic charge-conjugation symmetry, and constrain it using symmorphic or nonsymmorphic time-reversal symmetries. In position space we find that each form of time-reversal symmetry, when applied to random BdG matrices, results in a unique block diagonalization of the Hamiltonian when translational symmetry is also enforced. We provide representative models in all relevant symmorphic symmetry classes, including the non-superconducting CII class. For nonsymmorphic time-reversal symmetry, we identify a $\mathbb{Z}_4$ topological index with two phases supporting Majorana zero modes and two without, and study disorder effects in the presence of topological solitons. We further generalize a winding-number method, previously applied only to $\mathbb{Z}_2$ invariants without Kramer's degeneracy, to compute indices for both the $\mathbb{Z}_4$ model and a non-superconducting AII model with nonsymmorphic chiral symmetry and Kramer's degeneracy. We propose topolectric circuit implementations of the charge-density-wave and $\mathbb{Z}_4$ models which agree with the topological calculations. Finally, we show that, in one dimension, nonsymmorphic unitary symmetries do not produce new topological classifications beyond $\mathbb{Z}$ or $\mathbb{Z}_2$ indices.

I. INTRODUCTION

Topological superconductors are a central focus of condensed matter research [1–9], with models such as the Kitaev chain [1] guiding the pursuit of experimentally realizable non-trivial superconducting phases [10]. Of particular interest are Majorana zero modes (MZM), topologically protected zero-energy modes localized at the ends of a superconducting chain [1, 6–8, 11], which are promising candidates for fault-tolerant qubits [3, 12]. This prospect has driven extensive theoretical [2–5, 13] and experimental efforts on systems such as nanowires [14–16] and magnetic atom chains [17–19] that are primarily investigated through scanning tunneling microscopy [17–20].

The topological properties of superconductors may be categorized according to the ten-fold way classification of nonunitary symmetries [11, 21–27], specifically, time-reversal symmetry (TRS), charge conjugation symmetry, and chiral symmetry, as shown in Table I [21, 28]. Recent work has included crystalline symmetries in this classification, leading to new topological invariants and protected states [29–31]. Crystalline symmetries may also mimic nonunitary ones, expanding the ten-fold way without requiring that the Hamiltonian satisfies further nonunitary transformations [28, 32–38]. A particularly important example of this in one dimension is the comparison between the symmorphic Su-Schrieffer-Heeger (SSH) model [39–43], with alternating hopping parameters, and the nonsymmorphic charge-density-wave (CDW) model [39, 44–48], with constant hopping and alternating onsite energy. The SSH and CDW models can be considered as different phases of the Rice-Mele model [39, 49], which has both alternating hoppings and onsite energies. The SSH model is defined by its symmorphic symmetries that act locally within a unit cell, resulting in a $\mathbb{Z}$ topological index. Surprisingly, the CDW model has nonsymmorphic symmetries that involve a translation by half a unit cell, and mimic the nonunitary charge conjugation and chiral symmetries of the SSH model [44–46, 50–61], resulting in a $\mathbb{Z}_2$ topological index.

TABLE I. Altland-Zirnbauer classification of one-dimensional BdG Hamiltonians in Nambu space with built-in charge conjugation and the Kramer's degenerate AII and CII classes [21, 28]. T^2, C^2, and S^2 represent the form of time reversal, charge conjugation, and chiral symmetry, respectively, where the label 'NS' represents a nonsymmorphic symmetry and the column 'index' lists the form of topological superconductor or insulator for each model.

Class	T^2	C^2	S^2	Index
D	0	1	0	$\mathbb{Z}_2$
BDI	1	1	1	$\mathbb{Z}$
CII	-1	-1	1	$2\mathbb{Z}$
DIII	-1	1	1	$\mathbb{Z}_2$
AII	-1	NS	NS	$\mathbb{Z}_2$
D	NS	1	NS	$\mathbb{Z}_4$

While example topological models for most symmetry classes in one spatial dimension can be realized with two bands [61], models with Kramer's degeneracy require at least four. A simple way to obtain four bands is to write the Hamiltonian in the Bogoliubov-de-Gennes (BdG) representation, which naturally enforces charge conjugation as a 'built-in' symmetry that ensures superconductivity [7, 8, 62–64]. BdG classes can be differentiated by their bulk topology, where varying symmetry combinations result in different topological indices, Table I, and also by energy level statistics, where varying TRS results in the distribution of energy levels changing

* ed.mccann@lancaster.ac.uk

between different statistical ensembles [6, 65–68].

In this paper, we distinguish the BdG classes in Table I using both the level statistics of large random matrices, and also by identifying example four-band models in each class, and calculating their corresponding topological index. Since nonsymmorphic TRS involves a translation of half a unit cell, applying the operation twice yields a unitary translational symmetry. In symmorphic models such a translational symmetry can also be applied arbitrarily. The presence of translational symmetry enables block diagonalization of large random matrices, with each block belonging to a different statistical ensemble. The specific combination of these blocks depends on the global form of TRS in the matrix, which provides a way to distinguish topological classes. By imposing only translational symmetry on nonsymmorphic matrices, we separate the classes by analyzing the ratio of consecutive level spacings [69, 70], with distributions belonging to different statistical ensembles depending on the overall TRS of the matrix.

We then build example models in each of the classes and calculate their respective topological indices, including the non-superconducting nonsymmorphic AII class, the topological indices of which are shown in Table I [21, 28]. While the topology of the symmorphic classes is understood, we include example models to introduce the concepts used in the topological calculations of the nonsymmorphic AII class, which has not been previously discussed, and the nonsymmorphic $\mathbb{Z}_4$ index described in Ref. [71]. Specifically, we generalize the winding number from the BDI class, e.g. the SSH model, for nonsymmorphic chiral symmetry [44, 45], a method previously only used for non-Kramer's degenerate systems such as the CDW model. We further investigate the $\mathbb{Z}_4$ model due to its unique topology for noninteracting models in one-dimension to understand the role of disorder in the presence of solitons between its phases. We find that, although the nonsymmorphic symmetries are broken by disorder, solitons remain robust in a system with only nearest-neighbor hopping parameters due to additional symmorphic symmetries being satisfied exactly at the domain wall.

It has been found that topological models may be physically emulated by simple RLC circuits known as 'topolectric' circuits [72–78]. We extend the topolectric circuit methodology to nonsymmorphic systems, drawing comparison between the SSH and CDW model, and the Kitaev and $\mathbb{Z}_4$ chains. We find that the circuits agree with the topological theory, and allow for an experimentally measurable quantity (impedance) to be easily observed. Finally, we show that, in one dimension, the topology predicted by Ref. [28] for systems with an additional nonsymmorphic unitary symmetry is equivalent to that of the two-band models described in Ref. [61].

To build the random matrices and example models, we first construct a four-band BdG Hamiltonian [6–8, 62–64] that acts as two charge-conjugation partnered Rice-Mele chains coupled by superconducting order parameters. The terms of this Hamiltonian may have infinite range, such that all possible complex-valued parameters consistent with Hermicity are included. We then constrain this system through the application of various forms of TRS, resulting in four topological classes, including the $\mathbb{Z}_4$ class with nonsymmorphic TRS. To realize the non-superconducting CII and AII classes we build a model with similar structure to the BdG Hamiltonians, but with different forms of the charge-conjugation symmetry.

Our results are summarized in Table I according to the ten-fold way classification [21, 28]. The first column denotes the Cartan label of the symmetry class. Time-reversal, charge-conjugation, and chiral symmetry are denoted by the columns labeled T^2, C^2, and S^2, respectively, where a zero indicates an absence of symmetry and "NS" indicates a nonsymmorphic symmetry. For the nonsymmorphic classes we adopt the convention of Ref. [28], where the nonsymmorphic symmetry is treated as absent for the purposes of assigning a Cartan label. The final column of Table I represents the topological index of the superconductor or insulator for each member of the class. We find that the symmorphic D class has a $\mathbb{Z}_2$ index represented by a Majorana number [1], the BDI class by a $\mathbb{Z}$ integer winding number [11, 25, 27], the DIII class by a $\mathbb{Z}_2$ Fermi surface topological invariant [24, 26, 79, 80], and the non-superconducting CII class is defined by an even $2\mathbb{Z}$ winding number [11, 81]. The nonsymmorphic D class has a $\mathbb{Z}_4$ index [71] described by a Majorana number and two further phase transitions with conditions depending on the sign of the Majorana number, and the nonsymmorphic AII class has a $\mathbb{Z}_2$ invariant [28]. Both of these nonsymmorphic indices can be calculated with a generalized winding number [44, 45], the $\mathbb{Z}_4$ index may also be calculated using an equivalent integral formalism [28, 71]. Example paths of the generalized winding number for the $\mathbb{Z}_4$ model are shown for each of the four phases in Fig. 1.

In Sec. II we describe the generalized Rice-Mele model with added superconducting parameters and the construction of the BdG Hamiltonian. Sec. III describes the forms of symmorphic and nonsymmorphic symmetries applied to the Hamiltonian to constrain the system in both k-space and position space. In Sec. IV we build random matrices in position space with various forms of TRS. We then introduce an example model and calculate its topology for each of the symmorphic D, BDI, DIII, and CII classes in Sec. V, and the nonsymmorphic AII and $\mathbb{Z}_4$ classes in Sec. VI and Sec. VII, respectively. For the $\mathbb{Z}_4$ class we also add disorder in the presence of solitons in Sec. VII D. With the exception of class CII we do not explore in detail models belonging to the C classes with $C^2 = -1$, as these models are typically topologically trivial for both symmorphic and nonsymmorphic symmetries, and have been cataloged in Ref. [61]. We show in the supplementary material [82] that the $2\mathbb{Z}$ index of the CII class is destroyed in the presence of a nonsymmorphic unitary symmetry that anticommutes with the chi-

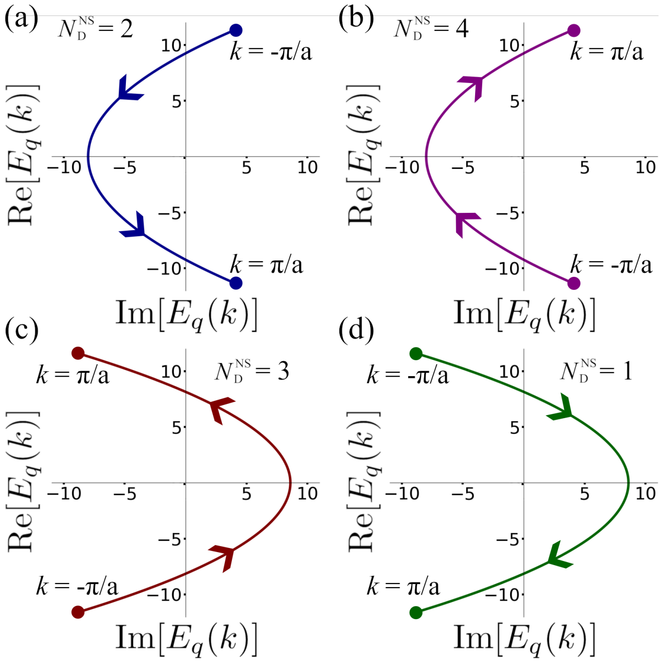

FIG. 1. Four distinct topological phases of the $\mathbb{Z}_4$ model in the nonsymmorphic D class, displayed as example trajectories of the winding path $E_q(k)$, Eq. (35), across the Brillouin zone $-\pi/a \leq k < \pi/a$. (a) Shows a trajectory in the phase $N_{\rm D}^{\rm NS} = 2$, and (b) a trajectory in the phase $N_{\rm D}^{\rm NS} = 4$. Both (a) and (b) have parameter values $v = 0.5$, $\Delta_s = 1$, and $\phi_s = \pi/4$, they are distinguished as for (a) $\mu = -1$ and for (b) $\mu = 1$. (c) Shows a trajectory in the phase $N_{\rm D}^{\rm NS} = 3$, and (d) a trajectory in the phase $N_{\rm D}^{\rm NS} = 1$. Both (c) and (d) have parameter values $\mu = 1.7$, $v = 1.2$, and $\Delta_s = 0.6$, they are distinguished as for (c) $\phi_s = 3\pi/4$ and for (d) $\phi_s = \pi/4$. It is possible to adiabatically deform the parameters such that the path in (a) may resemble the path in (b) without causing a phase transition, however, a change in sign of μ as displayed here must cause a transition between the two paths. A similar statement is true for a change in the sign of $\cos(\phi_s)$ between the paths in (c) and (d).

ral symmetry operator. As it is also topologically trivial, we do not write out an example model for the symmorphic AII class in this paper. A theoretical realization of nonsymmorphic topology is included in Sec. VIII in the form of topolectric circuits. Finally, in Sec. IX we show that additional nonsymmorphic unitary symmetries do not create novel topology.

II. MODEL

We consider a generalized Rice-Mele model with constant chemical potential and alternating on-site energies, in addition to both s- and p-wave superconducting order parameters. There are two orbitals per unit cell denoted A and B, which may be interpreted as spin labels $\uparrow$ and $\downarrow$ for spinful fermions, which will give four components in the BdG representation. The lattice constant is a, with an additional distance s between the A and B atoms within the same unit cell. In position space the Hamiltonian with nearest-neighbor hopping parameters takes the form

$$\begin{aligned}\mathcal{H}=\sum_j \Big[&(-\mu+u)c^\dagger_{\alpha,j}c_{\alpha,j}+(-\mu-u)c^\dagger_{\beta,j}c_{\beta,j}\\ &+t_{AA}e^{i\phi_{AA}}c^\dagger_{\alpha,j}c_{\alpha,j+1}+t_{BB}e^{\phi_{BB}}c^\dagger_{\beta,j}c_{\beta,j+1}\\ &+ve^{i\phi_v}c^\dagger_{\alpha,j}c_{\beta,j}+we^{i\phi_w}c^\dagger_{\beta,j}c_{\alpha,j+1}+t_3e^{i\phi_3}c^\dagger_{\alpha,j}c_{\beta,j+1}\\ &+\Delta_s e^{i\phi_s}c^\dagger_{\alpha,j}c^\dagger_{\beta,j}+\Delta'_s e^{i\phi'_s}c^\dagger_{\beta,j}c^\dagger_{\alpha,j+1}+\check{\Delta}_s e^{i\check{\phi}_s}c^\dagger_{\alpha,j}c^\dagger_{\beta,j+1}\\ &+\Delta_p e^{i\phi_p}c^\dagger_{\alpha,j}c^\dagger_{\alpha,j+1}+\Delta'_p e^{i\phi'_p}c^\dagger_{\beta,j}c^\dagger_{\beta,j}+\text{H.c.}\Big], \end{aligned} \tag{1}$$

where μ is the chemical potential and u is an onsite energy, t_{AA}, t_{BB}, v, w and t_3 are tight binding parameters, Δ_s, Δ'_s, and $\check{\Delta}_s$, are s-wave superconducting order parameters, Δ_p and Δ'_p are p-wave superconducting order parameters, and H.c. represents the Hermitian conjugate terms. For a finite system with J orbitals we can write the Hamiltonian as a $2J \times 2J$ BdG matrix, e.g., for four orbitals in the 'ladder' basis $\Psi^\dagger = \begin{pmatrix} c^\dagger_{\alpha,1} & c^\dagger_{\beta,1} & c_{\alpha,1} & c_{\beta,1} & c^\dagger_{\alpha,2} & c^\dagger_{\beta,2} & c_{\alpha,2} & c_{\beta,2}\end{pmatrix}$ the Hamiltonian is

$$\mathcal{H} = \Psi^\dagger \begin{pmatrix} \hat{h}_1 & \hat{\Delta}_1 & \hat{h}_2 & \hat{\Delta}_2 \\ \hat{\Delta}_1^\dagger & -\hat{h}_1^* & -\hat{\Delta}_2^* & -\hat{h}_2^* \\ \hat{h}_2^\dagger & -\hat{\Delta}_2^T & \hat{h}_1 & \hat{\Delta}_1 \\ \hat{\Delta}_2^\dagger & -\hat{h}_2^T & \hat{\Delta}_1^\dagger & -\hat{h}_1^* \end{pmatrix} \Psi + \mathrm{Tr}\left[\,\hat{h}_1\,\right], \tag{2}$$

where

$$\hat{h}_1 = \begin{pmatrix} -\mu+u & ve^{i\phi_v} \\ ve^{-i\phi_v} & -\mu-u \end{pmatrix}, \qquad \hat{\Delta}_1 = \begin{pmatrix} 0 & \Delta_s e^{i\phi_s} \\ -\Delta_s e^{i\phi_s} & 0 \end{pmatrix},$$

$$\hat{h}_2 = \begin{pmatrix} t_{AA}e^{i\phi_{AA}} & t_3 e^{i\phi_3} \\ we^{i\phi_w} & t_{BB}e^{i\phi_{BB}} \end{pmatrix}, \quad \hat{\Delta}_2 = \begin{pmatrix} \Delta_p e^{i\phi_p} & \check{\Delta}_s e^{i\check{\phi}_s} \\ \Delta'_s e^{i\phi'_s} & \Delta'_p e^{i\phi'_p} \end{pmatrix}.$$

We can write the Hamiltonian (2) in the BdG representation $\mathcal{H} = \frac{1}{2}\sum_k \Psi_k^\dagger H(k)\Psi_k + \frac{1}{2}\sum_k \mathrm{tr}(\hat{h}(k))$ where $\Psi_k^\dagger = \begin{pmatrix} c^\dagger_{\alpha,k} & c^\dagger_{\beta,k} & c_{\alpha,-k} & c_{\beta,-k}\end{pmatrix}$ for wave vector k and where the 4×4 Bloch Hamiltonian is

$$\begin{aligned} H(k) &= \begin{pmatrix} \hat{h}(k) & \hat{\Delta}(k) \\ \hat{\Delta}^\dagger(k) & -\hat{h}^T(-k) \end{pmatrix}, \\ \hat{h}(k) &= \begin{pmatrix} h_1(k) & h_2(k) \\ h_2^*(k) & h_3(k) \end{pmatrix}, \\ \hat{\Delta}(k) &= \begin{pmatrix} \Delta_1(k) & \Delta_2(k) \\ -\Delta_2(-k) & \Delta_3(k) \end{pmatrix}, \end{aligned} \tag{3}$$

where $h_1(k)$, $h_2(k)$, and $h_3(k)$ can take generic forms [61] consistent with Hermicity,

$$\begin{aligned} h_1(k) =& -\mu+u+2t_{AA}\cos(ka+\phi_{AA}), \\ h_2(k) =& v\left(\cos(ks+\phi_v)+i\sin(ks+\phi_v)\right) \\ &+w(\cos(k(a-s)+\phi_w)-i\sin(k(a-s)+\phi_w)) \\ &+t_3\left(\cos(k(a+s)+\phi_3)+i\sin(k(a+s)+\phi_3)\right), \\ h_3(k) =& -\mu-u+2t_{BB}\cos(ka+\phi_{BB}). \end{aligned}$$

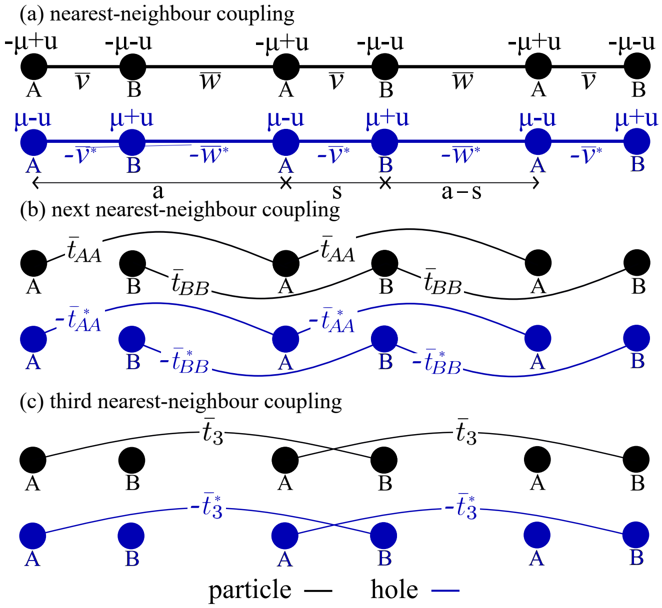

FIG. 2. The tight binding parameters of two generalised Rice-Mele model chains in parallel, where the upper chain (black) represents an electron space, and the lower chain (blue) represents a hole space. (a) Nearest-neighbor couplings with constant chemical potential $\pm\mu$, staggered onsite energy $\pm u$, and staggered hoppings $\pm v$ and $\pm v$ between adjacent A and B orbitals. The lattice constant is a, and a B orbital is located at intracell distance s to the right of an A orbital. (b) Next-nearest-neighbor coupling $\pm t_{AA}$ between A orbitals and $\pm t_{BB}$ between B orbitals. (c) Third-nearest-neighbor coupling $\pm t_3$ between an A orbital and the second B orbital to its right. Bars over parameters indicate that they are complex numbers, in general.

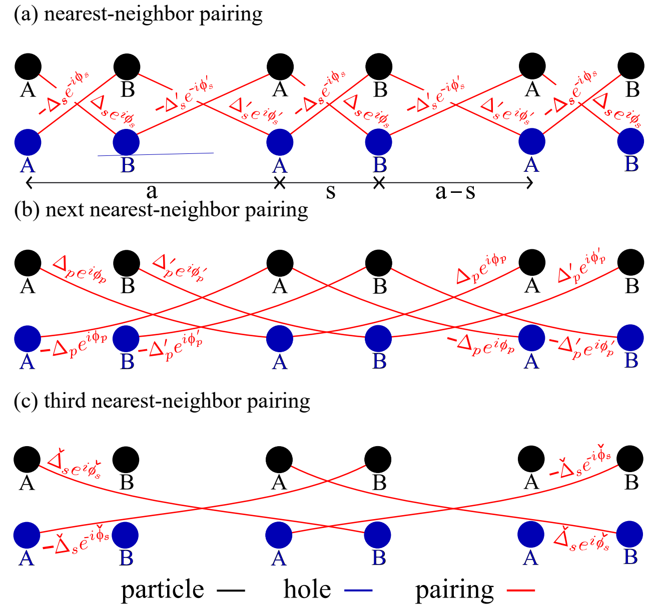

FIG. 3. The superconducting pairing parameters between two generalized Rice-Mele model chains in parallel, where the upper chain (black) represents an electron space, the lower chain (blue) represents a hole space, and lines between them (red) represent superconducting pairings. (a) Nearest-neighbor pairings with order parameter magnitudes Δ_s and Δ'_s between adjacent A and B orbitals with phases ϕ_s and ϕ'_s. The lattice constant is a, and a B orbital is located at intracell distance s to the right of an A orbital. (b) Next-nearest-neighbor order parameter magnitude Δ_p between A orbitals and Δ'_p between B orbitals with phases ϕ_p and ϕ'_p. (c) Third-nearest-neighbor order parameter magnitude $\check{\Delta}_s$ between an A orbital and the second B orbital to its right with phase $\check{\phi}_s$.

The superconducting pairing terms are

$$
\begin{aligned}
\Delta_1(k,s) &= 2i\Delta_p\cos(\phi_p)\sin(ka) - 2\Delta_p\sin(\phi_p)\cos(ka),\\
\Delta_2(k,s) &= \Delta_s\cos(ks+\phi_s) + i\Delta_s\sin(ks+\phi_s)\\
&+ \Delta'_s\cos(k(a-s)-\phi'_s) - i\Delta'_s\sin(k(a-s)-\phi'_s)\\
&+ \check{\Delta}_s\cos(k(a+s)-\check{\phi}_s) + i\check{\Delta}_s\sin(k(a+s)+\check{\phi}_s),\\
\Delta_3(k,s) &= 2i\Delta'_p\cos(\phi'_p)\sin(ka) - 2\Delta'_p\sin(\phi'_p)\cos(ka).
\end{aligned}
$$

As we are not concerned with numerical values of the parameters but only the constraints placed upon them, we do not consider them to be dependent on distances a or s. As such, next nearest-neighbor and third nearest-neighbor parameters are included because they become nearest-neighbor in the limit of intracell spacing $s = 0$. It is also simple to extend the model to infinite range hopping, as detailed in the supplementary material [82]. A schematic of the hopping parameters between atomic sites in the same chain can be found in Fig. 2, and for superconducting pairings between atomic sites in different chains in Fig. 3. The Hamiltonian is in the type I or "periodic" representation for $s = 0$ [39, 83], and the type II "canonical" representation for $s \neq 0$, and can be transformed between the two as

$$
H(k,s) = U_k(k,s)H(k,0)U_k^\dagger(k,s), \tag{4}
$$

where

$$
U_k(k,s) = \begin{pmatrix} e^{iks/4} & 0 & 0 & 0 \\ 0 & e^{-iks/4} & 0 & 0 \\ 0 & 0 & e^{iks/4} & 0 \\ 0 & 0 & 0 & e^{-iks/4} \end{pmatrix}. \tag{5}
$$

By putting the Hamiltonian into the BdG form, Eq. (3), there is now a 'built-in' charge conjugation symmetry imposed by the Pauli exclusion principle. With no further constraints, other than that the Hamiltonian is Hermitian, the Hamiltonian is now in the symmorphic D class, Table I. We can apply different forms of time-reversal and chiral symmetry to further constrain the Hamiltonian.

III. SYMMETRIES

The Hamiltonian (3) may satisfy any of the three nonunitary symmetries of TRS (T), charge conjugation symmetry (C), or chiral symmetry (S), with their respective operations in k-space being

$$\begin{aligned} \text{time}: &\quad U_T^\dagger(k,s)H^*(k,s)U_T(k,s) = H(-k,s), &(6)\\ \text{charge}: &\quad U_C^\dagger(k,s)H^*(k,s)U_C(k,s) = -H(-k,s), &(7)\\ \text{chiral}: &\quad U_S^\dagger(k,s)H(k,s)U_S(k,s) = -H(k,s), &(8)\end{aligned}$$

where U_T, U_C, and U_S are unitary matrices with

$$U_T(k,s)U_T^*(-k,s) = \pm I, \tag{9}$$
$$U_C(k,s)U_T^*(-k,s) = \pm I, \tag{10}$$
$$U_S(k,s)U_S(k,s) = I, \tag{11}$$

written in shorthand as $T^2 = \pm 1$, $C^2 = \pm 1$, and $S^2 = 1$. These operators also obey the relationship $U_S(k,s) = U_C^*(k,s)U_T(-k,s)$. For symmorphic models the symmetry operators U_T, U_C, U_S are independent of k for intracell distance $s = 0$. Conversely, for nonsymmorphic models the operators are independent of k for intracell distance $s = a/2$. Otherwise the operators gain a k dependence according to

$$U_T(k,s) = U_k^\dagger(k,s)U_T(k,0)U_k(k,s), \tag{12}$$
$$U_C(k,s) = U_k^\dagger(k,s)U_C(k,0)U_k(k,s), \tag{13}$$
$$U_S(k,s) = U_k(k,s)U_S(k,0)U_k^\dagger(k,s). \tag{14}$$

Different combinations of these symmetries result in distinct topological classes, Table I. We denote the corresponding index for each symmorphic class as N_n^{S} and for each nonsymmorphic class as N_{CL}^{NS}, where 'CL' indicates the Cartan label of the symmetry class. In k-space, symmetry operators take the form of the tensor product of two Pauli matrices, $\tau_i \otimes \sigma_j$, or in shorthand $\tau_i\sigma_j$, where $i,j = I,x,y,z$ for the identity matrix, and Pauli x, y, and z matrices, respectively, and where τ corresponds to the chain space and σ to the sublattice space. Each form of TRS constrains the parameters of the Hamiltonian in different ways, although these Hamiltonians are related to one another by unitary transformations [61].

In position space the symmetry operations are

$$\text{time}: \quad \mathcal{T}^\dagger H^* \mathcal{T} = H; \quad \mathcal{T}\mathcal{T}^* = \pm I; \tag{15}$$
$$\text{charge}: \quad \mathcal{C}^\dagger H^* \mathcal{C} = -H; \quad \mathcal{C}\mathcal{C}^* = \pm I; \tag{16}$$
$$\text{chiral}: \quad \mathcal{S}^\dagger H \mathcal{S} = -H; \quad \mathcal{S}\mathcal{S} = I; \tag{17}$$

where $\mathcal{T}$, $\mathcal{C}$, and $\mathcal{S}$ are unitary matrices, and $\mathcal{S} = \mathcal{T}^*\mathcal{C}$. For symmorphic models the forms of the symmetry operators in the ladder basis are effectively extensions of their k-space counterparts, such that a given k-space operator $\tau_i\sigma_j$ is represented by a size $2J \times 2J$ matrix

$$S_{ij} = \begin{pmatrix} \tau_i\sigma_j & 0 & \cdots \\ 0 & \tau_i\sigma_j & \cdots \\ \vdots & \vdots & \ddots \end{pmatrix}. \tag{18}$$

The nonsymmorphic symmetries are represented by the inclusion of a translation of $a/2$ [45, 46], which, in position space, is represented as

$$T_{a/2} = \begin{pmatrix} 0&1&0&0&0&0&0&\cdots&0&0&0\\ 0&0&0&0&1&0&0&\cdots&0&0&0\\ 0&0&0&1&0&0&0&\cdots&0&0&0\\ 0&0&0&0&0&0&1&\cdots&0&0&0\\ 0&0&0&0&0&1&0&\cdots&0&0&0\\ \vdots&\vdots&\vdots&\vdots&\vdots&\vdots&\vdots&&\vdots&\vdots&\vdots\\ 0&0&0&0&0&0&0&\cdots&0&1&0\\ 0&0&0&0&0&0&0&\cdots&1&0&0\\ 1&0&0&0&0&0&0&\cdots&0&0&0\\ 0&0&0&0&0&0&0&\cdots&0&0&1\\ 0&0&1&0&0&0&0&\cdots&0&0&0 \end{pmatrix}. \tag{19}$$

For nonsymmorphic models, the nonsymmorphic operators belong to groups $\tau_i\sigma_x$ and $\tau_i\sigma_y$, while symmorphic operators belong to groups $\tau_i\sigma_0$ and $\tau_i\sigma_z$. Therefore, there are only eight possible nonsymmorphic operators. In k-space for $s = a/2$, operators $\tau_0\sigma_x$, $\tau_0\sigma_y$, $\tau_z\sigma_x$, and $\tau_z\sigma_y$ are represented in position space by $T_{a/2}$, $T_{a/2}S_{Iz}$, $T_{a/2}S_{zI}$, and $T_{a/2}S_{zI}S_{Iz}$, respectively. Operators $\tau_x\sigma_x$, $\tau_x\sigma_y$, $\tau_y\sigma_x$, and $\tau_y\sigma_y$ also contain the matrix S_{xI}, which effectively flips the electron and hole spaces, such that the position space equivalents are $S_{xI}T_{a/2}$, $S_{xI}T_{a/2}S_{Iz}$, $S_{xI}T_{a/2}S_{zI}$, and $S_{xI}T_{a/2}S_{zI}S_{Iz}$, respectively. Symmorphic symmetries generally only hold for an even number of atoms J, unless the operator is diagonal. Certain nonsymmorphic operators, namely those that do not contain the matrix S_{xI}, hold for either an even or odd amount of atoms, although the ends of a system with open boundary conditions break the nonsymmorphic symmetry [44, 46].

IV. NONSYMMORPHIC RANDOM MATRICES

A large $2J \times 2J$ Hermitian Hamiltonian with random components that is unconstrained by any symmetry contains $\sim J^2$ real independent parameters. Applying various symmetries to the Hamiltonian results in a reduced number of independent parameters and hence different level statistics. Specifically, it has been found that the addition of nonsymmorphic TRS results in only $\sim J$ real independent parameters [71], resulting in a transition in the level statistics from the Gaussian unitary ensemble (GUE) to Poisson statistics. As the nonsymmorphism is represented by a translation of half a unit cell, applying the operation twice will always result in a unitary transformation, creating periodicity in the lattice and allowing for block diagonalization of the position space Hamiltonian. The energy eigenvalues of each block represent a different k value in the corresponding band structure, and each block may possess a form of time reversal symmetry. The individual blocks may be categorized by whether they obey GUE statistics with $T^2 = 1$, Gaussian orthogonal ensemble (GOE) statistics with $T^2 = 0$, or Gaussian simplectic ensemble (GSE) statistics with $T^2 = -1$, denoted by $\beta = 1$, $\beta = 2$, and $\beta = 4$, respectively [6, 65–68].

TABLE II. Forms of time-reversal symmetry belonging to each block of a block-diagonalized random matrix with a translational symmetry of period P and in-built charge conjugation symmetry under the application of further symmetries. Column 'Symmetries' indicates which symmetry is applied in addition to the translational and charge conjugation symmetries. The second column indicates the corresponding topological index for the applied symmetries. The third column shows the number of irreducible blocks with the fourth column representing their size. Columns $\beta = 1$, $\beta = 2$, and $\beta = 4$ represent the number of blocks satisfying Gaussian unitary, orthogonal and simplectic ensemble statistics, respectively. The final column indicates the number of degenerate $\beta = 2$ blocks, i.e. blocks that do not have time-reversal symmetry individually, but do have a time-reversal symmetric partner block with identical eigenvalues, resulting in Kramer's degeneracy.

Symmetries	Index	No. of blocks	Size of blocks	$\beta = 1$	$\beta = 2$	$\beta = 4$	No. degenerate $\beta = 2$ blocks
-	$\mathbb{Z}_2$	J/P	$2P \times 2P$	0	J/P	0	0
Time-reversal ($T^2 = 1$)	$\mathbb{Z}$	J/P	$2P \times 2P$	2	$J/2P - 2$	0	$J/P - 2$
Time-reversal ($T^2 = -1$)	$\mathbb{Z}_2$	J/P	$2P \times 2P$	0	$J/P - 2$	2	$J/P - 2$
Time-reversal (NS)	$\mathbb{Z}_4$	J/P	$2P \times 2P$	1	$J/P - 2$	1	$J/P - 2$
Unitary (NS)	$\mathbb{Z}_2$	$2J/P$	$P \times P$	0	$2J/P$	0	0

We consider the constraints imposed by both symmorphic and nonsymmorphic TRS (and, by extension, chiral symmetry) in the presence of charge conjugation and translational symmetry of variable periodicity P (in terms of the number of electron orbitals), and also by a nonsymmorphic unitary translational symmetry of period $P/2$. For periodicity $P = 2$ this can be understood as the randomized values of the Hamiltonian (3) in position space for all possible long range hoppings. In this way we can distinguish between each of the four BdG topological classes with $C^2 = 1$, Table. I, solely through the level statistics related to TRS. We note that the presence or absence of charge conjugation symmetry only affects the spectrum by ensuring every energy level has a negative energy partner, however, for fixed translational period this does not affect the level statistics away from the band gap. For this reason, the level statistics may only be used to distinguish between classes with $C^2 = 1$, as each of these classes has a distinct form of TRS. For example, class DIII ($T^2 = -1$, $C^2 = 1$, $S^2 = 1$) is not distinguishable purely by level statistics from class CII ($T^2 = -1$, $C^2 = -1$, $S^2 = 1$) as they have they both have $T^2 = -1$.

Our results are displayed in Table II, where the first column 'Symmetries' indicates which symmetry is applied in addition to the charge conjugation and translational symmetry, and the second column shows the corresponding topological index for these applied symmetries. The number of blocks in terms of the period of the translational symmetry P and the size of each block are listed in the third and fourth column, respectively. Columns $\beta = 1$, $\beta = 2$, and $\beta = 4$ show the number of blocks with GUE, GOE, and GSE statistics. Each individual $\beta = 2$ block does not possess TRS, however, we find that, when the Hamiltonian as a whole satisfies TRS, many of these blocks are paired together with another $\beta = 2$ block with identical eigenvalues due to Kramer's degeneracy. In k-space these represent identical eigenvalues of the bulk band structure at opposite k values. A count of the number of paired blocks with $\beta = 2$ statistics is displayed in the final column of the table.

We find that, in the absence of any additional symmetries, the Hamiltonian belongs to the symmorphic D class and hence has a $\mathbb{Z}_2$ index. As the translational period is not affected by additional constraints, there are J/P irreducible blocks of size $2P \times 2P$ in the block diagonal form of the Hamiltonian. Each of these blocks has $\beta = 2$ statistics and are paired to a charge conjugation partner, with eigenvalues the negative of its own. Applying symmorphic TRS with $T^2 = 1$ results in a transition to the BDI symmetry class with a $\mathbb{Z}$ index. This does not change the number or size of the individual blocks, but there are now $J/P - 2$ blocks with $\beta = 2$ statistics. The remaining two blocks have TRS with two independent energy eigenvalues and $T^2 = 1$ and therefore obey $\beta = 1$ statistics. These correspond to the time-reversal invariant points at $k = 0$ and $k = \pi/a$ in the bulk band structure. The number of degenerate blocks also increases to $J/P - 2$ due to the TRS. In contrast to this, for $T^2 = -1$, we find that there are still $J/P - 2$ blocks with $\beta = 2$ statistics, but now the two remaining blocks have $\beta = 4$ statistics and individually satisfy $T^2 = -1$. As a result the eigenvalues of the $\beta = 4$ blocks display Kramer's degeneracy such that they each only produce a single independent eigenvalue. This is to be expected as the bulk band structure of models in the DIII class [82] also display Kramer's degeneracy at the time-reversal invariant points $k = 0$ and $k = \pi$.

Now consider the addition of nonsymmorphic TRS, resulting in a Hamiltonian belonging to the nonsymmorphic D class with a $\mathbb{Z}_4$ index. Similar to symmorphic TRS there are $J/P - 2$ blocks with $\beta = 2$ statistics, however, there is now one $\beta = 1$ block and one $\beta = 4$ block. The bulk band structure for the nonsymmorphic D class, Fig. 8 has Kramer's degeneracy only at one of either $k = 0$ or $k = \pi/a$ depending on the representation, the energy eigenvalues at this point correspond to the $\beta = 4$ block, while the $\beta = 1$ block corresponds to the energies of the non-Kramer's degenerate time-reversal invariant point. For completeness we also include the effect of an additional unitary translational symmetry, which, as we describe in Sec. IX, despite K-theory predictions [28], does not affect the topological classification, hence the model remains in the symmorphic D class with a

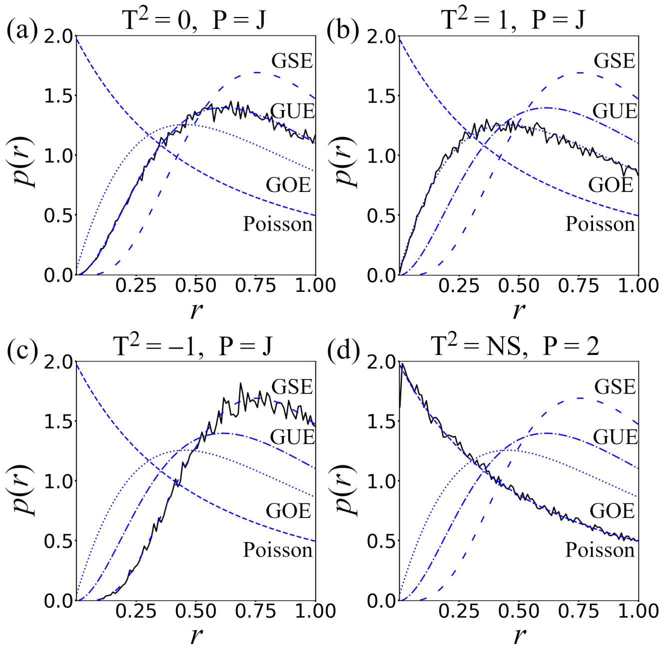

FIG. 4. Distributions of the ratio of consecutive level spacings for random matrices satisfying different forms of time-reversal symmetry, T^2, in the presence of fixed charge conjugation symmetry. Label P is the periodicity of the translational symmetry in terms of the number of electron orbitals J, where $P = J$ is equivalent to its absence. For (a) $T^2 = 0$ and $P = J$, such that there are effectively no applied symmetries, for (b) $T^2 = 1$ and $P = J$, for (c) $T^2 = -1$ and $P = J$, and for (d) time-reversal is nonsymmorphic, $T^2 = \mathrm{NS}$, which enforces a translational symmetry which, here, is chosen to have periodicity $P = 2$. In all plots, black solid lines show numerical data, blue dashed lines show the prediction of Poisson statistics, blue dotted lines show the prediction of the GOE ensemble, blue dot-dashed lines show the prediction of the GUE ensemble, and blue wide-dashed lines show the prediction of the GSE ensemble. We numerically diagonalized $2J \times 2J$ random matrices with $J = 1000$, where every independent real variable was taken from a standard normal distribution and averaged over an ensemble of 100 matrices. Only positive energy levels were used for all plots, and twofold degeneracy was neglected (for a degenerate pair of levels, only one was included).

$\mathbb{Z}_2$ index. As the unitary symmetry is represented by a translation, it effectively redefines the unit cell to be half its previous size, resulting in a doubling of the number of blocks and, by extension, halving their size.

We can further differentiate between classes by considering numerically the level distributions of the $2J \times 2J$ Hermitian random matrices under different forms of time-reversal symmetry, where each independent real parameter in the matrix is taken from the standard normal distribution (with mean zero and variance of 1). We numerically determine the eigenvalues E_n, the level spacing $s_n = (E_{n+1} - E_n)$, and the ratio of consecutive level spacings $r_n = \min\{s_n, s_{n-1}\}/\max\{s_n, s_{n-1}\}$ [69, 70], and we determine the distribution of ratios $p(r)$. We compare our numerical results with predictions for the Poisson distribution, GOE, GUE, and GSE [67, 68]. For the ratio distribution [69, 70],

$$p(r) = \begin{cases} \frac{2}{(1+r)^2}, & \text{Poisson}, \\ \frac{27}{4}\frac{(r+r^2)}{(1+r+r^2)^{5/2}}, & \text{GOE } (\beta = 1), \\ \frac{81\sqrt{3}}{2\pi}\frac{(r+r^2)^2}{(1+r+r^2)^4}, & \text{GUE } (\beta = 2), \\ \frac{729\sqrt{3}}{2\pi}\frac{(r+r^2)^4}{(1+r+r^2)^7}, & \text{GSE } (\beta = 4). \end{cases} \tag{20}$$

Figure 4 shows the numerically determined ratio distributions $p(r)$ for each of the forms of TRS. For random matrices that either do not have TRS or have symmorphic TRS we do not enforce a translational symmetry, or, equivalently, we set the periodicity $P = J$. As a result of the lack of translational symmetry we find that for Fig. 4(a) with $T^2 = 0$, Fig. 4(b) with $T^2 = 1$, and Fig. 4(c) with $T^2 = -1$, the ratio distributions closely match GUE, GOE, and GSE statistics, respectively. Fig. 4(d) shows the distribution in the presence of nonsymmorphic TRS, $T^2 = \mathrm{NS}$, by definition the nonsymmorphic TRS must enforce a translational symmetry for $P \leq J/2$. In Fig. 4(d) we have chosen $P = 2$, for which the distribution closely matches the prediction for the Poisson distribution. We note that, if we were to arbitrarily enforce a translational symmetry on matrices with $T^2 = 0$, $T^2 = 1$, or $T^2 = -1$, we would also find that their distributions followed the prediction for the Poisson distribution. However, there is no requirement to do so, unlike for matrices with nonsymmorphic TRS. Varying the periodicity of the nonsymmorphic TRS also shifts the distribution away from Poisson statistics and towards GOE and GUE statistics [71], but GSE statistics can not be obtained by changing the periodicity.

V. SYMMORPHIC MODELS

While the topology of symmorphic topological superconductors is already understood [7, 8, 11], the principles used to calculate their respective topological indices lends significantly to similar calculations in the nonsymmorphic classes. For this reason we introduce the topology of the three symmorphic BdG classes D, BDI, and DIII, beginning with class D which possesses only charge conjugation symmetry $C^2 = 1$. An exact D class model, derived from Hamiltonian (3), is given in the supplementary material [82] alongside a numerically obtained bulk band structure. Here, we only focus on the generalized $\mathbb{Z}_2$ topological index, which for D class Hamiltonians is known as the Majorana number [1, 11] defined as

$$N_{\mathrm{D}}^{\mathrm{S}} = \mathrm{sgn}(\mathrm{Pf}[H_M(0)]\mathrm{Pf}[H_M(\pi/a)]), \tag{21}$$

where $H_M(k)$ is the Hamiltonian in the Majorana basis, and $\mathrm{Pf}[H_M(0)]$ and $\mathrm{Pf}[H_M(\pi/a)]$ are the Pfaffians of the Hamiltonian at $k = 0$ and $k = \pi/a$, respectively. The physical significance of the Majorana number is that, for a finite model in position space, there are MZM exponentially localized onto the edges of the chain for parameter regions in which $N_{\mathrm{D}}^{\mathrm{S}} = -1$. The Majorana number can be used to differentiate between topologically trivial and non-trivial phases that host MZM for all superconductors. For example, the symmorphic BDI class, with $T^2 = 1$, $C^2 = 1$, and $S^2 = 1$, has topological and non-topological phases with different Majorana numbers. However, this is only one part of the topology of the BDI class, which has a $\mathbb{Z}$ topological index, Table I, due to the presence of chiral symmetry. This index can be understood in terms of a winding number, $N_{\mathrm{BDI}}^{\mathrm{S}}$, similar to the two-band SSH model [40, 41]. As we use the winding number formalism for the nonsymmorphic AII class, Sec. VI, and the nonsymmorphic D class, Sec. VII, we work through an example model here to show how a winding path can be constructed for four-band models.

We write an example with minimal parameters with time-reversal operator $U_T = I$ and chiral operator $U_S = \tau_x\sigma_0$. The Bloch Hamiltonian is

$$\begin{aligned} H(k) &= \begin{pmatrix} \hat{h}(k) & \hat{\Delta}(k) \\ \hat{\Delta}^{\dagger}(k) & -\hat{h}^T(-k) \end{pmatrix}, \qquad (22) \\ \hat{h}(k) &= \begin{pmatrix} -\mu+u & v+ve^{-ika} \\ v+ve^{ika} & -\mu-u \end{pmatrix}, \\ \hat{\Delta}(k) &= \begin{pmatrix} 0 & \Delta_s-\Delta_s e^{-ika} \\ -\Delta_s+\Delta_s e^{ika} & 0 \end{pmatrix}, \end{aligned}$$

where, from Hamiltonian (3), we have set $w = v$ and $\Delta_s' = \Delta_s$. Note that setting the alternating onsite energy to zero results allows for the block diagonalization of the Hamiltonian into that of the two-band Kitaev chain, as discussed in Sec. IX. In general, the band structure for the first quantized Hamiltonian is an insulator. Analytic forms of the energy eigenvalues and a numerically obtained band structure are given in the supplementary material [82]. To see this we must first off-block diagonalize the Hamiltonian into a so-called Q-matrix with $Q(k) = U_{xI}^{\dagger} H(k) U_{xI}$, where

$$U_{xI} = \frac{1}{\sqrt{2}}\begin{pmatrix} 0 & 1 & 0 & -1 \\ 1 & 0 & -1 & 0 \\ 0 & 1 & 0 & 1 \\ 1 & 0 & 1 & 0 \end{pmatrix}$$

such that

$$Q(k) = \begin{pmatrix} 0 & q(k) \\ q^{\dagger}(k) & 0 \end{pmatrix}, \qquad (23)$$

where

$$q(k) = \qquad (24)$$
$$\begin{pmatrix} \mu+u & -v-ve^{ika}-\Delta_s+\Delta_s e^{ika} \\ -v-ve^{-ika}+\Delta_s-\Delta_s e^{-ika} & \mu-u \end{pmatrix}.$$

We can define a winding number in this form by plotting the path taken between $-\pi/a < k \leq \pi/a$ in the complex plane by the product of the eigenvalues of $q(k)$, which we denote as $E_q(k)$ [11, 25, 27]. For Eq. (24) we find that

$$\begin{aligned} E_q(k) &= 2\Delta_s^2+\mu^2-u^2-2v^2-(2\Delta_s^2+2v^2)\cos(ka) \\ &\quad +4i\Delta_s v\sin(ka), \end{aligned} \qquad (25)$$

where the number of times $E_q(k)$ encircles the origin defines the winding number. For this minimal model we find that this defines the following topological phases,

$$N_{\mathrm{BDI}}^{\mathrm{S}} = \begin{cases} 1 & \text{if } E_q(0)E_q(\pi/a) < 0 \text{ and } \Delta_s > 0, \\ 0 & \text{if } E_q(0)E_q(\pi/a) > 0, \\ -1 & \text{if } E_q(0)E_q(\pi/a) < 0 \text{ and } \Delta_s < 0, \end{cases} \qquad (26)$$

where $E_q(0) = \mu^2-u^2-4v^2$ and $E_q(\pi/a) = \mu^2-u^2+4\Delta_s^2$. Phases $N_{\mathrm{BDI}}^{\mathrm{S}} = 1$ and $N_{\mathrm{BDI}}^{\mathrm{S}} = -1$ host MZM in position space and are differentiated by whether $E_q(k)$ follows a clockwise or anticlockwise trajectory, respectively. In general we consider Δ_s to be positive, although to define $N_{\mathrm{BDI}}^{\mathrm{S}} = -1$ with $\Delta_s < 0$ we can consider a phase $\phi_s = \pi$ that does not violate the symmetries of the system. We plot the energy levels of a finite system in position space for 48 unit cells as a function of the chemical potential μ in Fig. 5(a), where we find MZM for parameter values in agreement with Eq. (26). The MZM are exponentially localized onto the ends of the chain, with an example wavefunction shown in Fig. 5(b). An example band structure

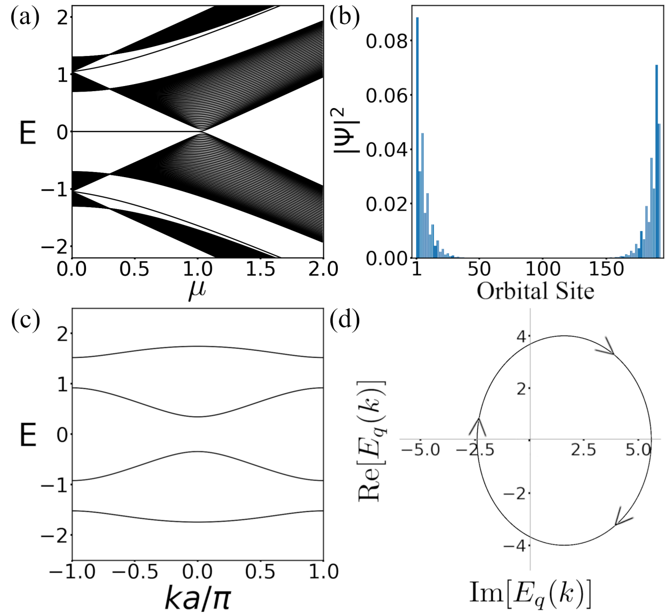

FIG. 5. Majorana zero modes and winding number for the symmorphic superconducting BDI model ($T^2 = 1$, $C^2 = 1$, $S^2 = 1$) described by Hamiltonian (22). (a) Energy levels E in position space as a function of the chemical potential μ for 48 unit cells. (b) Probability density per orbital site for an example MZM. (c) Example bulk band structure E(k) with the corresponding path of $E_q(k)$ in (d) defining a winding number $N_{\mathrm{BDI}} = 1$. Parameter values are $u = 0.3$, $v = 0.5$, and $\Delta_s = 0.5$ in (a) and (b) with value $\mu = 0.9$ fixed in (b), and $\mu = 0.7$, $u = 0.3$, $v = 0.5$, and $\Delta_s = 0.5$ in (c) and (d).

in the phase $N_{\rm BDI}^{\rm NS}=1$ is given in Fig. 5(c), with the corresponding path of $E_q(k)$ in the complex plane shown in Fig. 5(d).

The CII class, with $T^2=-1$, $C^2=-1$, and $S^2=1$, is also defined by a winding number, however, it always winds around the origin an even number of times, resulting in a $2\mathbb{Z}$ index. This index can be seen as the sum of the winding number of two coupled chains [27]. An example model is explored in the supplementary material [82].

The DIII class, with $T^2=-1$, $C^2=1$, and $S^2=1$, despite possessing chiral symmetry similar to the BDI class, can not be defined by a winding number, as, by direct calculation, the winding number can be shown to always be zero [27]. Due to the Kramer's degeneracy we can also not simply use the Majorana formula, Eq. (21). Instead, the topology of the DIII class is defined by a unique $\mathbb{Z}_2$ Fermi surface topological invariant [24, 26, 79, 80]. This is not purely a result of the different form of TRS, as we show in Sec. VI that nonsymmorphic models with $T^2=-1$ in the AII class can have an associated winding number equivalent. In general, the band structure for the first quantized Hamiltonian is an insulator. The band structure for this model displays Kramer's degeneracy at the time-reversal invariant points $k=0$ and $k=\pi/a$, such that the two positive energy bands are degenerate at these points, and, similarly, the two negative energy bands are also degenerate at these points. In position space this manifests as every energy level being doubly degenerate. We can define the Fermi surface topological invariant as

$$N_{\rm DIII}^{\rm S}=\frac{{\rm Pf}(T^\dagger\tilde{q}(\pi))}{{\rm Pf}(T^\dagger\tilde{q}(0))}\exp\!\left(-\frac{1}{2}\int_0^\pi dk\,{\rm Tr}[\tilde{q}^\dagger(k)\partial_k\tilde{q}(k)]\right), \tag{27}$$

where $N_{\rm DIII}^{\rm S}=\pm1$, T is the time-reversal operator of $\tilde{q}(k)$, and $\tilde{q}(k)$ is a component of the flat band Hamiltonian [24, 26, 79, 80]. A derivation of Eq. (27) for an example system, derived from Hamiltonian (3), is shown in the supplementary material [82] alongside a numerically obtained bulk band structure.

VI. NONSYMMORPHIC AII CLASS WITH A $\mathbb{Z}_2$ INDEX AND $T^2=-1$, $C^2=\mathrm{NS}$, $S^2=\mathrm{NS}$

The AII class is generally topologically trivial when only symmorphic TRS $T^2=-1$ is present. By introducing nonsymmorphic charge-conjugation and chiral symmetry we can induce a non-trivial $\mathbb{Z}_2$ index [28]. Although charge-conjugation symmetry is present, we do not consider this model a superconductor as the symmetry is nonsymmorphic. Therefore, we cannot write the model in the BdG formalism with fixed charge conjugation symmetry. Note that there also exists a nonsymmorphic AII class with no charge-conjugation or chiral symmetry, but an additional nonsymmorphic unitary symmetry that does not affect the trivial topology of the symmorphic AII class, as discussed in Sec. IX.

We first write a generic Hamiltonian with four atomic sites in the basis $\Psi^\dagger=(c_{A,k}^\dagger,c_{B,k}^\dagger,c_{C,k}^\dagger,c_{D,k}^\dagger)$. This model represents two coupled CDW chains that are time-reversal partners of each other such that $U_T=\tau_y\sigma_0$. For $s=a/2$, atomic sites A and C are at the same spatial position, and sites B and D are at the same spatial position. The chains are described by a constant hopping v and alternating onsite energy $\pm u$, and we introduce a coupling parameter Γ between the chains to distinguish from the superconducting order parameter Δ_s found in previous models. A schematic of the system is given in Fig. 6(a). The bulk Hamiltonian for this system can be written as

$$H(k)=\begin{pmatrix} h(k) & d(k)\\ d^\dagger(k) & h^*(-k)\end{pmatrix}, \tag{28}$$

where $d(k)=-d^T(-k)$. Imposing charge-conjugation and chiral symmetry satisfied by $U_C=\tau_z\sigma_y$ and $U_S=\tau_x\sigma_y$, we have

$$\begin{aligned} h(k) &= \begin{pmatrix} u & 2v\cos(ka/2)\\ 2v\cos(ka/2) & -u\end{pmatrix},\\ d(k) &= \begin{pmatrix} 0 & 2\Gamma\cos(ka/2+\phi_\Gamma)\\ -2\Gamma\cos(ka/2-\phi_\Gamma) & 0\end{pmatrix}.\end{aligned}$$

In general the band structure for this Hamiltonian is insulating, with energy eigenvalues

$$\begin{aligned} E^2 &= 2\Gamma\cos(2\phi_\Gamma)\cos(ka)+2v^2\cos(ka)+2\Gamma^2+2v^2\\ &\quad +u^2\pm4\Gamma\sin(\phi_\Gamma)\sin(ka)\sqrt{\Gamma^2\cos^2(\phi_\Gamma)+v^2}\,.\end{aligned}$$

An example band structure is given in Fig. 6(b), which shows Kramer's degeneracy at the time-reversal invariant points $k=0$ and $k=\pi/a$. In position space this may be written in the same form as Eq. (2) in the basis $\Psi=(c_{A,1}^\dagger,c_{B,1}^\dagger,c_{C,1}^\dagger,c_{D,1}^\dagger,c_{A,2}^\dagger,c_{B,2}^\dagger,c_{C,2}^\dagger,c_{D,2}^\dagger)$, with finite u and v, $\Delta_s=-\Gamma$, $\phi_s=-\phi_\Gamma$ and all other parameters equal to zero. The topology of this model is described by a $\mathbb{Z}_2$ index which we can calculate by utilizing the chiral symmetry to define a Q-matrix, Eq. (23), with $Q(k)=U_{xy}^\dagger H(k)U_{xy}$, where

$$U_{xy}=\frac{1}{\sqrt{2}}\begin{pmatrix} i & 0 & -i & 0\\ 0 & -i & 0 & i\\ 0 & 1 & 0 & 1\\ 1 & 0 & 1 & 0\end{pmatrix}$$

such that

$$q(k)=\begin{pmatrix} 2i\Gamma\cos(ka/2+\phi)-u & 2v\cos(ka/2)\\ 2v\cos(ka/2) & u+2i\Gamma\cos(ka/2-\phi)\end{pmatrix}.$$

We plot the path in the complex plane of the product of the eigenvalues of $q(k)$ which we denote as $E_q(k)$, and, for this system, we find that

$$\begin{aligned} E_q(k) &= 4\Gamma^2\sin^2(ka/2)-4\Gamma^2\cos^2(\phi_\Gamma)-4v^2\cos^2(ka/2)\\ &\quad -u^2-4iu\Gamma\sin(\phi_\Gamma)\sin(ka/2)\,. \end{aligned} \tag{29}$$

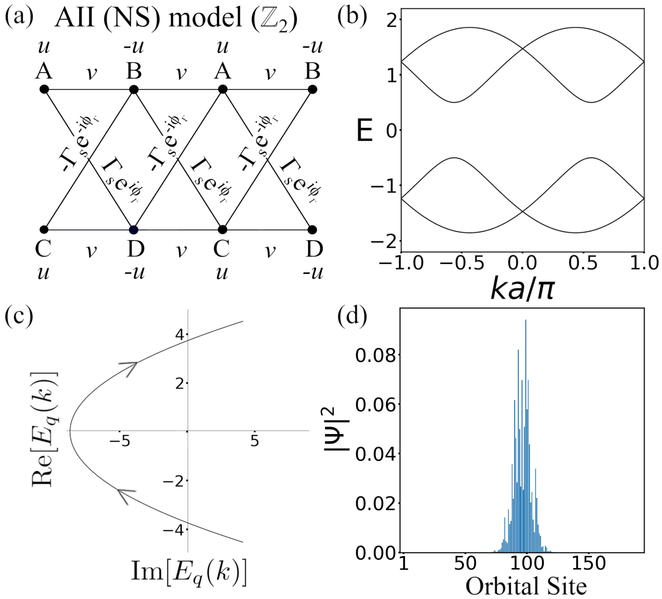

FIG. 6. Nonsymmorphic AII class with symmorphic time-reversal symmetry and nonsymmorphic charge-conjugation symmetry shown with intracell spacing $s = a/2$. (a) A schematic of an example system described by Hamiltonian (28) with alternating onsite energy $\pm u$, constant nearest-neighbor hopping v, and constant coupling Γ with phase ϕ_Γ. (b) An example band structure, as $T^2 = -1$ Kramer's degeneracy is present at both $k = 0$ and $k = \pi/a$, (c) shows the corresponding path of $E_q(k)$ for $N^{\mathrm{NS}}_{\mathrm{AII}} = 1$. (d) An example soliton state for an atomically smooth texture in the onsite energy localized on the transition $u = 0$ with $u_{\max} = 1$, $\zeta = 12$ and for 48 unit cells, with weak atomically sharp disorder in the hopping parameter v of strength $W = 10^{-10}$ that lifts the Kramer's degeneracy. Figures (b), (c), and (d) have parameter values $v = 0.4$, $\Gamma = 0.8$, and $\phi_\Gamma = \pi/4$, and (b) and (c) also have a fixed value of $u = 0.5$.

Similarly to the $\mathbb{Z}_4$ model, Sec. VII, plotting $E_q(k)$ between $k = -\pi/a$ and $k = \pi/a$ results in an open path with a guaranteed crossing of the real axis at $k = 0$. This is due to the $4\pi/a$ periodicity in the complex plane induced by the nonsymmorphic symmetry, and is in contrast to symmorphic chiral symmetry which produces a closed-loop winding number, Sec. V. An example path of $E_q(k)$ is plotted in Fig. 6(c). As is the case of the two-band CDW model, we can attempt to find the point of the phase transition by setting $E_q(0) = 0$, however, this yields $-u^2 - 4v^2 - 4\Gamma^2 = 0$. As u^2, v^2, and Γ^2 are all positive constants, $E_q(0) < 0$ for all nonzero parameter values. We instead define the $\mathbb{Z}_2$ index by examining the constraints imposed on the end of the path at $k = \pi/a$. To do this we first set $\mathrm{Im}[E_q(k)] = -4u\Gamma\sin(\phi_\Gamma)\sin(ka/2) = 0$, for which there are three solutions for $0 < k \leq \pi/a$: $\phi_\Gamma = 0$, $\Gamma = 0$, and $u = 0$. For these solutions $E_q(k)$ traverses only the real axis, and, as $E_q(0) < 0$, the sign of $E_q(\pi/a)$ for each of these solutions determines whether the path passes through the origin, causing a phase transition. We find that $E_q(\pi/a, \phi_\Gamma = 0) = E_q(\pi/a, \Gamma = 0) = -u^2$, and, for nonzero u, these are always negative quantities such that the path of $E_q(k)$ does not pass through the origin. However, $E_q(\pi/a, u = 0) = 4\Gamma^2(1 - \cos^2\phi_\Gamma)$ which is always positive, such that the path of $E_q(k)$ does pass through the origin, inducing a phase transition. It is not possible to adiabatically transform the parameters of $E_q(k)$ to avoid this transition, and hence there is a topological phase transition protected by the nonsymmorphic symmetry at $u = 0$.

We find that, similar to other nonsymmorphic models [61], neither phase hosts zero-energy edge states. To emphasize the topological nature of this transition we instead consider an atomically smooth soliton in the alternating onsite energy described by the function

$$u_l = (-1)^l\, u_{\max}\tanh\left(\frac{l - N - 1/2}{\zeta}\right), \tag{30}$$

for atomic site l, where $u_{\max}$ is the magnitude of the texture at infinity and ζ is the soliton width. We find that, for atomically sharp solitons ($J \to 0$) or smooth solitons on the length scale of the unit cell ($J \gg a$), the nonsymmorphic symmetries are approximate in the presence of a soliton that breaks translational invariance. This results in energy levels that are not symmetric about $E = 0$, including the soliton with finite energy E_{sol} that does not have a chiral partner at energy $-E_{\mathrm{sol}}$. This effect is minimized for an atomically smooth soliton described by Eq. (30), the nonsymmorphic symmetries are not significantly broken as the soliton energy level is pinned at zero-energy and is doubly degenerate due to Kramer's degeneracy. The zero-energy mode has a wavefunction exponentially localized onto the center of the soliton at the point $u = 0$, as shown in Fig. 6(d). To obtain Fig. 6(d) numerically we broke the Kramer's degeneracy by adding small disorder to the hopping parameter v, drawn randomly from a uniform distribution $[-W, W]$ of magnitude $W = 10^{-10}$.

VII. NONSYMMORPHIC D CLASS WITH A $\mathbb{Z}_4$ INDEX AND $T^2 = \mathrm{NS}$, $C^2 = 1$, $S^2 = \mathrm{NS}$

A. Minimal model with $U_T = \tau_0\sigma_x$

The $\mathbb{Z}_2$ index belonging to the symmorphic D class, Sec. V, is expanded to a $\mathbb{Z}_4$ index when nonsymmorphic TRS and chiral symmetry are enforced. We note that the $\mathbb{Z}_4$ index does not refer to the degeneracy of the ground state [1, 84, 85] or unique propagation of edge currents [86], but rather four distinct topological phases, with phase transitions that may be unrelated to the Majorana number. Here, we explore in more detail an example model with $U_T = \tau_0\sigma_x$ and $U_S = \tau_x\sigma_x$ when written in the type II ‘canonical’ basis with $s = a/2$, as first described in Ref. [71]. The BdG Bloch Hamiltonian for this system is

$$
\begin{aligned}
H(k) &= \begin{pmatrix} \hat{h}(k) & \hat{\Delta}(k) \\ \hat{\Delta}^{\dagger}(k) & -\hat{h}^{T}(-k) \end{pmatrix}, \qquad (31)\\
\hat{h}(k) &= \begin{pmatrix} -\mu & 2v\cos(ka/2) \\ 2v\cos(ka/2) & -\mu \end{pmatrix},\\
\hat{\Delta}(k) &= \begin{pmatrix} 0 & 2i\Delta_s \sin(ka/2+\phi_s) \\ 2i\Delta_s\sin(ka/2-\phi_s) & 0 \end{pmatrix},
\end{aligned}
$$

where, from the generalized Hamiltonian (3), we have set $w = v$, $\Delta_s = \Delta'_s$, and $\phi_s = -\phi'_s$. In general, the band structure for the first quantized Hamiltonian is insulating, with energy eigenvalues

$$
\begin{aligned}
E^2 &= \mu^2 + f^2 + g^2 + S^2 \pm \sqrt{\mu^2 f^2 + S^2(f^2+g^2)},\\
f(k) &= 2v\cos(ka/2),\\
S(k) &= 2\Delta_s \sin(\phi_s)\cos(ka/2),\\
g(k) &= 2\Delta_s\cos(\phi_s)\sin(ka/2).
\end{aligned}
$$

In contrast to the case of real TRS $T^2 = -1$ for the symmorphic DIII class, which displays Kramer's degeneracy at both time-reversal invariant points $k = 0$ and $k = \pi/a$, the bulk band structure described by these equations for nonsymmorphic TRS only has Kramer's degeneracy present at the Brillouin zone edges, $k = \pi/a$ [61]. Numerically obtained examples for both cases are shown in the supplementary material [82]. The only differences distinguishing this Hamiltonian from the two-band Kitaev chain [1] in the symmorphic D class with no TRS is that the phase of the order parameter alternates along the chain, as shown schematically in Fig. 7(a). This change induces the nonsymmorphic TRS, resulting in two additional topological phase transitions in addition to the $\mathbb{Z}_2$ Majorana number. These four phases can be related to the phases of two band models, namely the noninteracting charge-density-wave (CDW) model, Fig. 7(b), and the Kitaev chain, Fig. 7(c). This relation is possible as, within a given phase, it is possible to adiabatically deform certain parameters to zero such that the Hamiltonian becomes block-diagonalizable, i.e. the hopping parameter v in the CDW related phases, and the phase of the order parameter in the Kitaev chain related phases. Hence the topological phase transitions for the $\mathbb{Z}_4$ model, as given in the phase diagram in Fig. 7(d), can be related to the phase transitions of the $\mathbb{Z}_2$ and $\mathbb{Z}$ indices in the CDW and Kitaev models. The corresponding phase diagram for the Kitaev model is shown in Fig. 7(e).

As the Kitaev-like phases are related to the topologically non-trivial phases of the Kitaev chain we expect $N_{\mathrm{D}}^{\mathrm{NS}} = 1$ and $N_{\mathrm{D}}^{\mathrm{NS}} = 3$ to support MZM. By plotting the energy levels in position space, we confirm that the Kitaev-like phases do support MZM while the CDW phases do not, and also show gap closing points between CDW phases and Kitaev phases. Fig. 8(a) shows the energy levels as a function of the chemical potential for parameter values $v = 1$, $\Delta_s = 1$, and $\phi_s = \pi/4$. We find that this allows us to move from $N_{\mathrm{D}}^{\mathrm{NS}} = 2$, across the Majorana phase transition and into $N_{\mathrm{D}}^{\mathrm{NS}} = 1$, resulting in MZM, and then back into $N_{\mathrm{D}}^{\mathrm{NS}} = 4$ where those zero modes dissipate back into the bulk. We also plot the energy levels as a function of the superconducting phase ϕ_s in Fig. 8(b) for parameter values $\mu = v = 1$ and $\Delta_s = 0.5$. We observe topological phase transitions between phases $N_{\mathrm{D}}^{\mathrm{NS}} = 1$ and $N_{\mathrm{D}}^{\mathrm{NS}} = 4$ and between $N_{\mathrm{D}}^{\mathrm{NS}} = 4$ and $N_{\mathrm{D}}^{\mathrm{NS}} = 3$, and both $N_{\mathrm{D}}^{\mathrm{NS}} = 1$ and $N_{\mathrm{D}}^{\mathrm{NS}} = 3$ host MZM. This can be supported by a direct Majorana number calculation, which we discuss in the next section.

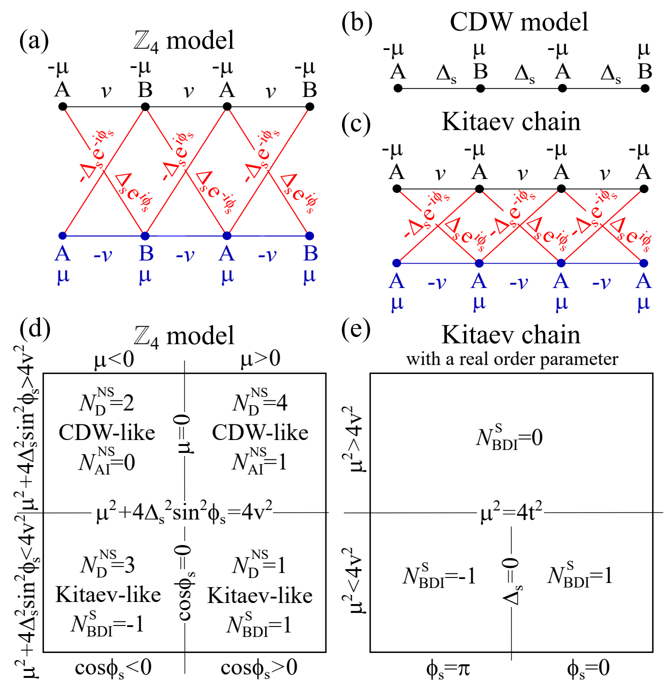

FIG. 7. (a) The $\mathbb{Z}_4$ model shown in the Bogoliubov-de-Gennes (BdG) representation with two orbitals A and B per cell with constant chemical potential μ, nearest-neighbor hopping v, and magnitude of the superconducting order parameter Δ_s, with alternating phase of the order parameter ϕ_s. (b) The noninteracting CDW model where Δ_s acts as nearest-neighbor hopping, and μ is now an alternating onsite energy. (c) The Kitaev chain in the BdG representation, now with constant phase ϕ_s. (d) Phase diagram of the $\mathbb{Z}_4$ topological superconductor with phases $N_{\mathrm{D}}^{\mathrm{NS}} = 1, 2, 3, 4$ and (e) the Kitaev chain with a real order parameter. In (d), each phase is labeled using a phase of a two-band model. The CDW model is in the nonsymmorphic AI class and has two phases denoted $N_{\mathrm{AI}}^{\mathrm{NS}} = 0, 1$, and the Kitaev chain with nearest-neighbor hopping belongs to the symmorphic class BDI and has three possible winding numbers $N_{\mathrm{BDI}}^{S} = 0$, 1, and -1. For (d) and (e), in the designation of the Kitaev chain phases, we assume $v > 0$. Schematics are shown with intracell spacing $s = a/2$.

B. Calculation of the $\mathbb{Z}_4$ index for a minimal model

To calculate the parameter regions in which each of the $\mathbb{Z}_4$ phases exists we can take one of two approaches, utilizing either a Pfaffian based equation [28, 71], or a nonsymmorphic winding number equivalent. First with the Pfaffian approach, we must transform the Hamiltonian into the form

$$\tilde{H}(k) = \begin{pmatrix} X(k) & iY(k) \\ -iY(k) & -X(k) \end{pmatrix}; \tag{32}$$
$$X(\pi/a) = X(-\pi/a), \quad Y(\pi/a) = -Y(-\pi/a),$$

which we obtain through the unitary transformation $\tilde{H}(k) = U^{\dagger}\mathcal{H}(k)U$, where

$$U = \begin{pmatrix} 1 & 0 & 0 & 0 \\ 0 & 0 & 0 & 1 \\ 0 & 1 & 0 & 0 \\ 0 & 0 & 1 & 0 \end{pmatrix}.$$

Using this we can define the $\mathbb{Z}_4$ topological index as

$$N_{\mathrm{D}}^{\mathrm{NS}} = -\frac{2}{\pi}\arg\left\{\mathrm{Pf}[\sigma_x Z(\pi/a)]\right\} + \frac{1}{\pi}\int_0^{\pi/a} dk \frac{\partial}{\partial k}\arg\{\det[\sigma_x Z(k)]\}, \tag{33}$$

where $N_{\mathrm{D}}^{\mathrm{NS}}$ is defined modulo 4, $Z(k) = X(k) + iY(k)$, and $\arg(Z) = \arg(re^{i\varphi}) = \varphi$ for $\pi < \varphi \leq \pi$ [28]. For Hamiltonian (31) we find that

$$X(k) = \begin{pmatrix} \mu & 0 \\ 0 & -\mu \end{pmatrix},$$
$$iY(k) = \begin{pmatrix} 2i\Delta_s \sin(ka/2 + \phi_s) & 2v\cos(ka/2) \\ -2v\cos(ka/2) & -2i\Delta_s \sin(ka/2 - \phi_s) \end{pmatrix},$$

such that

$$Z(k) = \begin{pmatrix} \mu + 2i\Delta_s \sin(ka/2 + \phi_s) & 2v\cos(ka/2) \\ -2v\cos(ka/2) & -\mu - 2i\Delta_s \sin(ka/2 - \phi_s) \end{pmatrix}.$$

Substituting this into Eq. (33) we obtain phases

$$N_{\mathrm{D}}^{\mathrm{NS}} = \begin{cases} 1 & \text{if } \mu^2 + 4\Delta_s^2\sin^2(\phi_s) < 4v^2 \text{ and } \cos\phi_s > 0, \\ 2 & \text{if } \mu^2 + 4\Delta_s^2\sin^2(\phi_s) > 4v^2 \text{ and } \mu < 0, \\ 3 & \text{if } \mu^2 + 4\Delta_s^2\sin^2(\phi_s) < 4v^2 \text{ and } \cos\phi_s < 0, \\ 4 & \text{if } \mu^2 + 4\Delta_s^2\sin^2(\phi_s) > 4v^2 \text{ and } \mu > 0, \end{cases}$$

as given in the phase diagram, Fig. 7(d). Here we have taken into account a discontinuity in the integral for the case $\mu^2 + 4\Delta_s^2\sin^2(\phi_s) < 4v^2$ and $\mu\cos(\phi_s) > 0$.

Alternatively, the topology can be calculated more intuitively from the utilization of the chiral symmetry, similarly to the case of the nonsymmorphic AII class described in Sec. VI. First, we transform Hamiltonian (3) into the form of a Q-matrix, Eq. (23), with $Q(k) = U_{xx}^{\dagger}\mathcal{H}(k)U_{xx}$ where

$$U_{xx} = \frac{1}{\sqrt{2}}\begin{pmatrix} -1 & 0 & 1 & 0 \\ 0 & -1 & 0 & 1 \\ 0 & 1 & 0 & 1 \\ 1 & 0 & 1 & 0 \end{pmatrix}$$

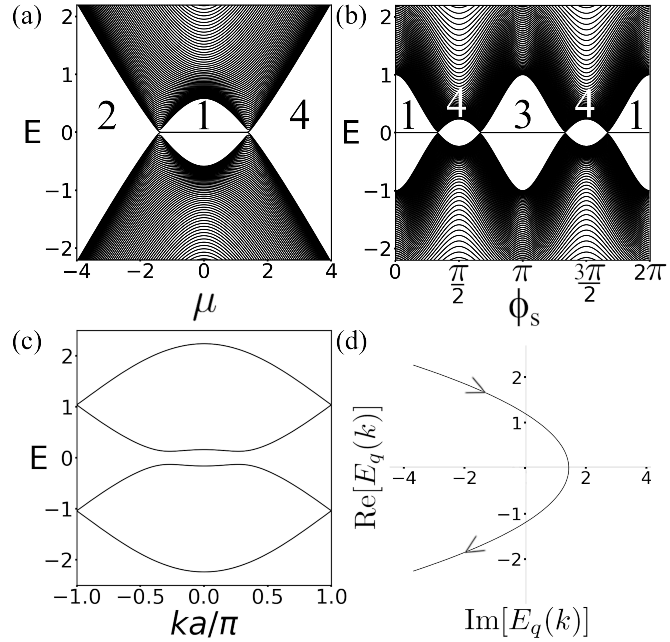

FIG. 8. Energy levels and winding number equivalent for the nonsymmorphic superconducting D model ($T^2 = \mathrm{NS}$, $C^2 = 1$, $S^2 = \mathrm{NS}$) described by Hamiltonian (31). (a) Energy levels E in position space for 48 unit cells as a function of the chemical potential μ, and (b) as a function of the superconducting phase ϕ_s. Numbers in each plot show the phase $N_{\mathrm{D}}^{\mathrm{NS}}$ of the $\mathbb{Z}_4$ model. (c) Example bulk band structure E(k) with the corresponding path of $E_q(k)$ in (d) defining a phase $N_{\mathrm{D}}^{\mathrm{NS}} = 3$. Parameter values are $v = 1$, $\Delta_s = 1$ in (a) and (b), with $\phi_s = \pi/4$ in (a) and $\mu = 1$ in (b), and $\mu = 1$, $v = 0.6$, $\Delta_s = 0.2$, and $\phi_s = \pi/4$ in (c) and (d).

such that

$$q(k) = \begin{pmatrix} \mu - 2i\Delta_s \sin(ka/2 + \phi_s) & -2v\cos(ka/2) \\ -2v\cos(ka/2) & \mu - 2i\Delta_s \sin(ka/2 - \phi_s) \end{pmatrix}.$$

To characterize the topology we plot the product of the eigenvalues of $q(k)$ in the complex plane across the Brillouin zone, i.e. for $-\pi/a \leq k < \pi/a$, where, for this system, the product can be written as

$$\begin{aligned} E_q(k) &= \mu^2 - 4\Delta_s^2\sin^2(ka/2) + 4\Delta_s^2\sin^2(\phi_s) \\ &- 4v^2\cos^2(ka/2) - 4i\mu\Delta_s\cos(\phi_s)\sin(ka/2). \end{aligned} \tag{34}$$

An example band structure is shown in Fig. 8(c), with a corresponding path of $E_q(k)$ shown in Fig. 8(d). Phase transitions are defined for parameter values in which $E_q(k)$ passes through the origin, and that can not be avoided by adiabatically deforming the parameters. Unlike the symmorphic BDI class described in Sec. V this does not produce a closed-loop winding number, but rather an open-loop path due to the 4π periodicity of the imaginary and real components of $E_q(k)$ induced by the nonsymmorphic symmetry [44]. Typically, this methodology results in a $\mathbb{Z}_2$ index, as the Hamiltonian symmetries enforce the path to be symmetric about the real axis such that the only topological band gap closing occurs at $E_q(0)$. This $\mathbb{Z}_2$ index can be seen in the case of the nonsymmorphic AI class with two bands in Ref. [61]. For the $\mathbb{Z}_4$ model we find two further topological phase transitions unrelated to the point $E_q(0)$ that can be defined at variable k values depending on the parameter values of the system. These additional transitions match those predicted previously by Eq. (33).

We first examine the transition associated with $E_q(0) = 0$, which we find agrees with the prediction of Eq. (33) between CDW and Kitaev-like phases. It is trivial to see this by setting

$$E_q(0) = \mu^2 + 4\Delta_s^2 \sin^2(\phi_s) - 4v^2 = 0, \tag{35}$$

which immediately returns the expected formula. For the other two transitions we must solve $E_q(k) = 0$ for nonzero k, a problem that can be simplified by considering the imaginary and real parts in isolation. Specifically, we must find parameter values such that $\mathrm{Im}[E_q(k)] = -4\mu\Delta_s \cos(\phi_s)\sin(k/2) = 0$ for nonzero k. We assume that the electron and hole chains remain coupled with $\Delta_s \neq 0$, leaving either $\mu = 0$ or $\cos(\phi_s) = 0$ as solutions. For $\mu = 0$ we find that $E_q(\pi) = -4\Delta_s^2 \sin^2(\phi_s)$, which is always less than zero. Since the path of $E_q(k)$ is confined to the real axis for $\mu = 0$, this means that, for the CDW-like phases with $E_q(0) > 0$, the path must always pass through the origin, resulting in a closing of the bulk band gap that corresponds to the phase transition between CDW-like phases. For the Kitaev-like phases with $E_q(0) < 0$ both ends of the path are now negative and a crossing is not guaranteed. The same logic can be applied in the case of $\cos\phi_s = 0$ for which $E_q(\pi) = \mu^2$, since this is always positive, a transition is only guaranteed in the Kitaev-like phases with $E_q(0) < 0$. Therefore, we have shown that the topology of the $\mathbb{Z}_4$ model can be derived purely from the utilization of the chiral symmetry.

Example trajectories for each of the four phases are shown in Fig. 1. The CDW-like phases, shown in Fig. 1(a) and Fig. 1(b), are related by a sign reversal of μ. As discussed previously, this sign change necessarily drives a phase transition at $\mu = 0$. The Kitaev-like phases, depicted in Fig. 1(c) and Fig. 1(d), are similarly related by a sign reversal of $\cos(\phi_s)$, implying a phase transition at $\cos(\phi_s) = 0$. It is possible, however, to adiabatically deform Δ_s and ϕ_s at fixed μ in Fig. 1(a) to produce a trajectory resembling Fig. 1(b) without encountering a phase transition. In contrast, changing the sign of μ invariably induces a transition and reverses the direction of the trajectory across the Brillouin zone. An analogous relationship holds between Fig. 1(c) and Fig. 1(d) when varying μ and Δ_s at fixed ϕ_s.

By writing the Hamiltonian in the type I 'periodic' representation with $s = 0$ we can calculate the Majorana number, Eq. (21), from which we find that the corresponding $\mathbb{Z}_2$ phase transition occurs when $\mu^2 + 4\Delta_s^2 \sin^2(\phi_s) = 4v^2$, the same transition predicted by Eq. (33) between CDW and Kitaev-like phases. Hence we expect that there would be MZM in the Kitaev-like phases, but not the CDW-like phases.

C. Solitons in the minimal Z_4 model

While the topological nature of the Majorana boundary between Kitaev-like and CDW-like phases is well understood [1], the additional phase transitions at $\mu = 0$ in CDW-like phases and $\cos\phi_s = 0$ in Kitaev-like phases are not. To provide further evidence of the topological nature for these transitions we introduce solitons into the system, where a texture in parameter values hosts a zero-energy state that is topologically protected by the symmetries of the system [39–41, 46, 87]. Consider an atomically smooth soliton in the chemical potential described by the function

$$\mu_l = -\mu_{\max}\tanh\left(\frac{l - N - 1/2}{\zeta}\right) + \mu_c\,, \tag{36}$$

for atomic site $l = 1, 2, ..., J$, where $\mu_{\max}$ is the magnitude of the texture at infinity for $\mu_c = 0$, $N = J/2$ is the number of unit cells, and ζ is the soliton width in dimensionless units, i.e., measured in units of the lattice constant. Here, μ_c is a constant dependent on the other parameters of the system and is used to shift all values of the soliton across the chain. This is needed for systems with higher order parameters with transitions that do not occur at $\mu = 0$, as discussed in Sec. VII E. For the minimal model we consider here, we set $\mu_c = 0$ such that the soliton is centered on $\mu = 0$.

Disorder is applied identically in the electron chain to the hole chain, in this way the symmorphic charge-conjugation symmetry is maintained regardless of disorder strength. As the solitons break translational invariance they also weaken the nonsymmorphic symmetries, however, for a large enough system size and width ζ the symmetry is approximately maintained, allowing the solitons to remain localized [44, 45, 52, 61, 88, 89]. We plot the position space energy levels as a function of ϕ_s for 48 unit cells, Fig. 9(a) with parameter values $\mu = 1$, $\Delta_s = 1$, and $v = 0.3$. As $4v^2 < \mu^2$ there is no value of ϕ_s that places the system in a Kitaev-like phase, hence there is an energy gap for all values of ϕ_s. Replacing the constant chemical potential of Fig. 9(a) with a texture described by Eq. (36) with $\mu_{\max} = 1$ and $\zeta = N/4 = 12$ results in the energy levels of Fig. 9(b). We find that the addition of the texture has removed the energy gap located in the CDW-like phases, with zero energy states exponentially localized onto the center of the chain where $\mu \approx 0$. Therefore, the soliton marks the boundary between CDW-like phases $N_{\mathrm{D}}^{\mathrm{NS}} = 2$ and $N_{\mathrm{D}}^{\mathrm{NS}} = 4$, Fig. 7(d). An example soliton state highlighting the exponential localization at the center of the chain is shown in Fig. 10(a), with $\mu_{\max} = 1$, $\Delta_s = 1$, $v = 0.3$, and $\phi_s = \pi/2$.

We also consider the case of a smooth soliton in ϕ_s described by the function

$$\phi_{s,n} = \frac{\phi_{s,\max}}{2}\left(1 + \tanh\left(\frac{n - N}{\zeta}\right)\right) + \phi_{s,c}\ , \tag{37}$$

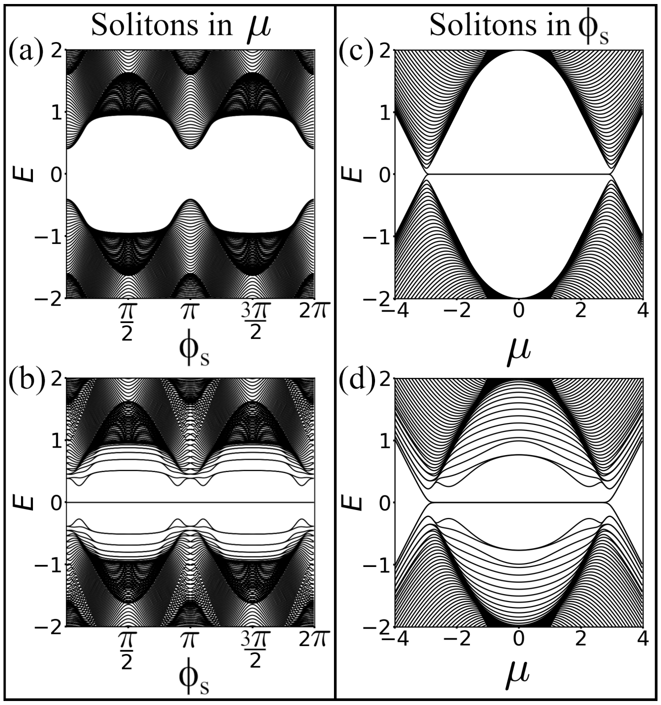

FIG. 9. Energy levels in the $\mathbb{Z}_4$ model in position space for 48 unit cells. (a) Position space energy levels as a function of the superconducting phase ϕ_s, parameter values are $\Delta_s = 1$, $v = 0.3$, and $\mu = 1$. (b) Position space energy levels of (a) in the presence of a soliton in the chemical potential with $\mu_{\max} = 1$ and $\zeta = N/4 = 12$. (c) Position space energy levels for 48 unit cells with no solitons as a function of the chemical potential μ, parameter values are $\Delta_s = 1$, $v = 1.5$, and $\phi_s = \pi/4$. (d) Position space energy levels of (c) in the presence of a soliton in the superconducting phase with $\phi_{s,\max} = \pi$ and $\zeta = N/4 = 12$. In (d) there are four zero energy levels in total, with two localized onto the ends of the chain and two localized on the solitons.

where $\phi_{s,\max}$ is the magnitude of the texture at infinity, and $n = 1, 2, ..., J-1$ is an index representing the position between adjacent atomic sites. For the minimal model we consider here, we set $\phi_{s,c} = 0$ such that the soliton is centered on $\phi_s = \phi_{s,\max}/2$. We plot the position space energy levels for 48 unit cells in the absence of solitons, now as a function of μ, Fig. 9(c). For parameter values $\Delta_s = 1$, $v = 1.5$, and $\phi_s = \pi/4$ we find a topological phase transition at $|\mu| = 2$ and MZM in the region $|\mu| < 2$, as predicted in Fig. 7(d). Adding a texture in ϕ_s described by Eq. (37) for $\phi_{s,\max} = \pi$ and $\zeta = N/4$, we obtain the energy levels as shown in Fig. 9(d). There are now four near-zero energy states in addition to the two MZM. While the Majorana states are exponentially localized onto the edges of the chain, the additional states are localized at the center of the chain where $\phi_s \approx \pi/2$, the same parameter value predicting the phase transition between Kitaev-like phases $N_{\mathrm{D}}^{\mathrm{NS}} = 1$ and $N_{\mathrm{D}}^{\mathrm{NS}} = 3$. An example probability density for $\phi_{s,\max} = \pi$, $\Delta_s = 1$, $v = 1.5$, and $\mu = 1$ is shown in Fig. 10(b).

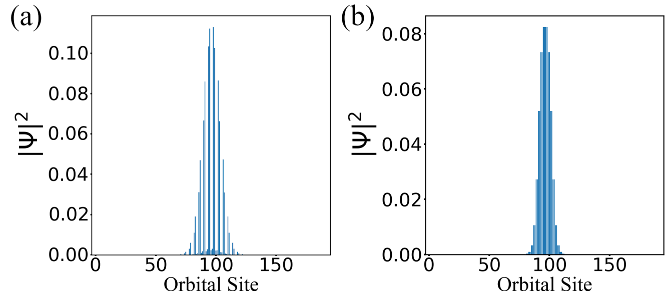

FIG. 10. Probability densities of near zero-energy soliton states exponentially localized onto the center of a chain of 48 unit cells. (a) A system with a soliton in the chemical potential between CDW-like phases $N_{\mathrm{D}}^{\mathrm{NS}} = 2$ and $N_{\mathrm{D}}^{\mathrm{NS}} = 4$, with parameter values $\Delta_s = 1$, $v = 0.3$, $\phi = \pi/2$, and $\mu_{\max} = 1$. (b) A system with a soliton in the superconducting phase between Kitaev-like phases $N_{\mathrm{D}}^{\mathrm{NS}} = 1$ and $N_{\mathrm{D}}^{\mathrm{NS}} = 4$, with parameter values $\Delta_s = 1$, $v = 1.5$, $\mu = 2$, and $\phi_{s,\max} = \pi$. In both systems there exists a second state localized onto the soliton with opposite energy, for the system in (b) there also exist two Majorana zero-modes localized onto the ends of the chain.

D. Disorder in the minimal $\mathbb{Z}_4$ model

In general the nonsymmorphic symmetries are not robust to disorder, although we can build random matrices that preserve the nonsymmorphism as discussed in Sec. IV. Here we introduce disorder in the chemical potential through the addition $\delta\mu_l$ to the lth atomic site in the particle chain, as described by the Gaussian-correlated potential [88, 90, 91] given by

$$\delta\mu_l = \frac{\sum_m w_m \exp(-|l-m|^2/\eta^2)}{\sqrt{\sum_m \exp(-|l-m|^2/\eta^2)}}, \tag{38}$$

where η is the correlation length in dimensionless units. The summation is over all atomic sites $m = 1, 2, ..., 2N$ with w_m drawn randomly from a uniform distribution $-W \leq w_m \leq W$ with disorder strength W. This allows for atomically sharp disorder within a sample for the case of $\eta \ll 1$ and sample-to-sample variations for $\eta \gg N$ across an ensemble. We find that sample-to-sample disorder does not affect topologically protected zero modes in this model, as for each variation in the ensemble the symmetries are not broken, hence we focus here on atomically sharp disorder within each member of the ensemble. In this way chosen parameters can be effectively randomized across the length of the chain. This breaks the nonsymmorphic symmetry that relies on translational invariance, while maintaining the symmorphic charge-conjugation symmetry that protects the MZM localized onto the ends of the chain in Kitaev-like phases. We can also use the right hand side of Eq. (38) to calculate disorder terms for the hopping parameter δv_l and the superconducting phase $\delta\phi_{s,l}$. We plot the density of states (DOS) for these finite systems numerically by approximation in Fig. 11 using a Lorentzian of finite

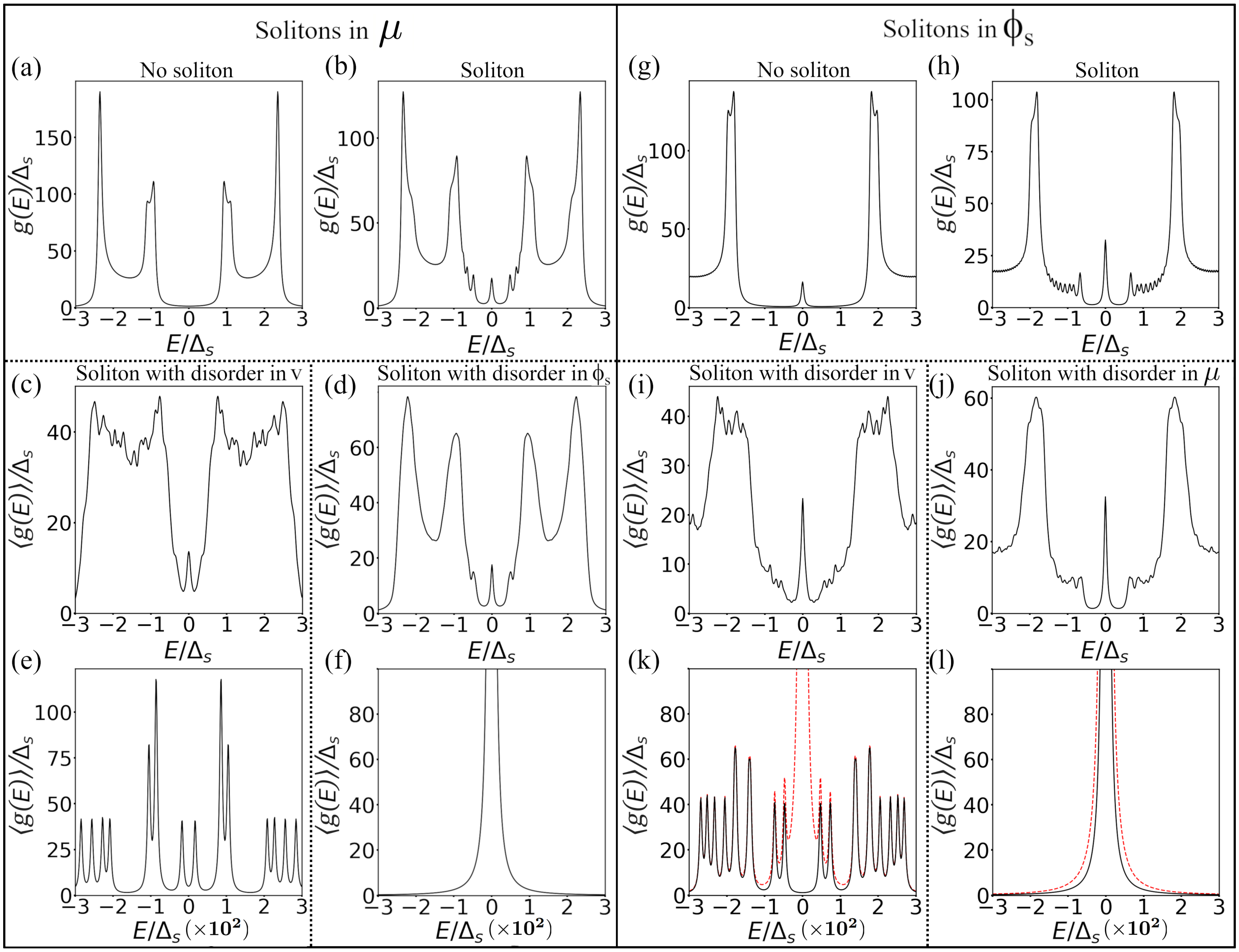

FIG. 11. Density of states (DOS) for various systems of the $\mathbb{Z}_4$ model in position space with 48 unit cells. (a) The DOS in the phase $N_{\mathrm{D}}^{\mathrm{NS}} = 4$ with $\mu = 1$, $v = 0.3$, $\Delta_s = 1$ and $\phi_s = \pi/4$, (b) is for the same system but in the presence of a soliton in the chemical potential with $\mu_{\max} = 1$ and width $\xi = 12$. Figures (c)-(f) detail the DOS once disorder has been introduced to (b). (c) and (d) show the DOS for atomically sharp disorder in v and ϕ_s, respectively. (e) and (f) show the same disorder as (c) and (d) but for small energy of order $\Delta_s \times 10^{-2}$ for disorder in v and ϕ_s, respectively. (g) The DOS in the phase $N_{\mathrm{D}}^{\mathrm{NS}} = 3$ with $\mu = 1$, $v = 1.5$, $\Delta_s = 1$, and $\phi_s = \pi/4$, (h) is for same system but in the presence of a soliton in the superconducting phase with $\phi_{s,\max} = \pi$ and width $\xi = 12$. Figures (i)-(l) detail the DOS once disorder has been introduced to (h), (i) and (j) show atomically sharp disorder in v and μ, respectively. (k) and (l) show the same disorder as (i) and (j) for a small energy of order $\Delta_s \times 10^{-2}$ in v and μ, respectively. A broadening width of $\xi = 0.04\Delta_s$ was used for Figures (a)-(d) and (g)-(j), and $\xi = 0.0004\Delta_s$ for figures (e)-(f) and (k)-(l). For plots with disorder we average over 20 disorder realizations with a disorder magnitude of $W = 0.5$ and parameter $\eta = 0.05$, resulting in strong atomically sharp disorder within each sample.

width ξ,

$$g(E) = \frac{1}{\pi}\sum_n \frac{\xi}{(E-E_n)^2+\xi^2}. \qquad (39)$$

We first plot the DOS with width $\xi = 0.04\Delta_s$ for a system of 48 unit cells, with no solitons or MZM and no disorder. This system resides in the phase $N_{\mathrm{D}}^{\mathrm{NS}} = 4$ with parameter values $\mu = 1$, $v = 0.3$, $\Delta_s = 1$, and $\phi_s = \pi/4$ and is shown in Fig. 11(a). As expected the DOS is zero at zero energy, indicating the absence of any zero-energy states. Fig. 11(b) shows the DOS for the same system after a soliton in the chemical potential is added with $\mu_{\max} = 1$. There is now a small but distinct peak in the DOS at zero energy, corresponding to a zero energy soliton exponentially localized at the center of the chain, as depicted in Fig. 9(c). While maintaining the soliton we now also introduce atomically sharp disorder with $\eta = 0.05$: The disorder averaged DOS are shown in Fig. 11(c) and Fig. 11(d) for disorder in v and ϕ_s, respectively. For all DOS plots with disorder we average over 20 disorder realizations. As the disorder breaks the translational invariance of the system and hence the nonsymmorphic symmetries, we expect that the soliton states would delocalize into the bulk and move away from zero energy. However, Fig. 11(c) and Fig. 11(d) clearly show a zero-energy peak in the DOS.

To better understand the robustness of such soliton states we plot the disorder averaged DOS for small energy $\sim \Delta_s \times 10^{-2}$ with disorder in v and ϕ_s. Fig. 11(e) shows that disorder in v does delocalize the soliton state, increasing its energy away from zero. In contrast, Fig. 11(f) shows that disorder in ϕ_s does not delocalize the soliton, as the energy eigenvalues across the ensemble remain fixed at zero energy. This apparent robustness of the soliton in μ can be attributed to the presence of additional symmetries at precisely the point $\mu = 0$ at the center of the chain, namely, symmorphic chiral symmetry $U_S = \tau_0\sigma_z$ and TRS $U_T = \tau_x\sigma_z$, and nonsymmorphic charge-conjugation symmetry $U_C = \tau_0\sigma_y$. In position space, it is clear that the addition of disorder to the system breaks all the nonsymmorphic symmetries, but not the symmorphic symmetries, resulting in a model belonging to the BDI symmetry class. The soliton in μ remains in the case of disorder in ϕ_s as it is localized on a transition in the remaining symmorphic model that is not affected by the disorder, while that same transition is affected by disorder in v, resulting in the destruction of the soliton.

We repeat this procedure for the case of solitons in the superconducting phase ϕ_s by plotting the DOS with $\xi = 0.04\Delta_s$. We start with a system in the $N_{\mathrm{D}}^{\mathrm{NS}} = 3$ phase with no soliton and parameter values $\mu = 1$, $v = 1.5$, $\Delta_s = 1$, and $\phi_s = \pi/4$. As this is a Kitaev-like phase there are MZM localized onto the edges of the chain even in the absence of solitons. Fig. 11(g) shows the DOS for this pristine system, where the MZM are shown as a small but observable peak at zero energy. Adding a soliton in ϕ_s between the Kitaev-like phases $N_{\mathrm{D}}^{\mathrm{NS}} = 3$ and $N_{\mathrm{D}}^{\mathrm{NS}} = 1$, increases the magnitude of this peak, as can be seen in Fig. 11(h). Adding disorder to the hopping parameter v and chemical potential μ does not appear to significantly change the DOS, as shown in Fig. 11(i) and Fig. 11(j), respectively. Fig. 11(k) and Fig. 11(l) shows the disorder averaged DOS for small energy $\sim \Delta_s \times 10^{-2}$ for disorder in v and μ, respectively. As we are focused on the affect of disorder on the soliton states we separate the MZM from the DOS by representing their contribution with the red dashed line in Fig. 11(k) and 11(l). In Fig. 11(k), it is clear that the disorder in v has delocalized the soliton state and moved its energy away from zero, while disorder in μ has not, with the soliton remaining at zero energy. This can again be explained by the presence of additional symmorphic symmetries exactly at the center of the soliton with $\phi_s = \pi/2$, namely, symmorphic chiral symmetry $U_S = \tau_y\sigma_0$ and time-reversal $U_T = \tau_z\sigma_0$, and nonsymmorphic charge conjugation $U_C = \tau_y\sigma_x$. To prevent the presence of symmorphic symmetries, we can add further parameters to the system that change the topological phase transitions.

E. Higher order parameters in the $\mathbb{Z}_4$ model

So far we have only considered the minimal required parameters to realize the $\mathbb{Z}_4$ topology, and this has led to a surprising robustness of solitons localized on these transitions due to the presence of symmorphic symmetries exactly at these transition points. Within the system with time-reversal operator $U_T = \tau_0\sigma_x$, there are two first-order parameters from Hamiltonian (3) that have not been added (excluding complex phases). These are t_{AA} and Δ_p with $t_{BB} = t_{AA}$ and $\Delta_p' = \Delta_p$, and here we focus on the addition of Δ_p. If we consider the simple case of switching off the s-wave superconducting parameter Δ_s and switching on the p-wave parameter Δ_p, we find that the $\mathbb{Z}_4$ model is reduced to a $\mathbb{Z}_2$ index due to the creation of unitary symmetries. However, unlike typical superconductors in the symmorphic D class such as the Kitaev chain [1], having both Δ_s and Δ_p be non-zero results in a distortion of the topological phase transitions between $N_{\mathrm{D}}^{\mathrm{NS}} = 1$ and $N_{\mathrm{D}}^{\mathrm{NS}} = 3$ and between $N_{\mathrm{D}}^{\mathrm{NS}} = 2$ and $N_{\mathrm{D}}^{\mathrm{NS}} = 4$, although, as expected, the Majorana phase transition remains unchanged. Introducing Δ_p to the Hamiltonian (31) keeps the noninteracting part the same but results in a new coupling matrix of

$$\hat{\Delta}(k) = \begin{pmatrix} 2i\Delta_p \sin(ka) & 2i\Delta_s \sin(ka/2 + \phi_s) \\ 2i\Delta_s \sin(ka/2 - \phi_s) & 2i\Delta_p \sin(ka) \end{pmatrix}.$$

Analytically deriving the topological transition points is non-trivial, and is discussed in detail in the supplementary material [82]. We also include in the supplementary material the derivation of topological transition points for a Hamiltonian that includes the hopping parameter t_{AA}. Here, we examine the effect of disorder on the DOS for systems with solitons, where the zero energy states are localized on domain walls corresponding to the new transition points once Δ_p coupling is accounted for. The disorder-averaged DOS for small energy $\sim \Delta_s \times 10^{-2}$ is shown in Fig. 12. We first examine the case of solitons in μ between $N_{\mathrm{D}}^{\mathrm{NS}} = 2$ and $N_{\mathrm{D}}^{\mathrm{NS}} = 4$ as we previously did for a minimal model, Fig. 11(a)-(f) for a soliton localized on $\mu = 0$. Due to the introduction of the parameter Δ_p, the value of μ which corresponds to a phase transition has shifted. For a system with $\Delta_p = 0.5$, $v = 0.3$, $\Delta_s = 1$, and $\phi = \pi/4$, we find that the phase transition occurs at $\mu \approx -0.255$ [82]. This can be accounted for in the soliton texture, Eq. (36), by setting $\mu_c = -0.255$. In this way the zero-energy state remains localized on the soliton at the center of the chain. The disorder-averaged DOS for this system and disorder in v and ϕ_s are shown in Fig. 12(a) and Fig. 12(b), respectively. Similarly to the minimal model with disorder in v, Fig. 11(e), the DOS for a system with non-zero Δ_p and disorder in v has multiple peaks near zero energy, rather than a single larger peak at exactly zero energy. However, in the case of the minimal model we found the soliton state to be especially robust to the presence of disorder in ϕ_s, Fig. 11(f), remaining at zero energy. In contrast to this, the presence of Δ_p shifts the states from zero energy, Fig. 12(b), and

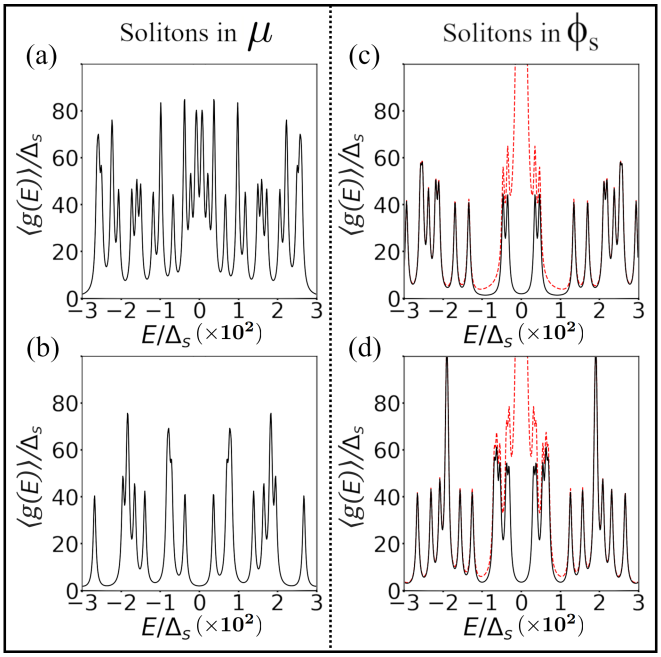

FIG. 12. Density of states (DOS) for small energy of order $\Delta_s \times 10^{-2}$ for various systems of the $\mathbb{Z}_4$ model in position space with 48 unit cells and in the presence of a Δ_p order parameter. In each of these systems solitons are present of width $\xi = 12$ in addition to disorder of strength $W = 0.5$. (a) The DOS for a system with a soliton in the chemical potential between phases $N_{\mathrm{D}}^{\mathrm{NS}} = 2$ and $N_{\mathrm{D}}^{\mathrm{NS}} = 4$ and centered on $\mu_c = -0.255$, with disorder in the hopping parameter v and with parameter values $\Delta_s = 1$, $\Delta_p = 0.5$, $v = 0.3$, $\phi_s = \pi/4$, and $\mu_{\max} = 1$. (b) DOS for the same system as (a) but in the presence of disorder in ϕ_s. (c) The DOS for a system with a soliton in the superconducting phase between phases $N_{\mathrm{D}}^{\mathrm{NS}} = 1$ and $N_{\mathrm{D}}^{\mathrm{NS}} = 3$ and centered on $\phi_{s,c} = 2.02$, with disorder in the hopping parameter v and with parameter values $\Delta_s = 1$, $\Delta_p = 0.5$, $v = 1.5$, $\mu = 1$, and $\phi_{s,\max} = \pi$. (d) DOS for the same system as (a) but in the presence of disorder in μ.

can be attributed to the fact that additional symmorphic symmetries don't appear at the transition point anymore.

We plot the disorder averaged soliton energy for a soliton in the chemical potential μ against the value of Δ_p in Fig. 13, represented as a log-log plot with error bars showing ± 1 standard deviation from the mean. Each point is averaged across an ensemble of 20 disorder realizations for disorder in the superconducting phase ϕ_s with disorder strength $W = 0.5$. The approximately linear behavior indicates a power law relation between the value of Δ_p and the raising of the soliton energy level from zero energy. This can be attributed to Δ_p breaking the symmorphic symmetries induced at $\mu = 0$ and $\Delta_p = 0$.

We also examine solitons in ϕ_s between phases $N_{\mathrm{D}}^{\mathrm{NS}} = 1$ and $N_{\mathrm{D}}^{\mathrm{NS}} = 3$, as we previously did for a minimal model as shown in Fig. 11(g)-(l) for a soliton localized on $\phi_s = \pi/2$. For a system with $\Delta_p = 0.5$, $v = 1.5$, $\Delta_s = 1$, and $\mu = 1$, we find that the phase transition occurs at $\phi_s \approx$

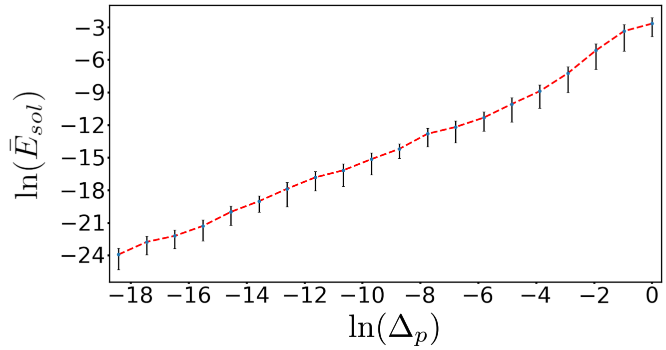

FIG. 13. Disorder averaged soliton energy for a soliton in the chemical potential μ in the $\mathbb{Z}_4$ model between phases $N_{\mathrm{D}}^{\mathrm{NS}} = 2$ and $N_{\mathrm{D}}^{\mathrm{NS}} = 4$, plotted against the magnitude of the superconducting order parameter Δ_p and represented as a log-log plot. Each point is averaged across an ensemble of 20 disorder realizations for disorder in the superconducting phase of strength $W = 0.5$. Error bars represent ranges of ± 1 standard deviation from the mean for each ensemble. The plot shows approximately linear behavior indicating a power law relation between increasing Δ_p and the raising of the soliton states from zero energy in the presence of disorder, which can be attributed to Δ_p breaking the symmorphic symmetries induced at $\mu = 0$ and $\Delta_p = 0$. Parameter values are $\mu_{\max} = 1$, $\Delta_s = 1$, $\phi_s = \pi/4$, and variable μ_c depending on the value of Δ_p.

2.02 [82]. This can be accounted for in the soliton texture, Eq. (37), by setting $\phi_{s,c} = 2.02$ such that the zero energy state remains localized on the soliton at the center of the chain. The disorder-averaged DOS for this system and disorder in v and μ are shown in Fig. 12(c) and Fig. 12(d), respectively. Similarly to the minimal model with disorder in v, Fig. 11(k), the DOS for a system with non-zero Δ_p and disorder in v has multiple peaks near zero energy, rather than a single larger peak at exactly zero energy. However, in the case of the minimal model we found the soliton state to be especially robust to the presence of disorder in μ, Fig. 11(l), remaining at zero energy. In contrast to this, the presence of Δ_p shifts the states from zero energy, Fig. 12(d), and can be attributed to the fact that additional symmorphic symmetries don't appear at the transition point anymore.

F. System with $\mathbb{Z}_4$ index with $U_T = \tau_x\sigma_x$ and alternating onsite energy

So far we have only examined one possible realization of the $\mathbb{Z}_4$ model. Here, we briefly describe a model with nonsymmorphic time-reversal operator $U_T = \tau_x\sigma_x$. In comparison to the system with $U_T = \tau_0\sigma_x$ which has constant chemical potential, this system has alternating onsite energy similar to the CDW model [46, 61]. The

BdG Hamiltonian can be written as

$$\begin{aligned} H(k) &= \begin{pmatrix} \hat{h}(k) & \hat{\Delta}(k) \\ \hat{\Delta}^{\dagger}(k) & -\hat{h}^{T}(-k) \end{pmatrix}, \qquad (40) \\ \hat{h}(k) &= \begin{pmatrix} u & 2iv\sin(ka/2+\phi_v) \\ -2iv\sin(ka/2+\phi_v) & -u \end{pmatrix}, \\ \hat{\Delta}(k) &= \begin{pmatrix} 0 & 2\Delta_s\cos(ka/2) \\ -2\Delta_s\cos(ka/2) & 0 \end{pmatrix}, \end{aligned}$$

where, from the generalized Hamiltonian (3), we have set $w = -v$, $\phi_w = \phi_v$, and $\Delta_s' = -\Delta_s$. In general, the band structure for the first quantized Hamiltonian is an insulator, with energy eigenvalues

$$\begin{aligned} E^2 &= \mu^2 + f^2 + g^2 + S^2 \pm \sqrt{\mu^2 f^2 + S^2(f^2+g^2)}, \\ f(k) &= 2\Delta_s\cos(ka/2), \\ S(k) &= 2v\sin(\phi_v)\cos(ka/2), \\ g(k) &= 2v\cos(\phi_v)\sin(ka/2). \end{aligned}$$

For this example, we calculate the phases using the Pfaffian integral approach, finding that

$$Z(k) = \begin{pmatrix} u + 2iv\sin(ka/2+\phi_v) & 2\Delta_s\cos(ka/2) \\ -2\Delta_s\cos(ka/2) & -u - 2iv\sin(ka/2-\phi_v) \end{pmatrix}.$$

This results in phases

$$N_{\mathrm{D}}^{\mathrm{NS}} = \begin{cases} 1 & \text{if} \quad u^2+4v^2\sin^2(\phi_v) < 4\Delta_s^2 \quad \text{and} \quad \cos\phi_v > 0, \\ 2 & \text{if} \quad u^2+4v^2\sin^2(\phi_v) > 4\Delta_s^2 \quad \text{and} \quad u < 0, \\ 3 & \text{if} \quad u^2+4v^2\sin^2(\phi_v) < 4\Delta_s^2 \quad \text{and} \quad \cos\phi_v < 0, \\ 4 & \text{if} \quad u^2+4v^2\sin^2(\phi_v) > 4\Delta_s^2 \quad \text{and} \quad u > 0, \end{cases}$$

which clearly resembles the topology previously calculated for a system with $U_T = \tau_0\sigma_x$, as seen in the phase diagram Fig. 7(d).

VIII. TOPOLECTRIC CIRCUIT REALIZATION OF NONSYMMORPHIC MODELS

A. General setup and two-point impedance

The use of electric circuits to realize topological systems has been studied extensively [72–78], however, circuits representing nonsymmorphic models have not been explored. Here, we explicitly write out circuit realizations of the symmorphic SSH and Kitaev chain models and the nonsymmorphic CDW and $\mathbb{Z}_4$ models. In general, the electric current that flows into the ground and the voltage of an RLC circuit at node a are related by Kirchoff's law [76–78] as

$$\begin{aligned} \frac{d}{dt}I_a &= \sum_b \left[\left(C_{ab}\frac{d^2}{dt^2} + \frac{1}{L_{ab}} + \frac{1}{R_{ab}}\frac{d}{dt}\right)(V_a - V_b)\right] \\ &\quad + \left(C_a\frac{d^2}{dt^2} + \frac{1}{L_a} + \frac{1}{R_a}\frac{d}{dt}\right)V_a\,, \qquad (41) \end{aligned}$$

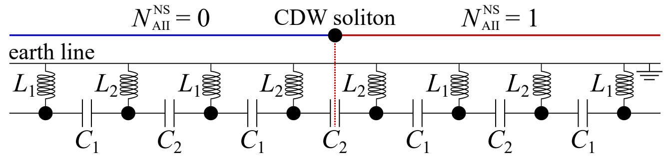

FIG. 14. Schematic of a topolectric circuit realization of the SSH and CDW models. Each node is connected to adjacent nodes with staggered capacitors C_1 and C_2 and connected to the ground through alternating inductors L_1 and L_2. The SSH phase is realized for $L_2 = L_1$ and the CDW phase for $C_1 = C_2$. In the CDW phase an atomically sharp soliton may be implemented by swapping the order of L_1 and L_2, as shown at the center of the diagram.

where I_a is the current between node a and the ground, V_a and V_b are the voltages at node a and b, C_{ab}, L_{ab}, and R_{ab} are the capacitance, inductance, and resistance between nodes a and b, C_a, L_a, and R_a are the capacitance, inductance and resistance at node a, and the sum is taken over all adjacent nodes b. We note that, by convention, we take C_{ab}, L_{ab}, R_{ab}, C_a, L_a, and R_a to be positive. By performing a Fourier transform $V(t) = V_0 e^{i\omega t}$, we can rewrite Eq. (41) as

$$I_a(\omega) = \sum_b J_{ab}(\omega)V_b(\omega), \qquad (42)$$

where

$$\begin{aligned} J_{ab}(\omega) &= i\omega\Bigg[-C_{ab} + \frac{1}{\omega^2 L_{ab}} + \frac{i}{\omega R_{ab}} + \delta_{ab}\Bigg(C_a - \frac{1}{\omega^2 L_a} \\ &\quad - \frac{i}{\omega R_a} + \sum_c\left[C_{ac} - \frac{1}{\omega^2 L_{ac}} - \frac{i}{\omega R_{ab}}\right]\Bigg)\Bigg], \qquad (43) \end{aligned}$$

where $J_{ab}(\omega)$ is the circuit Laplacian. The circuit Laplacian can be related to position-space tight-binding Hamiltonians $\mathcal{H}$ via the relation $J_{ab}(\omega) = i\omega H_{ab}(\omega)$, or, in k-space, as $J_{ab}(k) = i\omega H_{ab}(k)$. The topological equivalence of the circuit to the tight-binding Hamiltonian is confirmed by the experimentally measurable quantity of impedance under an applied current [78]. We inject an incoming current $I_a(\omega)$ into node a, resulting in an outgoing current $I_b(\omega) = I_a(\omega)$ at node b. The voltage difference between these two nodes then defines the two-point impedance as

$$Z_{ab}(\omega) = \frac{V_a(\omega) - V_b(\omega)}{I(\omega)} = \sum_n \frac{|\psi_{n,a} - \psi_{n,b}|}{j_n}\,, \qquad (44)$$

where we have diagonalized the circuit Laplacian to obtain eigenvalues j_n and corresponding eigenmodes with components $\psi_{n,a}$ at node a. When at least one eigenvalue j_n is small, Z_{ab} diverges provided that $\psi_{n,a} \neq \psi_{n,b}$. Therefore, edge states, MZM, and solitons may be detected by measuring the two-point impedance.

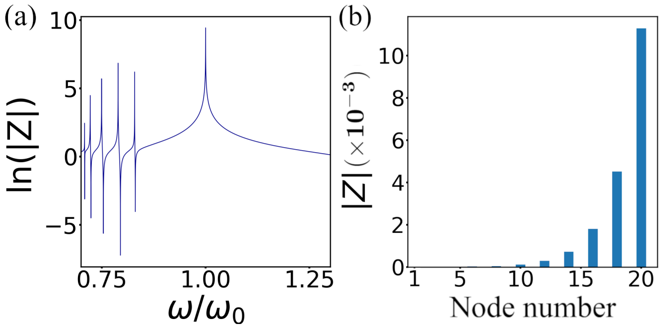

FIG. 15. Two-point impedance magnitudes across topolectric realizations of the SSH model with 20 nodes in the topological phase $C_1/C_2 = 0.4$ with edge states and current input at the first site in the chain. In (a) the output is at the edge state on the opposite end of the chain and the logarithm of the magnitude of the impedance $\ln(|\mathrm{Z}|)$ is plotted as a function of the frequency, while (b) shows the on-resonance impedance as a function of variable output node, where the value at site 20 corresponds to the peak in (a) at $\omega/\omega_0 = 1$.

B. Circuit realizations of the SSH and CDW models

The SSH and CDW models have circuit realizations that can be considered as different phases of one another. To see this, consider a chain of nodes connected by staggered capacitors C_1 and C_2 and grounded by inductors L_1 and L_2 that alternate along the chain at nodes A and B, respectively. With only these components, Eq. (43) reduces to the position space Hamiltonian

$$H_{ab}(\omega) = -C_{ab} + \delta_{ab}\left(-\frac{1}{\omega^2 L_a} + \sum_c C_{ac}\right), \qquad (45)$$

where $C_{ab} = C_1$ and $L_a = L_1$ for odd values of a and $C_{ab} = C_2$ and $L_a = L_2$ for even values of a. The SSH phase is realized when $L_2 = L_1$, such that for an infinite circuit in the type I representation ($s = 0$), this results in

$$H_{\mathrm{SSH}}(k) = \begin{pmatrix} C_1 + C_2 - \frac{1}{\omega^2 L_1} & C_1 + C_2 e^{-ika} \\ C_1 + C_2 e^{ika} & C_1 + C_2 - \frac{1}{\omega^2 L_1} \end{pmatrix}, \qquad (46)$$

where at the resonant frequency $\omega_0 = 1/\sqrt{L_1(C_1 + C_2)}$, the onsite terms are zero and we find exact agreement with the SSH model with $C_1 = -v$ and $C_2 = -w$. Therefore, for $C_1/C_2 < 1$, the model is in the topological regime and hosts edge states at zero energy on the ends of the chain, while, for $C_1/C_2 > 1$, the model is in the trivial phase. We note that, as C_1 and C_2 are both positive, we can not realize regimes with $C_1/C_2 < 0$, although this is possible by introducing subnodes into the system [78]. By varying the frequency ω across a system in the topologically non-trivial regime ($C_1/C_2 < 1$), we find that there is a distinct peak in the two point impedance between the two ends of the chain, where l is the last node in the chain, as predicted by Eq. (44) and shown in Fig. 15(a). This peak corresponds to the zero-energy edge state of the SSH model. In Fig. 15(b), we plot the two-point impedance for each node across the chain when the system is at the resonant frequency and for an input current injected at the first node. There is a distinct peak in the impedance at the end of the chain that matches the peak found in Fig. 15(a). Due to the underlying sublattice symmetry of the SSH model, the impedance is near-zero if the current output is on an A node and non-zero on B nodes [78].

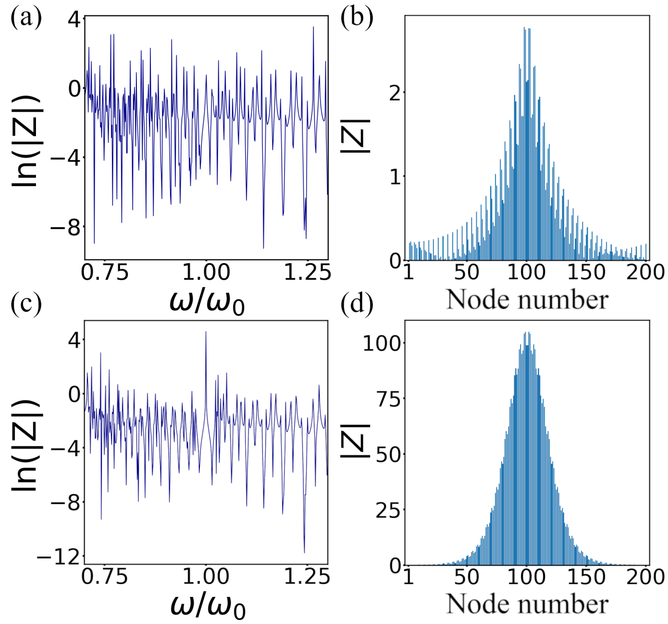

FIG. 16. Two-point impedance magnitudes across topolectric realizations of the CDW model with 200 nodes in the presence of a topological soliton between the two phases and with current input at the first site in the chain. (a) and (b) are for an atomically sharp soliton, Fig. 14, located at the center of the chain, (a) is the logarithm of the magnitude of the impedance $\ln(|\mathrm{Z}|)$ plotted as a function of the frequency with current output at the position of the soliton at the center of the chain. (b) is a plot of the on-resonance impedance as a function of output node, where the peak at the center of the chain corresponds to the peak in (a) at $\omega/\omega_0 = 1$. (c) and (d) are for the same system as (a) and (b), but in the presence of an atomically smooth soliton of width $\zeta = 50$. We find a significantly larger peak in the impedance for a smooth soliton when compared to the sharp soliton in (a) and (b). Figures (a) and (b) use parameter values $C_1 = 10$F, $L_1 = 0.2$H, and $L_2 = 0.21$H and (c) and (d) use $C_1 = 10$F, $u_{\max} = 1$.

The CDW phase is realized by setting $C_2 = C_1$ in Eq. (45). For an infinite circuit in the type II representation ($s = a/2$), this results in

$$H_{\mathrm{CDW}}(k) = \begin{pmatrix} 2C_1 - \frac{1}{\omega^2 L_1} & C_1 \cos(ka/2) \\ C_1 \cos(ka/2) & 2C_1 - \frac{1}{\omega^2 L_2} \end{pmatrix}. \qquad (47)$$

The CDW model is characterized by an alternating onsite energy $\pm u$ which we obtain by setting $u = 2C_1 -$

$1/\omega^2 L_1 = -2C_1 + 1/\omega^2 L_2$, a condition satisfied by the resonant frequency

$$\omega_0 = \frac{1}{2}\sqrt{\frac{1}{C_1 L_1} + \frac{1}{C_1 L_2}}\,. \tag{48}$$

The constant hopping of the CDW model is related to the capacitance as $C_1 = v$. At the resonant frequency, the two topological phases are then defined by whether $2C_1 - 1/\omega^2 L_1 > 0$ ($N^{\mathrm{NS}}_{\mathrm{AI}} = 0$) or $2C_1 - 1/\omega^2 L_1 < 0$ ($N^{\mathrm{NS}}_{\mathrm{AI}} = 1$). While the CDW model does not have zero energy edge states, it can host a zero energy state exponentially localized onto a soliton between the two phases [46]. An atomically sharp soliton can be implemented by swapping the values of L_1 and L_2 at the center of the chain. The two point impedance for current injected at the edge of the chain and with current output at the center of the chain is shown as a function of the frequency ω in Fig. 16(a). A sharp peak in the impedance is found at the resonant frequency, and we find that the magnitude of the peak is small when compared to the SSH model, Fig. 15, due to the nonsymmorphic symmetry only being approximate in the presence of a soliton, requiring large system sizes to be close to zero energy [46]. We also plot the two-point impedance for current injected at the edge of the chain for each node in the chain in Fig. 16(b). This shows a distinct peak in the impedance at the position of the soliton at the center of the chain.

Although more difficult to implement experimentally, requiring careful tuning of circuit components, a larger peak in the impedance may be realized by considering an atomically smooth soliton in the onsite terms. By fixing the frequency as $\omega = \omega_0$, we can define a smooth soliton by continuously changing the value of L_a according to

$$L_a = \left[\omega_0^2\left(2C_1 - (-1)^a u_{\max}\tanh\left(\frac{a-(N+1)/2}{\zeta}\right)\right)\right]^{-1},$$

where $u_{\max}$ is the value of the alternating onsite energy at infinity, N is the number of nodes, and ζ is the soliton width. This results in a significantly larger peak in the impedance as there are eigenvalues j_n closer to zero energy when compared to an atomically sharp soliton [46]. We show this in Fig. 16(c) as a function of the frequency for current injected at the first node and with output current at the center of the chain, where a significantly larger peak at $\omega = \omega_0$ is shown as compared to Fig. 16(a). In Fig. 16(d), the two-point impedance for current injected at the first node as a function of output node is shown, and the impedance peaks at the center of the chain at the position of the soliton.

We note that it is also possible to build a CDW circuit by alternating the grounding component from capacitors to inductors, however, this can not realize a phase of the SSH model.

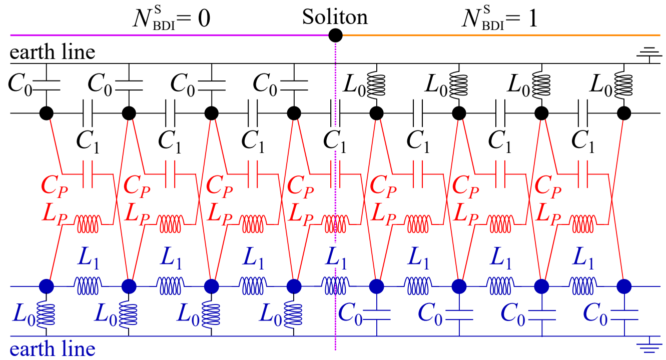

FIG. 17. Topolectric circuit realization of the Kitaev model with real superconducting pairing, a soliton causes a phase transition from topologically trivial ($N^{\mathrm{S}}_{\mathrm{BDI}} = 0$) to non-trivial ($N^{\mathrm{S}}_{\mathrm{BDI}} = 1$). The model is simulated by two channels, the upper channel (black) represents the electron chain and the lower channel (blue) represents the hole chain. The chains are grounded by either inductors L_0 or capacitors C_0 depending on the topological phase, nodes in the same channel are connected by inductors L_1 and capacitors C_1, and the channels are paired to one-another (red) by inductors L_P and capacitors C_P [76, 77].

C. Circuit realizations of the Kitaev and $\mathbb{Z}_4$ models

Circuit realizations of the Kitaev chain and the $\mathbb{Z}_4$ model closely resemble one another, and may be used as a comparison between topolectric circuits with symmorphic and nonsymmorphic symmetries, respectively. The Kitaev chain can be modeled with two coupled channels as shown in Fig. 17, where the upper channel represents the 'electron' nodes and the lower channel represents the 'hole' nodes [76, 77]. A soliton at the center of the chain marks the boundary between a topologically trivial phase ($N^{\mathrm{S}}_{\mathrm{BDI}} = 0$) and a topologically non-trivial phase ($N^{\mathrm{S}}_{\mathrm{BDI}} = 1$). The electron (hole) channel is grounded by inductors L_0 (capacitors C_0) in the non-trivial phase and capacitors C_0 (inductors L_0) in the trivial phase. Nodes within the electron (hole) channel are connected by capacitors C_1 (inductors L_1), and the two channels are coupled by capacitors C_P and inductors L_P. The Hamiltonian can be derived by Fourier transforming the position space circuit Laplacian, Eq. (43), and reduces exactly to the Kitaev chain at the resonant frequency,

$$\omega_0 \equiv 1/\sqrt{L_0 C_0} = 1/\sqrt{L_1 C_1} = 1/\sqrt{L_P C_P}\,. \tag{49}$$

The resulting k-space Hamiltonian can be written in the type I representation as

$$H_{\mathrm{Kit}}(k) = \begin{pmatrix} h(k) & g(k) \\ g^*(k) & -h^*(k) \end{pmatrix}, \tag{50}$$

where

$$\begin{aligned} h(k) &= -2C_1\cos(ka) + 2C_1 + \xi_t C_0, \\ g_1 &= -2iC_P\sin(ka), \end{aligned}$$

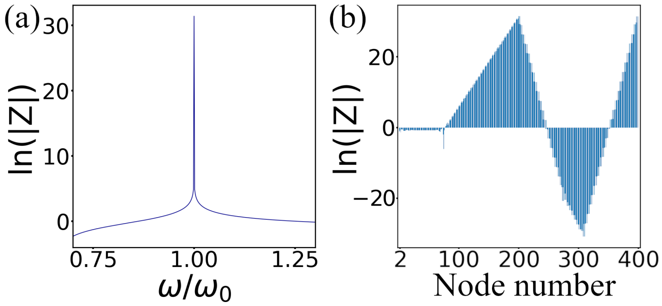

FIG. 18. Impedances across the topolectric realization of the Kitaev chain, Fig. 17, for 400 nodes and a soliton between phases $N^{\rm S}_{\rm BDI} = 0$ and $N^{\rm S}_{\rm BDI} = 1$. (a) shows the impedance as a function of the input frequency where the current is inputted into the first node in the electron channel and outputted at the soliton at center of the chain. (b) shows the on-resonance impedance as a function of output node, the central peak corresponds to the same peak in (a). Parameter values are $L_0 = 0.4$H, $C_0 = 0.2$F, $L_1 = 0.4$H, $C_1 = 0.2$F, $L_P = 0.3$H, $C_P = 0.267$F.

where

$$\xi_t = \begin{cases} 1 & \text{if} \quad N^{\rm S}_{\rm BDI} = 0\,, \\ -1 & \text{if} \quad N^{\rm S}_{\rm BDI} = 1\,, \end{cases} \tag{51}$$

such that the onsite energy $\mu = -2C_1 + \xi_t C_0$, hopping $v = -C_1$, and pairing $\Delta_s = C_P$.

The Kitaev chain is topologically trivial for $|\mu| > |2v|$ and non-trivial for $|\mu| < |2v|$. Therefore, flipping the sign of ξ_t by swapping the grounding component in the electron (hole) chain from a capacitor (inductor) to an inductor (capacitor) causes a topological phase transition between $N^{\rm S}_{\rm BDI} = 0$ and $N^{\rm S}_{\rm BDI} = 1$. Taking a finite chain where the grounding components are swapped at the center of the chain, Fig. 17, results in a soliton that hosts zero-energy modes. These zero-energy modes result in large measurable peaks in the impedance according to Eq. (44). We plot the impedance as a function of the frequency in Fig. 18(a) for 400 nodes, with an input current at the first site in the chain and an output current at the soliton node at the center of the chain. We also plot the on-resonance impedance for an input current at the first node in the chain and with variable output node in Fig. 18(b), which shows large peaks in the impedance at the edges of the topologically non-trivial section of the chain. It is also possible to include an arbitrary phase in the pairing parameters between the two channels [77]. Although this is useful for braiding of MZM we do not include this here, as, for a single chain, the phase can be gauged away and does not affect the topology of the system.

In contrast to the Kitaev chain the alternating phases of the $\mathbb{Z}_4$ model can not be gauged away [71], and must be accounted for when constructing a topolectric circuit. Example circuit realizations of the $\mathbb{Z}_4$ model for each possible topological phase are shown in Fig. 19, where the inter-channel components of the Kitaev chain are replaced by phase-control units (PCU), the structure of which is shown in Fig. 20. Phase transitions are controlled by a change in the grounding inductance from L_1 to L'_1 and grounding capacitance from C_0 to C'_0, Fig. 19(a), or by a change in the PCU from ϕ_1 (ϕ'_1) to ϕ_2 (ϕ'_2), Fig. 19(b). The resonant frequency is identical to that of the Kitaev chain, Eq. (49), such that, at this frequency, all possible circuit components the k-space Hamiltonian can be written in the same form as Eq. (3) with

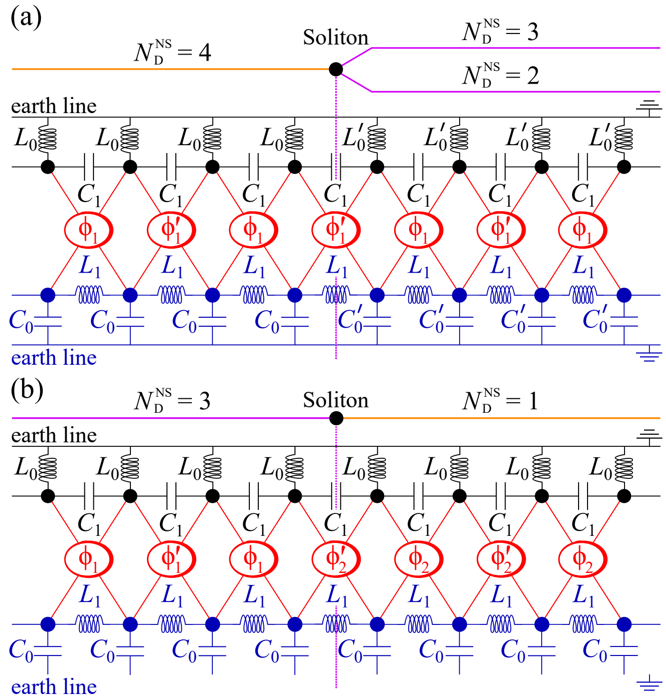

FIG. 19. Examples of topolectric circuit realizations of the $\mathbb{Z}_4$ model. The model is simulated by two channels, the upper channel (black) represents the electron chain and the lower channel (blue) represents the hole chain. The chains are grounded by a topological control unit that may be switched 'on' or 'off' to elicit a phase transition, nodes in the same channel are connected by inductors L_1 and capacitors C_1, and the channels are paired to one-another (red) by phase control units [76, 77]. In (a) a soliton in the phase control unit causes a phase transition from $N^{\rm NS}_{\rm D} = 3$ to $N^{\rm NS}_{\rm D} = 1$. In (b) a soliton in the topological control unit causes a phase transition from either $N^{\rm NS}_{\rm D} = 2$ or $N^{\rm NS}_{\rm D} = 3$, depending on the value of other parameters, to $N^{\rm NS}_{\rm D} = 4$. Each form phase control unit is shown in Fig. 20.

$$h_1(k) = h_3(k) = 2C_1 - C_0\,, \tag{52}$$

$$h_2(k) = -2C_1\cos(ka/2)\,, \tag{53}$$

$$\Delta_1(k) = \Delta_3(k) = 0\,, \tag{54}$$

$$\Delta_2(k) = \left(\eta_t C_P + \frac{i\sqrt{L_P C_P}}{R_P}\right) e^{ika/2} - \left(\eta_t C_P - \frac{i\sqrt{L_P C_P}}{R_P}\right) e^{-ika/2}\,, \tag{55}$$

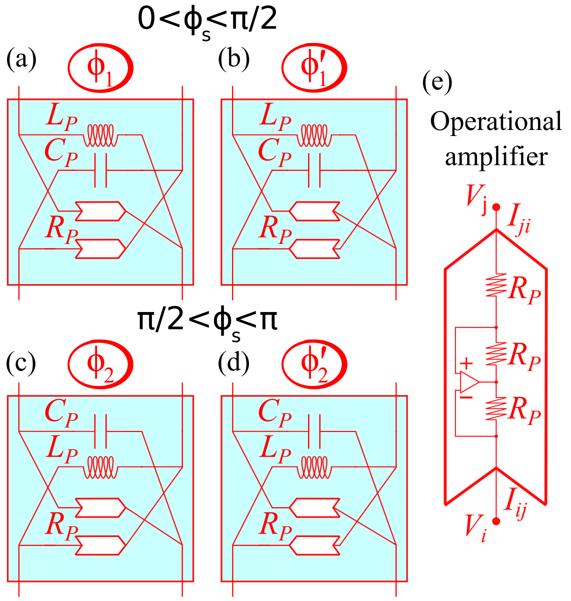

FIG. 20. Circuit diagrams of the phase-control units (PCU) used in Fig. 19. There are four forms of PCU, (a) and (b) show the intracell and intercell PCUs, respectively, which mimic the superconducting pairing $\Delta_s' = \Delta_s$ with phase $\phi_s' = -\phi_s$ found in Hamiltonian (3) for $0 < \phi_s < \pi/2$. Figures (c) and (d) correspond to the same parameters as (a) and (b), respectively, but for $\pi/2 < \phi_s < \pi$. Figure (e) shows the structure of the operational amplifier used in (a)-(d).

where C_0 is interchangeable with C_0' and

$$\eta_t = \begin{cases} 1 & \text{if} \quad \text{PCU} = \phi_1\,, \\ -1 & \text{if} \quad \text{PCU} = \phi_2\,. \end{cases} \tag{56}$$

From this, we can compare the components to the parameters of the $\mathbb{Z}_4$ Hamiltonian, Eq. 31, as

$$\begin{aligned} \mu &= -2C_1 + C_0\,, &(57)\\ v &= -C_1\,, &(58)\\ \Delta_s &= C_P^2 + L_P C_P / R_P^2\,, &(59)\\ \phi_s &= \arg\left[\eta_t C_P + i\sqrt{L_P C_P}/R_P\right]\,. &(60) \end{aligned}$$

Substituting these expressions into the phase transitions shown in Fig. 7(d) we find that

$$N_{\mathrm{D}}^{\mathrm{NS}} = \begin{cases} 1 & \text{if} \;\; X < 0 \text{ and } Y > 0\,, \\ 2 & \text{if} \;\; X > 0 \text{ and } Z < 0\,, \\ 3 & \text{if} \;\; X < 0 \text{ and } Y < 0\,, \\ 4 & \text{if} \;\; X > 0 \text{ and } Z > 0\,, \end{cases} \tag{61}$$

where

$$X = C_0^2 - 4C_1C_0 + \frac{4L_PC_P}{R_P^2}, \tag{62}$$

$$Y = \eta_t C_P \left(\sqrt{\frac{L_PC_P}{R_P^2} + C_P^2}\right)^{-1}, \tag{63}$$

$$Z = \mu = -2C_1 + C_0\,. \tag{64}$$

We can select parameter values such that by swapping C_0 for C_0' we can flip the sign of X or Z, resulting in a phase transition between $N_{\mathrm{D}}^{\mathrm{NS}} = 4$ and $N_{\mathrm{D}}^{\mathrm{NS}} = 3$ or between $N_{\mathrm{D}}^{\mathrm{NS}} = 4$ and $N_{\mathrm{D}}^{\mathrm{NS}} = 2$ at the position in the chain that this swap occurs, Fig. 19(a). Similarly, we can swap the PCU ϕ_1 (ϕ_1') for ϕ_2 (ϕ_2') which flips the sign of Y, resulting in a transition between phases $N_{\mathrm{D}}^{\mathrm{NS}} = 3$ and $N_{\mathrm{D}}^{\mathrm{NS}} = 1$. We note that the solitons shown in Fig. 19 are example transitions, and, alternatively, there may be different phase transitions or no phase transition depending on the parameter values.

Taking finite chains, with topological transitions occurring at the center of the chain, results in zero-energy states hosted on solitons and corresponding peaks in the impedance that are localized onto the solitons according to Eq. (44). We first plot the impedance for a system with 400 nodes, current input at the first site in the 'electron' channel, and a soliton between $N_{\mathrm{D}}^{\mathrm{NS}} = 4$ and $N_{\mathrm{D}}^{\mathrm{NS}} = 3$ as a function of frequency in Fig. 21(a). Here a large peak is observed at the resonant frequency. For the same system as Fig. 21(a), we plot the impedance as a function of the output node, where peaks are observed at the edges of the $N_{\mathrm{D}}^{\mathrm{NS}} = 3$ section of the chain which hosts MZM. By deforming the parameter values, the transition may then be between $N_{\mathrm{D}}^{\mathrm{NS}} = 4$ and $N_{\mathrm{D}}^{\mathrm{NS}} = 2$. As neither side of this transition is in a phase that hosts MZM, the only contribution to the impedance peak is from the soliton. Fig. 21(c) shows that the on-resonance peak for current output on the soliton is of the same order of magnitude as the off-resonance impedances, although Fig. 21(d) does show that there is some small localization on the soliton despite the small magnitude. To obtain a more measurable impedance, we instead construct an atomically smooth soliton with a texture in the grounding components L_0 and C_0 between phases $N_{\mathrm{D}}^{\mathrm{NS}} = 4$ and $N_{\mathrm{D}}^{\mathrm{NS}} = 2$. The texture is described by

$$\begin{aligned} L_{0,l} &= \left[\omega^2\left(2C_1 - \mu_{\max}\tanh\left(\frac{l-N-1/2}{\zeta}\right)\right)\right]^{-1}, \\ C_{0,l} &= \frac{1}{\omega^2 L_{0,l}} = 2C_1 - \mu_{\max}\tanh\left(\frac{l-N-1/2}{\zeta}\right), \end{aligned}$$

where l is the index of a given node in the electron chain and $\mu_{\max}$ is the value of the onsite energy, Eq. (57), at infinity. We plot the impedance in the presence of a smooth soliton with width $\zeta = N/4$ as a function of frequency in Fig. 21(e). This shows a much more distinct peak when compared to the atomically sharp soliton in Fig. 21(c), and the impedance as a function of output node shows the corresponding peak at the center of the chain. Finally, we plot the impedance for a system with a soliton in the superconducting phase, Fig. 19(b), between phases $N_{\mathrm{D}}^{\mathrm{NS}} = 3$ and $N_{\mathrm{D}}^{\mathrm{NS}} = 1$ as a function of frequency in Fig. 21(g) and as a function of output node in Fig. 21(h). Large peaks in the impedance are found localized at both ends of the chain in addition to localization on the soliton at the center of the chain. This is due to both $N_{\mathrm{D}}^{\mathrm{NS}} = 3$ and $N_{\mathrm{D}}^{\mathrm{NS}} = 1$ hosting MZM.

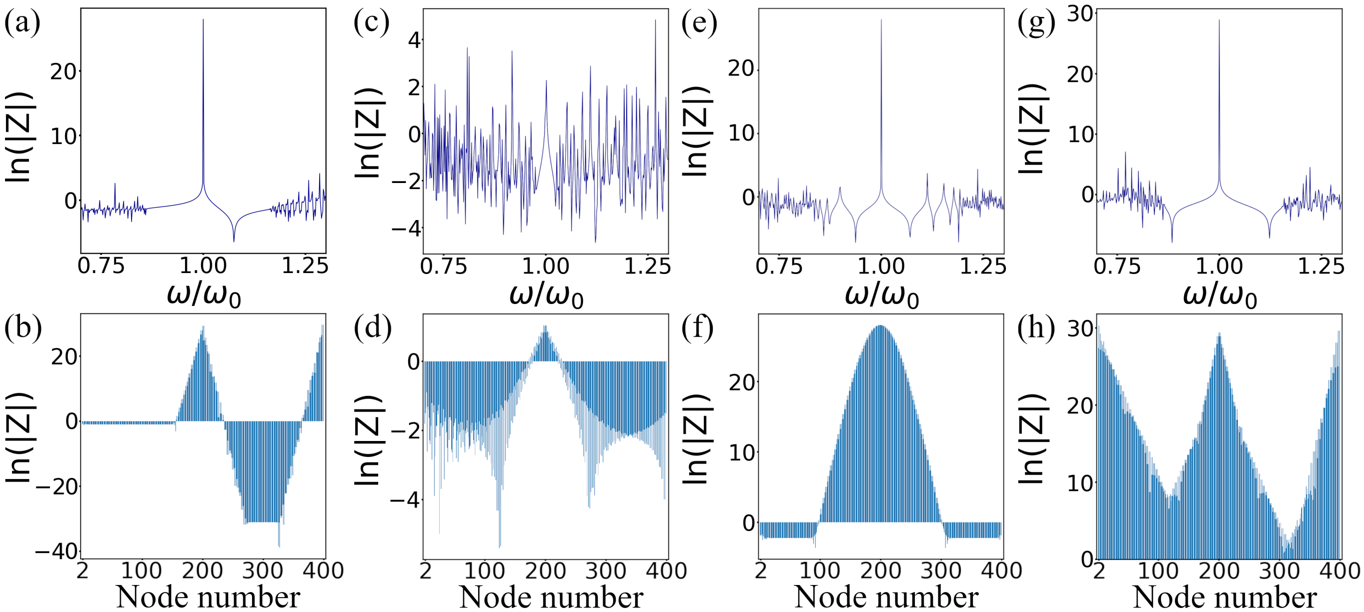

FIG. 21. Impedances across the topolectric realization of the $\mathbb{Z}_4$ chain, Fig. 19, for 400 nodes and input current at the first node in the electron channel. The top row of figures measure the impedance as a function of frequency, with current inputted at the first node in the chain and outputted at the center of the chain, while the bottom row measures impedance as a function of variable output node. Figures (a)-(d) are for a system with an atomically sharp soliton in the grounding inductors and capacitors, where (a) and (b) are for a system with a soliton between phases $N_{\mathrm{D}}^{\mathrm{NS}}=4$ and $N_{\mathrm{D}}^{\mathrm{NS}}=3$, while (c) and (d) are for a soliton between phases $N_{\mathrm{D}}^{\mathrm{NS}}=4$ and $N_{\mathrm{D}}^{\mathrm{NS}}=2$. Figures (e) and (f) are for an atomically smooth soliton in the grounding inductors and capacitors between phases $N_{\mathrm{D}}^{\mathrm{NS}}=4$ and $N_{\mathrm{D}}^{\mathrm{NS}}=2$. Finally, (g) and (h) are for an atomically sharp soliton in the phase-control unit between phases $N_{\mathrm{D}}^{\mathrm{NS}}=3$ and $N_{\mathrm{D}}^{\mathrm{NS}}=1$. Parameter values for (a) and (b) are $L_0=0.075$H, $C_0=1.6$F, $L_0'=0.171$, $C_0'=0.7$ $L_1=0.4$H, $C_1=0.3$F, $L_P=0.6$H, $C_P=0.2$F, $R_P=5\Omega$, for (c) and (d) $L_0=0.047$H, $C_0=1.7$F, $L_0'=0.053$H, $C_0'=1.5$F, $L_1=0.1$H, $C_1=0.8$F, $L_P=0.3$H, $C_P=0.267$F, $R_P=0.2\Omega$, for (e) and (f) $L_1=0.1$H, $C_1=0.8$F, $L_P=0.3$H, $C_P=0.267$F, $R_P=0.2\Omega$ and $\mu_{\max}=1$, and for (g) and (h) $L_0=0.4$H, $C_0=0.2$F, $L_1=0.1$H, $C_1=0.8$F, $L_P=0.3$H, $C_P=0.267$F, $R_P=1\Omega$. For fixed resistance and at the resonant frequency, all other parameter values can be identically scaled such that the two-point impedance as shown here is scaled by the same factor.

IX. ADDITIONAL NONSYMMORPHIC UNITARY SYMMETRIES

It has been predicted by K-theory [28] that there exist additional nonsymmorphic unitary symmetries which introduce new non-trivial topologies to the system, Table III. These unitary symmetries act on the k-space Hamiltonian as $U^\dagger H(k)U=H(k)$ and, in position space, as $\mathcal{U}^\dagger\mathcal{H}\mathcal{U}=\mathcal{H}$. They may exist simultaneously with symmorphic time-reversal and chiral symmetries allowing for the construction of nonsymmorphic models in the BDI and DIII classes. For the nonsymmorphic D class we denote the unitary symmetry as U. Both BDI and DIII nonsymmorphic classes are divided into subclasses based on whether the unitary symmetry commutes or anticommutes with the symmorphic chiral symmetry, with operators denoted U_- and U_+, respectively. It is also possible to have a nonsymmorphic unitary symmetry in the AII and C classes, although this does not affect the trivial topology of the symmorphic models. An exception to this is the CII class. It has a symmorphic winding number that is destroyed by a U_- symmetry, as discussed in the supplementary material [82].

The predicted topologies for each class are given in Table III, however, we note that, although we can calculate the corresponding index, we do not consider these models as topologically distinct from models without an additional unitary symmetry. This is clear as the nonsymmorphic unitary symmetry is represented by a translation in position space, and, as such, acts simply as a redefinition of the unit cell into two two-band models described by Ref. [61]. To see this, we examine an example model in the BDI class with $U_T=I$, $U_C=\tau_x\sigma_0$, and a unitary symmetry whose operator U_- commutes with the chiral operator $U_S=\tau_x\sigma_0$, resulting in a predicted $\mathbb{Z}\oplus\mathbb{Z}_2$ index. The Bloch Hamiltonian for this system is

$$\begin{aligned}
H(k) &= \begin{pmatrix} \hat{h}(k) & \hat{\Delta}(k) \\ \hat{\Delta}^\dagger(k) & -\hat{h}^T(-k)\end{pmatrix}, \qquad (65)\\
\hat{h}(k) &= \begin{pmatrix} -\mu & v+ve^{-ika} \\ v+ve^{ika} & -mu\end{pmatrix},\\
\hat{\Delta}(k) &= \begin{pmatrix} 0 & \Delta_s-\Delta_s e^{-ika} \\ -\Delta_s+\Delta_s e^{ika} & 0\end{pmatrix},
\end{aligned}$$

where, from Hamiltonian (3), we have set $\Delta_s'=\Delta_s$ and $w=v$. A schematic of this system is shown in Fig. 22(a).

TABLE III. Altland-Zirnbauer classification of one dimensional BdG Hamiltonians with built-in charge conjugation symmetry and the Kramer's degenerate AII class in the presence of additional nonsymmorphic unitary symmetries. T^2, C^2, and S^2 represent the values of time reversal, charge conjugation, and chiral symmetry, respectively. Column U^2 represents the presence of an additional unitary symmetry, columns U_-^2 (U_+^2) represents the presence of an additional unitary symmetry whose operator commutes (anticommutes) with the chiral symmetry operator of either the BDI or DIII class, where the label 'NS' represents a nonsymmorphic symmetry. The column 'index' lists the form of topological superconductor or insulator for each model.

Class	T^2	C^2	S^2	U^2	U_-^2	U_+^2	Index
D	0	1	0	NS	0	0	$\mathbb{Z}_2 \oplus \mathbb{Z}_2$
BDI	1	1	1	0	NS	0	$\mathbb{Z} \oplus \mathbb{Z}_2$
BDI	1	1	1	0	0	NS	$\mathbb{Z}_2$
DIII	-1	1	1	0	NS	0	$\mathbb{Z}_2$
DIII	-1	1	1	0	0	NS	$\mathbb{Z}_2$
AII	-1	0	0	NS	0	0	0

We have also written this in the Type I representation such that we can easily define a winding number. In this representation, the unitary symmetry is k dependent with $U_- = U_k(k,s)(\tau_0\sigma_x)$, and transforms between representations as $U_-(k,s) = U_k^\dagger(k,s)U_-(k,0)U_k(k,s)$. The winding number contributes the $\mathbb{Z}$ portion of the topology, and can be calculated by first defining a Q-matrix, Eq. (23), through the unitary transformation $Q(k) = U_{xI}^\dagger H(k) U_{xI}$, Eq. (V). For this system, this is described by component

$$q(k) = \begin{pmatrix} \mu & -v - ve^{ika} + \Delta_s - \Delta_s e^{ika} \\ -v - ve^{-ika} - \Delta_s + \Delta_s e^{-ika} & \mu \end{pmatrix},$$

where the product of the eigenvalues of $q(k)$ is

$$\begin{aligned} E_q(k) \;&=\; 2\Delta_s^2 + \mu^2 - 2v^2 - 2(\Delta_s^2 + v^2)\cos(ka) \\ &\quad -4i\Delta_s v \sin(k)\,. \end{aligned} \tag{66}$$

Plotting the path of $E_q(k)$ between $-\pi/a < k \leq \pi/a$ defines the winding number as the number of times the path encircles the origin, producing phases

$$N_{\mathrm{BDI}}^{\mathrm{NS}} = \begin{cases} -1 & \text{if } |E| > |2v| \text{ and } v < 0\,, \\ 0 & \text{if } |E| < |2v|\,, \\ 1 & \text{if } |E| > |2v| \text{ and } v > 0\,. \end{cases} \tag{67}$$

An example path of $E_q(k)$ is given in Fig. 22(b). To calculate the $\mathbb{Z}_2$ contribution to the topological index, we must first block diagonalize Hamiltonian (65) through the unitary transformation $H_{\mathrm{B}}(k) = U_{Ix}(k)^\dagger H(k) U_{Ix}(k)$, where

$$U_{Ix} = \frac{1}{\sqrt{2}} \begin{pmatrix} 0 & e^{ika/2} & 0 & -e^{ika/2} \\ 0 & 1 & 0 & 1 \\ e^{ika/2} & 0 & -e^{ika/2} & 0 \\ 1 & 0 & 1 & 0 \end{pmatrix} \tag{68}$$

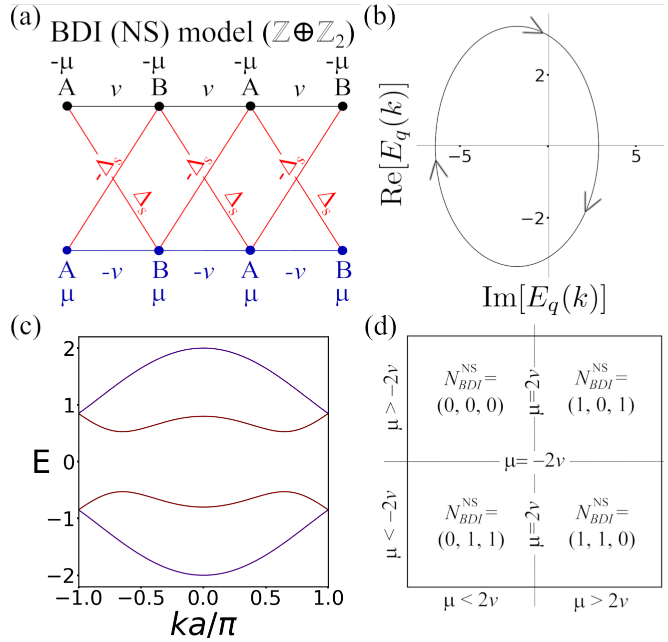

FIG. 22. Nonsymmorphic BDI class with symmorphic time-reversal, charge conjugation, and chiral symmetries and an additional nonsymmorphic unitary symmetry. (a) Schematic of an example model with constant chemical potential $\pm\mu$, hopping $\pm v$ and superconducting pairing Δ_s, this is the Kitaev chain in a two-band representation shown with intracell spacing $s = a/2$. (b) Example path of the winding number with the corresponding band structure of the four-band representation, Eq. (69), shown in (c), with eigenvalues of the block $H_1(k)$ in red and $H_2(k)$ in purple. (d) Phase diagram for $N_{\mathrm{BDI}}^{\mathrm{NS}} = (\nu_1, \nu_2, W)$, with $\nu_1 + \nu_2 = W$ (mod 2). Figures (b) and (c) use parameter values $\mu = 0.6$, $v = 0.7$, and $\Delta_s = 0.3$.

such that

$$H_{\mathrm{B}}(k) \;=\; \begin{pmatrix} H_1(k) & 0 \\ 0 & H_2(k) \end{pmatrix}, \tag{69}$$
$$H_1(k) \;=\; \begin{pmatrix} \mu - 2v\cos(ka/2) & -2i\Delta_s \sin(ka/2) \\ 2i\Delta_s \sin(ka/2) & -\mu + 2v\cos(ka/2) \end{pmatrix},$$
$$H_2(k) \;=\; \begin{pmatrix} \mu + 2v\cos(ka/2) & 2i\Delta_s \sin(ka/2) \\ -2i\Delta_s \sin(ka/2) & -\mu - 2v\cos(ka/2) \end{pmatrix}.$$

Eigenvalues for $H_1(k)$ are

$$\begin{aligned} E_1^2(k) \;&=\; 4\Delta_s^2 \sin^2(ka/2) - 4v^2 \sin^2(ka/2) \\ &\quad -4\mu v \cos(ka/2) + \mu^2 + 4v^2\,, \end{aligned} \tag{70}$$

and, for $H_2(k)$, $E_2(k) = E_1(k + \pi/a)$. An example of the combined band structure is given in Fig. 22(c). Kramer's degeneracy is present at $k = \pi/a$ as the nonsymmorphic unitary symmetry also enforces nonsymmorphic time-reversal, charge conjugation and chiral symmetries in addition to the symmorphic counterparts. Due to the 4π periodicity of the diagonal Hamiltonian components, we can not define a topological index for either 2×2 block. By setting $k = 0$, we find that $H_1(0)$ and $H_2(0)$ are zero-dimensional Hamiltonians with charge conjugation symmetry $U_C = \sigma_x$. Both $H_1(0)$ and $H_2(0)$ are diagonalized such that their transitions may be immediately calculated from their eigenvalues, although we can also find the transitions by calculating the Majorana number of each. We transform $H_1(k)$ to the Majorana basis by $H_{1,\mathcal{M}} = -iU_{\mathcal{M}} H_1 U_{\mathcal{M}}^\dagger$, where

$$U_{\mathcal{M}} = \frac{1}{\sqrt{2}} \begin{pmatrix} 1 & 1 \\ i & -i \end{pmatrix},$$

such that

$$H_{1,\mathcal{M}} = \begin{pmatrix} 0 & 2v - E \\ -2v + E & 0 \end{pmatrix}, \tag{71}$$

from which we define the Majorana number as $\nu_1 = \text{sign}(\text{Pf}[H_{1,\mathcal{M}}])$, resulting in $\nu_1 = 0$ if $E < 2v$ and $\nu_1 = 1$ if $E > 2v$. Following the same procedure for $H_2(0)$, we obtain

$$H_{2,\mathcal{M}} = \begin{pmatrix} 0 & 2v + E \\ -2v - E & 0 \end{pmatrix}, \tag{72}$$

with Majorana number $\nu_2 = \text{sign}(\text{Pf}[H_{2,\mathcal{M}}])$. We find $\nu_2 = 0$ if $E > -2v$ and $\nu_2 = 1$ if $E < -2v$. The topological invariants satisfy the constraint $\nu_1 + \nu_2 = N_{\text{BDI}}^{\text{NS}}$ (mod 2) thus defining a a $\mathbb{Z} \oplus \mathbb{Z}_2$ index [28]. This can be understood as each of the 2×2 sub-blocks of the Hamiltonian at $k = 0$ corresponding to the transitions of the winding number, as the path of $E_q(k)$ only passes through the origin at $k = 0$. Therefore, for this minimal model, there are four phases of the index which can be written as $N_{\text{BDI}}^{\text{NS}} = (\nu_1, \nu_2, N_{\text{BDI}}^{\text{NS}})$, and a full phase diagram is given in Fig. 22(d).

We emphasize that, although we can calculate the $\mathbb{Z} \oplus \mathbb{Z}_2$ index, we do not consider the addition of nonsymmorphic unitary symmetries as topologically distinct from models with only time-reversal, charge conjugation, and chiral symmetries. Once block diagonalized, the Brillouin zone must be redefined as $k \to 2\tilde{k}$. In this way, each of the blocks $H_1(\tilde{k})$ and $H_2(\tilde{k})$ are simply two-band symmorphic models in the BDI class, with winding numbers that match that of the overall Hamiltonian defined by the path of Eq. (66), up to the sign of v. This is the result of the nonsymmorphic unitary symmetry acting simply as a redefinition of the unit cell. It is clear to see from the schematic in Fig. 22(a) that the model is actually a two-band Kitaev chain, and that extending the unit cell introduces redundant degrees of freedom that can be removed via unitary transformation. As all systems in this class are related by unitary transformation to Eq. (65) [61], this holds for all possible variations of the symmetry operators. Therefore, the $\mathbb{Z} \oplus \mathbb{Z}_2$ topology is not realizable in one-dimension, nor are any of the other topologies given in Table III. The exception to this is class DIII, which has topology that is not affected by the additional nonsymmorphic symmetries.

X. CONCLUSIONS

We describe superconducting one-dimensional BdG tight-binding models on a periodic lattice with four energy bands, in addition to a noninteracting four-band model belonging to the class AII. For each superconducting symmetry class, we calculated the corresponding topological index for an example system, finding agreement with the tenfold way classification of symmorphic models [11, 21–27] and the classification of Ref. [28] for nonsymmorphic models. With this we complete the catalog of one-dimensional symmorphic and nonsymmorphic tight-binding models started in Ref [61] for two-band models, where certain topologies could not be explored due to TRS inducing Kramer's degeneracy.

While the topology of other symmetry classes can be described as either topologically trivial, an integer $\mathbb{Z}$ winding number, or a $\mathbb{Z}_2$ index, we describe a $\mathbb{Z}_4$ index belonging to the nonsymmorphic D class, a topology which is unique in one-dimensional non-interacting models. We calculate the topology based on a nonsymmorphic winding number equivalent, that has previously only been used to calculate a $\mathbb{Z}_2$ topological index without Kramer's degeneracy [44, 45]. We explore the $\mathbb{Z}_4$ model in detail, introducing solitons into the system and, by plotting the disorder-averaged DOS, we find that, in general, the zero-energy states hosted by the solitons are not robust to disorder, although, for only nearest-neighbor parameters, additional symmorphic symmetries may be present exactly at the domain wall and protect the solitons. We also show an example model in the AII class with a $\mathbb{Z}_2$ index that, although not superconducting, has a similar topological calculation to the $\mathbb{Z}_4$ model due to the nonsymmorphic chiral symmetry.

The translational symmetry of the models allows for block-diagonalization of finite position space Hamiltonians. Each of these blocks belong to a statistical ensemble [67, 68], with the number of blocks in each ensemble determined by the symmetries of the model. We catalog this distribution of blocks for each possible combination of symmorphic and nonsymmorphic symmetries.

We briefly describe the topology described by the presence of additional unitary symmetries. However, due to the spatial constraints of the model, we find that this simply acts as a redefinition of the unit cell, and hence has no physical implications in one-dimension.

A theoretical realization of nonsymmorphic topology is shown in the form of topolectric circuits, where electrical components are used to mimic the position space Hamiltonian, and the impedance through the circuit is used to identify domain walls between degenerate ground states [74, 76, 77]. We build circuits for symmorphic SSH and Kitaev chains and compare them to nonsymmorphic CDW and $\mathbb{Z}_4$ chains, finding agreement with the topological k-space calculations.

The models presented here in the atomic basis in position space provide a guideline for experimental realization of each symmetry class with four energy bands. Although the topology of the superconducting models may be realized by identical four-band noninteracting tight binding parameters, it may be more experimentally viable to consider a two-band topological insulator, with superconductivity induced by the proximity effect [92–94] to replicate the topology.

---

[1] A. Y. Kitaev, Unpaired Majorana fermions in quantum wires, Phys.-Usp. **44**, 131 (2001).

[2] A. Y. Kitaev, Fault-tolerant quantum computation by anyons, Ann. Phys. (N. Y), **303**, 2 (2003).

[3] C. Nayak, S. H. Simon, A. Stern, M. Freedman, and S. Das. Sarma, Non-Abelian anyonsand topological quantum computation, Rev. Mod. Phys. **80**, 1083 (2008).

[4] A. Stern, and N. H. Lindner, Topological quantum computation—from basic concepts to first experiments, Sci. **339**, 1179 (2013).

[5] V. Lahtinen, and J. K. Pachos, A short introduction to topological quantum computation, SciPost Phys. **3**, (2017).

[6] C. W. J. Beenakker, Random-matrix theory of Majorana fermions and topological superconductors, Rev. Mod. Phys. **87**, 1037 (2015).

[7] H.-M. Guo, A brief review on one-dimensional topological insulators and superconductors, Sci. China Phys. Mech. **59**, 637401 (2016).

[8] M. Sato and Y. Ando, Topological superconductors: a review, Rep. Prog. Phys. **80**, 076501 (2017).

[9] M. M. Sharma, P. Sharma, N. K. Karn, and V. P. S. Awana, Comprehensive review on topological superconducting materials and interfaces, Supercond. Sci. Technol. **35**, 083003 (2022)

[10] T. Dvir, G. Wang, N. van Loo, et al., Realization of a minimal Kitaev chain in coupled quantum dots, Nature **614**, 445 (2023).

[11] C. Chiu, J. C. Y. Teo, A. P. Schnyder, and S. Ryu, Classification of topological quantum matter with symmetries Rev. Mod. Phys. **88**, 035005 (2016).

[12] S. Das Sarma, M. Freedman, and C. Nayak, Topological quantum computation, Phys. Today **59** (7), 32 (2006).

[13] K. Laubscher, J. D. Sau, and S. D. Sarma, Majorana zero modes in gate-defined germanium hole nanowires, Phys. Rev. B **109**, 035433 (2024)

[14] V. Mourik, K. Zuo, S. M. Frolov, S. R. Plissard, E. P. A. M. Bakkers, and L. P. Kouwenhoven, Signatures of Majorana fermions in hybrid superconductor-semiconductor nanowire devices, Sci. **336**, 1003 (2012).

[15] A. Das, Y. Ronen, Y. Most, Y. Oreg, M. Heiblum, and H. Shtrikman, Zero-bias peaks and splitting in an Al–InAs nanowire topological superconductor as a signature of Majorana fermions, Nat. Phys. **8**, 887 (2012).

[16] M. T. Deng, S. Vaitiekėnas, E. B. Hansen, J. Danon, M. Leijnse, K. Flensberg, J. Nygård, P. Krogstrup, and C. M. Marcus, Majorana bound state in a coupled quantum-dot hybrid-nanowire system, Sci. **354**, 1557 (2016).

[17] S. Nadj-Perge, I. K. Drozdov, J. Li, H. Chen, S. Jeon, J. Seo, A. H. MacDonald, B. A. Bernevig, and A. Yazdani, Observation of Majorana fermions in ferromagnetic atomic chains on a superconductor, Sci. **346**, 602 (2014).

[18] M. Ruby, F. Pientka, Y. Peng, F. v. Oppen, B. W. Heinrich, and K. J. Franke, End States and Subgap Structure in Proximity-Coupled Chains of Magnetic Adatoms, Phys. Rev. Lett. **115**, 197204 (2015).

[19] R. Awlak, M. Kisiel, J. Klinovaja, T. Meier, S. Kawai, T. Glatzel, D. Loss, and E. Meyer, Probing atomic structure and Majorana wavefunctions in mono-atomic Fe chains on superconducting Pb surface, npj Quant. Inf. **2**, 16035 (2016).

[20] B. Jäck, Y. Xie, and A. Yazdani, Detecting and distinguishing Majorana zero modes with the scanning tunnelling microscope. Nat. Rev. Phys. **3**, 541 (2021).

[21] A. Altland and M. R. Zirnbauer, Nonstandard symmetry classes in mesoscopic normal-superconducting hybrid structures, Phys. Rev. B **55**, 1142 (1997).

[22] A. P. Schnyder, S. Ryu, A. Furusaki, and A. W. W. Ludwig, Classification of topological insulators and superconductors in three spatial dimensions, Phys. Rev. B **78**, 195125 (2008)

[23] A. Kitaev, Periodic table for topological insulators and superconductors, AIP Conf. Proc. **1134**, 22 (2009).

[24] X. L. Qi, Taylor, L. Hughes, and S. C. Zhang, Topological invariants for the Fermi surface of a time-reversal-invariant superconductor, Phys. Rev. B **81**, 134508 (2010).

[25] S. Ryu, A. P. Schnyder, A. Furusaki, and A. W. W. Ludwig, Topological insulators and superconductors: tenfold way and dimensional hierarchy, New J. Phys. **12**, 065010 (2010).

[26] J. C. Y. Teo and C. L. Kane, Topological defects and gapless modes in insulators and superconductors, Phys. Rev. B **82**, 115120 (2010).

[27] P. Matveeva, T. Hewitt, D. Liu, K. Reddy, D. Gutman, and Sam T. Carr, One-dimensional noninteracting topological insulators with chiral symmetry Phys. Rev. B **107**, 075422 (2023).

[28] K. Shiozaki, M. Sato, and K. Gomi, Topology of nonsymmorphic crystalline insulators and superconductors, Phys. Rev. B **93**, 195413 (2016).

[29] J. C. Y. Teo, L. Fu, and C. L. Kane, Surface states and topological invariants in three-dimensional topological insulators: Application to $Bi_{1-x}Sb_x$, Phys. Rev. B **78**, 045426 (2008).

[30] L. Fu, Topological Crystalline Insulators Phys. Rev. Lett. **106**, 106802 (2011).

[31] T. H. Hsieh, H. Lin, J. Liu, W. Duan, A. Bansil, and L. Fu, Topological crystalline insulators in the SnTe material class Nat. Commun. **3**, 982 (2012).

[32] C.-X. Liu, R.-X. Zhang, and B. K. VanLeeuwen, Topological nonsymmorphic crystalline insulators, Phys. Rev. B **90**, 085304 (2014).

[33] K. Shiozaki and M. Sato, Topology of crystalline insulators and superconductors, Phys. Rev. B **90**, 165114 (2014).

[34] S. M. Young and C. L. Kane, Dirac semimetals in two dimensions, Phys. Rev. Lett. **115**, 126803 (2015).

[35] Z. Wang, A. Alexandradinata, R. J. Cava, and B. A. Bernevig, Hourglass fermions, Nature **532**, 189 (2016).

[36] D. Varjas, F. de Juan, and Y.-M. Lu, Space group constraints on weak indices in topological insulators, Phys.

Rev. B **96**, 035115 (2017).

[37] J. Kruthoff, J. de Boer, J. van Wezel, C. L. Kane, and R.-J. Slager, Topological classification of crystalline insulators through band structure combinatorics, Phys. Rev. X **7**, 041069 (2017).

[38] M. A. J. Herrera and D. Bercioux, Tunable Dirac points in a two-dimensional nonsymmorphic wallpaper group lattice, Commun. Phys. **6**, 42 (2023).

[39] J. Cayssol and J.-N. Fuchs, Topological and geometrical aspects of band theory, J. Phys. Mater. **4**, 034007 (2021).

[40] W. P. Su, J. R. Schrieffer, and A. J. Heeger, Solitons in Polyacetylene, Phys. Rev. Lett. **42**, 1698 (1979).

[41] W. P. Su, J. R. Schrieffer, and A. J. Heeger, Soliton excitations in polyacetylene, Phys. Rev. B 2**2**, 2099 (1980).

[42] M. Z. Hasan and C. L. Kane, Colloquium: Topological insulators, Rev. Mod. Phys. **82**, 3045 (2010).

[43] J. K. Asbóth, L. Oroszlány, and A. Pályi, A Short Course on Topological Insulators (Springer, Cham, 2016).

[44] K. Shiozaki, M. Sato, and K. Gomi, $\mathbb{Z}_2$ topology in nonsymmorphic crystalline insulators: Möbius twist in surface states, Phys. Rev. B **91**, 155120 (2015).

[45] W. Brzezicki and T. Hyart, Topological domain wall states in a nonsymmorphic chiral chain, Phys. Rev. B **101**, 235113 (2020).

[46] R. E. J. Allen, H. V. Gibbons, A. M. Sherlock, H. R. M. Stanfield, and E. McCann, Nonsymmorphic chiral symmetry and solitons in the Rice-Mele model, Phys. Rev. B **106**, 165409 (2022).

[47] S. Kivelson, Solitons with adjustable charge in a commensurate Peierls insulator, Phys. Rev. B **28**, 2653 (1983).

[48] J.-N. Fuchs and F. Piéchon, Orbital embedding and topology of one-dimensional two-band insulators, Phys. Rev. B **104**, 235428 (2021).

[49] M. J. Rice and E. J. Mele, Elementary Excitations of a Linearly Conjugated Diatomic Polymer, Phys. Rev. Lett. **49**, 1455 (1982).

[50] R. S. K. Mong, A. M. Essin, and J. E. Moore, Antiferromagnetic topological insulators, Phys. Rev. B **81**, 245209 (2010).

[51] C. Fang and L. Fu, New classes of three-dimensional topological crystalline insulators: Nonsymmorphic and magnetic, Phys. Rev. B **91**, 161105(R) (2015).

[52] Y. X. Zhao and A. P. Schnyder, Nonsymmorphic symmetry-required band crossings in topological semimetals, Phys. Rev. B **94**, 195109 (2016).

[53] Y. Yanase and K. Shiozaki, Möbius topological superconductivity in UPt_3, Phys. Rev. B **95**, 224514 (2017).

[54] J. Arkinstall, M. H. Teimourpour, L. Feng, R. El-Ganainy, and H. Schomerus, Topological tight-binding models from nontrivial square roots, Phys. Rev. B **95**, 165109 (2017).

[55] M. M. Otrokov *et al.*, Prediction and observation of an antiferromagnetic topological insulator, Nature **576**, 416 (2019).

[56] Y. Gong *et al.*, Experimental realization of an intrinsic magnetic topological insulator, Chin. Phys. Lett. **36**, 076801 (2019).

[57] D. Zhang, M. Shi, T. Zhu, D. Xing, H. Zhang, and J. Wang, Topological axion states in the magnetic insulator $MnBi_2Te_4$ with the quantized magnetoelectric effect, Phys. Rev. Lett. **122**, 206401 (2019).

[58] C. Niu, H. Wang, N. Mao, B. Huang, Y. Mokrousov, and Y. Dai, Antiferromagnetic topological insulator with nonsymmorphic protection in two dimensions, Phys. Rev. Lett. **124**, 066401 (2020).

[59] A. M. Marques and R. G. Dias, One-dimensional topological insulators with noncentered inversion symmetry axis, Phys. Rev. B **100**, 041104(R) (2019).

[60] Y. Yang, H. C. Po, V. Liu, J. D. Joannopoulos, L. Fu, and M. Soljačić, Non-Abelian nonsymmorphic chiral symmetries, Phys. Rev. B **106**, L161108 (2022).

[61] E. McCann, Catalog of noninteracting tight-binding models with two energy bands in one dimension, Phys. Rev. B **107**, 245401 (2023).

[62] Y. Tanaka, M. Sato, and N. Nagaosa, Symmetry and Topology in Superconductors - Odd-Frequency Pairing and Edge States -, J. Phys. Soc. Jpn. **81**, 011013 (2012).

[63] J. Alicea, New directions in the pursuit of Majorana fermions in solid state systems, Rep. Prog. Phys. **75**, 076501 (2012).

[64] M. Leijnse and K. Flensberg, Introduction to topological superconductivity and Majorana fermions, Semicond. Sci. Technol. **27**, 124003 (2012).

[65] F. J. Dyson, Statistical Theory of the Energy Levels of Complex Systems. I, J. Math. Phys. **3**, 140 (1962).

[66] E. P. Wigner, Random matrices in physics, SIAM Rev. **9**, 1 (1967).

[67] M. L. Mehta, Random Matrix Theory (Springer, New York, 1990).

[68] T. Guhr, A. Müller-Groeling, and H. A. Weidenmüller, Random-matrix theories in quantum physics: Common con- cepts, Phys. Rep. **299**, 189 (1998).

[69] V. Oganesyan and D. A. Huse, Localization of interacting fermions at high temperature, Phys. Rev. B **75**, 155111 (2007).

[70] Y. Y. Atas, E. Bogomolny, O. Giraud, and G. Roux, Distribution of the ratio of consecutive level spacings in random matrix ensembles, Phys. Rev. Lett. **110**, 084101 (2013).

[71] M. Tymczyszyn and E. McCann, One-dimensional $\mathbb{Z}_4$ topological superconductor, Phys. Rev. B **110**, 085416 (2024)

[72] C. H. Lee, S. Imhof, C. Berger, F. Bayer, J. Brehm, L. W. Molenkamp, T. Kiessling, and R. Thomale, Topolectrical circuits, Commun. Phys. **1**, 39 (2018).

[73] S. Imhof, C. Berger, F. Bayer, J. Brehm, L. W. Molenkamp, T. Kiessling, F. Schindler, C. H. Lee, M. Greiter, T. Neupert, and R. Thomale, Topolectrical-circuit realization of topological corner modes, Nat. Phys. **14**, 925 (2018).

[74] M. Ezawa, Higher-order topological electric circuits and topological corner resonance on the breathing kagome and pyrochlore lattices, Phys. Rev. B **98**, 201402(R) (2018).

[75] T. Hofmann, T. Helbig, C. H. Lee, M. Greiter, and R. Thomale, Chiral Voltage Propagation and Calibration in a Topolectrical Chern Circuit, Phys. Rev. Lett. **122**, 247702 (2019).

[76] M. Ezawa, Braiding of Majorana-like corner states in electric circuits and its non-Hermitian generalization, Phys. Rev. B **100**, 045407 (2019).

[77] M. Ezawa, Non-Abelian braiding of Majorana-like edge states and topological quantum computations in electric circuits, Phys. Rev. B **102**, 075424 (2020).

[78] J. Dong, V. Juričić, and B. Roy, Topolectric circuits: Theory and construction, Phys. Rev. Research **3**, 023056 (2021).

[79] C. L. M. Wong and K. T. Law, Majorana Kramers dou-

blets in $d_{x^2} - d_{y^2}$-wave superconductors with Rashba spin-orbit coupling, Phys. Rev. B **86**, 184516 (2012).

[80] A. P. Schnyder and S. Ryu, Topological phases and surface flat bands in superconductors without inversion symmetry, Phys. Rev. B **84**, 060504(R) (2011).

[81] S. Gholizadeh, M. Yahyavi and B. Hetényi, Extended Creutz ladder with spin-orbit coupling: A one-dimensional analog of the Kane-Mele model, Europhys. Lett. **122**, 27001 (2018).

[82] See Supplemental Material at [URL will be inserted by publisher] for long-range parameters of the generalized superconducting Rice-mele model, example models of the symmorphic D, DIII, BDI, CII classes and nonsymmorphic CII class, and for the topological transition points of the $\mathbb{Z}_4$ model in the presence of A-A and B-B hopping and superconducting pairing.

[83] C. Bena and G. Montambaux, Remarks on the tight-binding model of graphene, New J. Phys. **11**, 095003 (2009).

[84] M. Cheng, Superconducting proximity effect on the edge of fractional topological insulators, Phys. Rev. B **86**, 195126 (2012).

[85] F. Zhang and C.L. Kane, Time-Reversal-Invariant Z_4 Fractional Josephson Effect, Phys. Rev. Lett. **113**, 036401 (2014).

[86] S. Cheon, T. Kim, S. Lee, H. W. Yeom, Chiral solitons in a coupled double Peierls chain, Sci. **350**, 182-185 (2015).

[87] R. Jackiw and C. Rebbi, Solitons with fermion number $\frac{1}{2}$, Phys. Rev. D **13**, 3398 (1976).

[88] J. H. Muten, L. H. Frankland, and E. McCann, Solitons in binary compounds with stacked two-dimensional honeycomb lattices, Phys. Rev. B **109**, 165416 (2024).

[89] S.-H. Han, S.-G. Jeong, S.-W. Kim, T.-H. Kim, and S. Cheon, Topological features of ground states and topological solitons in generalized Su-Schrieffer-Heeger models using generalized time-reversal, particle-hole, and chiral symmetries, Phys. Rev. B **102**, 235411 (2020).

[90] T. Koschny and L. Schweitzer, Influence of correlated disorder potentials on the levitation of current carrying states in the quantum Hall effect, Physica E **12**, 654 (2002).

[91] Z.-Z. Guo, Entanglement in one-dimensional Anderson model with long-range correlated disorder, Chin. Phys. Lett. **25**, 1079 (2008).

[92] S. De Franceschi, L. Kouwenhoven, C. Schönenberger and W. Wernsdorfer, Hybrid superconductor–quantum dot devices, Nat. Nanotechnol. **5**, 703 (2010).

[93] S. M. Albrecht, A. P. Higginbotham, M. Madsen, F. Kuemmeth, T. S. Jespersen, J. Nygård, P. Krogstrup and C. M. Marcus, Exponential protection of zero modes in Majorana islands, Nat. **531**, 206 (2016).

[94] A. Nikolaenko and F. Pientka, Topological superconductivity in proximity to type-II superconductors, Phys. Rev. B **103**, 134503 (2021).

Supplementary material: One-dimensional topological superconductors with nonsymmorphic symmetries

I. LONG-RANGE PARAMETERS

We generalize the superconducting Rice-Mele Hamiltonian (Eq. (3) in the main text) to include all possible long-range tight-binding couplings

$$h_1(k,s) = -\mu + u + \sum_{n=1}^{\infty} t_{2n}\cos(kan+\phi_{2n}), \tag{S1}$$

$$\begin{aligned} h_2(k,s) = & \sum_{n=1}^{\infty}[t_{2n-1}\cos[k((n-1)a+s)+\phi_{2n-1}] + it_{2n-1}\sin[k((n-1)a+s)+\phi_{2n-1}] \\ & + t'_{2n-1}\cos[k(an-s)+\phi'_{2n-1}] - it'_{2n-1}\sin[k(an-s)+\phi'_{2n-1}]], \end{aligned} \tag{S2}$$

$$h_3(k,s) = -\mu - u + \sum_{n=1}^{\infty} t'_{2n}\cos(kan+\phi'_{2n}), \tag{S3}$$

where, for integer n, t_{2n} and t'_{2n} are A-A and B-B hoppings with phases ϕ_{2n} and ϕ'_{2n}, t_{2n-1} and t'_{2n-1} are A-B hoppings with phases ϕ_{2n-1} and ϕ'_{2n-1}. Similarly, we extend the superconducting pairings as

$$\Delta_1(k,s) = \sum_{n=1}^{\infty}[2i\Delta_{2n,p}\cos(\phi_{2n,p})\sin(kan) - 2\Delta_{2n,p}\sin(\phi_{2n,p})\cos(kan)], \tag{S4}$$

$$\tag{S5}$$

$$\begin{aligned} \Delta_2(k,s) = & \sum_{n=1}^{\infty}[\Delta_{2n-1,s}\cos[k((n-1)a+s)+\phi_{2n-1,s}] + i\Delta_{2n-1,s}\sin[k((n-1)a+s)+\phi_{2n-1,s}] \\ & + \Delta'_{2n-1,s}\cos[k(an-s)-\phi'_{2n-1,s}] - i\Delta'_{2n-1,s}\sin[k(an-s)-\phi'_{2n-1,s}]], \end{aligned} \tag{S6}$$

$$\Delta_3(k,s) = \sum_{n=1}^{\infty}[2i\Delta'_{2n,p}\cos(\phi'_{2n,p})\sin(kan) - 2\Delta'_{2n,p}\sin(\phi'_{2n,p})\cos(kan)], \tag{S7}$$

where $\Delta_{2n,p}$ and $\Delta'_{2n,p}$ are A-A and B-B p-wave superconducting order parameters with phases $\phi_{2n,p}$ and $\phi'_{2n,p}$, and $\Delta_{2n-1,s}$ and $\Delta'_{2n-1,s}$ are A-B s-wave superconducting order parameters with phases $\phi_{2n-1,s}$ and $\phi'_{2n-1,s}$. In terms of the nearest-neighbor parameters in the main text $t_2 = t_{AA}$, $t'_2 = t_{BB}$, $\phi_2 = \phi_{AA}$, $\phi'_2 = \phi_{BB}$, $t_1 = v$, $t'_1 = w$, $\phi_1 = \phi_v$, $\phi'_1 = w$, $\Delta_{2,p} = \Delta_p$, $\Delta'_{2,p} = \Delta'_p$, $\phi_{2,p} = \phi_p$, $\phi'_{2,p} = \phi'_p$, $\Delta_{1,s} = \Delta_s$, $\Delta'_{1,s} = \Delta'_s$, $\Delta_{3,s} = \check{\Delta}_s$, $\phi_{1,s} = \phi_s$, $\phi'_{1,s} = \phi'_s$, $\phi_{3,s} = \check{\phi}_s$, with t_3 unchanged.

II. SYMMORPHIC MODELS

A. Symmorphic D class with $\mathbb{Z}_2$ index and $T^2 = 0$, $C^2 = 1$, $S^2 = 0$

While the topology of symmorphic topological superconductors is already understood [S1–S3], the principles used to calculate their respective topological indices lends significantly to similar calculations in the nonsymmorphic classes. For this reason we introduce the topology of the three symmorphic BdG classes D, BDI, and DIII, beginning with class D which possesses only charge conjugation symmetry. As the charge conjugation symmetry is fixed for all BdG Hamiltonians as $U_C = \tau_x\sigma_0$, and as there are no further symmetries constraining the system, the generalized Hamiltonian (Eq. (3) in the main text) remains completely unconstrained. For simplicity we consider a minimal version of this model, a Kitaev chain with a complex order parameter, where, from Hamiltonian (Eq. (3) in the main text), we set $\Delta'_s = \Delta_s$ and $w = v$. Additionally, we consider that the onsite energy alternates along atomic sites, and that only the intracell order parameter has a complex phase, as, if the intercell order parameter has the same phase, it could simply be gauged away inducing chiral symmetry.

A schematic for this system is given in Fig. S1(a). The k-space Bloch Hamiltonian for this example model is

$$H(k) = \begin{pmatrix} \hat{h}(k) & \hat{\Delta}(k) \\ \hat{\Delta}^\dagger(k) & -\hat{h}^T(-k) \end{pmatrix}, \tag{S8}$$

$$\hat{h}(k) = \begin{pmatrix} -\mu+u & v+ve^{-ika} \\ v+ve^{ika} & -\mu-u \end{pmatrix}, \tag{S9}$$

$$\hat{\Delta}(k) = \begin{pmatrix} 0 & \Delta_s e^{i\phi_s} - \Delta_s e^{-ika} \\ -\Delta_s e^{i\phi_s} + \Delta_s e^{ika} & 0 \end{pmatrix}. \tag{S10}$$

In general, the band structure for the first quantized Hamiltonian is an insulator, and a numerically obtained band structure is given in Fig. S2(a). From Hamiltonian (S8) we can define a $\mathbb{Z}_2$ topological index known as the Majorana number [S1, S4] as

$$N_{\mathrm{D}}^{\mathrm{S}} = \mathrm{sgn}(\mathrm{Pf}[H_M(0)]\mathrm{Pf}[H_M(\pi/a)]), \tag{S11}$$

where

$$H_M(k) = \frac{1}{2}\begin{pmatrix} -iH_{11}(k) & H_{12}(k) \\ H_{21}(k) & iH_{11}(k) \end{pmatrix}, \tag{S12}$$

$$H_{11}(k) = \hat{\Delta}(k) + \hat{\Delta}^\dagger(k), \tag{S13}$$

$$H_{12}(k) = -\hat{h}(k) - \hat{h}^T(k) + \hat{\Delta}(k) - \hat{\Delta}^\dagger(k), \tag{S14}$$

$$H_{21}(k) = \hat{h}(k) + \hat{h}^T(k) + \hat{\Delta}(k) - \hat{\Delta}^\dagger(k), \tag{S15}$$

is the Hamiltonian in the Majorana basis, as defined by the basis transformation

$$\Psi_k = \begin{pmatrix} c_{\alpha,k} \\ c_{\beta,k} \\ c^\dagger_{\alpha,-k} \\ c^\dagger_{\beta,-k} \end{pmatrix} \Rightarrow \begin{pmatrix} \hat{\lambda}_1 \\ \hat{\lambda}_2 \\ \hat{\lambda}_3 \\ \hat{\lambda}_4 \end{pmatrix} = \begin{pmatrix} c_{\alpha,k} + c^\dagger_{\alpha,-k} \\ c_{\beta,k} + c^\dagger_{\beta,-k} \\ i(c_{\alpha,k} - c^\dagger_{\alpha,-k}) \\ i(c_{\beta,k} - c^\dagger_{\beta,-k}) \end{pmatrix}, \tag{S16}$$

where $\hat{\lambda}_i$ are Majorana fermions. This transformation can be written as $\mathcal{H}_M(k) = -iU_M\mathcal{H}(k)U_M^\dagger$, where

$$U_M = \begin{pmatrix} 1 & 0 & 1 & 0 \\ i & 0 & -i & 0 \\ 0 & 1 & 0 & 1 \\ 0 & i & 0 & -i \end{pmatrix}. \tag{S17}$$

The Hamiltonian (S12) is skew-symmetric at points $k = 0$ and $k = \pi$, allowing for a well-defined Pfaffian, and resulting in a Majorana number

$$N_{\mathrm{D}}^{\mathrm{S}} = \mathrm{sgn}[(2\Delta_s^2 + \mu^2 - u^2 - 4v^2 - 2\Delta_s^2\cos(\phi_s)) \cdot (\mu - u^2 + 2\Delta_s^2 + 2\Delta_s^2\cos(\phi_s)] \tag{S18}$$

The physical significance of this is that, for a finite model in position space, there are MZM exponentially localized onto the edges of the chain for parameter regions in which $W = -1$. An example of this is shown for the BDI class in Fig. 5 of the main text.

B. Symmorphic BDI class with $\mathbb{Z}$ index and $T^2 = 1$, $C^2 = 1$, $S^2 = 1$

We write an example with minimal parameters with time-reversal operator $U_T = I$ and chiral operator $U_S = \tau_x\sigma_0$. This model can be obtained by setting the complex phase of the order parameter in the D class model to zero which induces TRS, Fig. S1(b). The Bloch Hamiltonian is now

$$H(k) = \begin{pmatrix} \hat{h}(k) & \hat{\Delta}(k) \\ \hat{\Delta}^\dagger(k) & -\hat{h}^T(-k) \end{pmatrix}, \tag{S19}$$

$$\hat{h}(k) = \begin{pmatrix} -\mu+u & v+ve^{-ika} \\ v+ve^{ika} & -\mu-u \end{pmatrix}, \tag{S20}$$

$$\hat{\Delta}(k) = \begin{pmatrix} 0 & \Delta_s - \Delta_s e^{-ika} \\ -\Delta_s + \Delta_s e^{ika} & 0 \end{pmatrix}, \tag{S21}$$

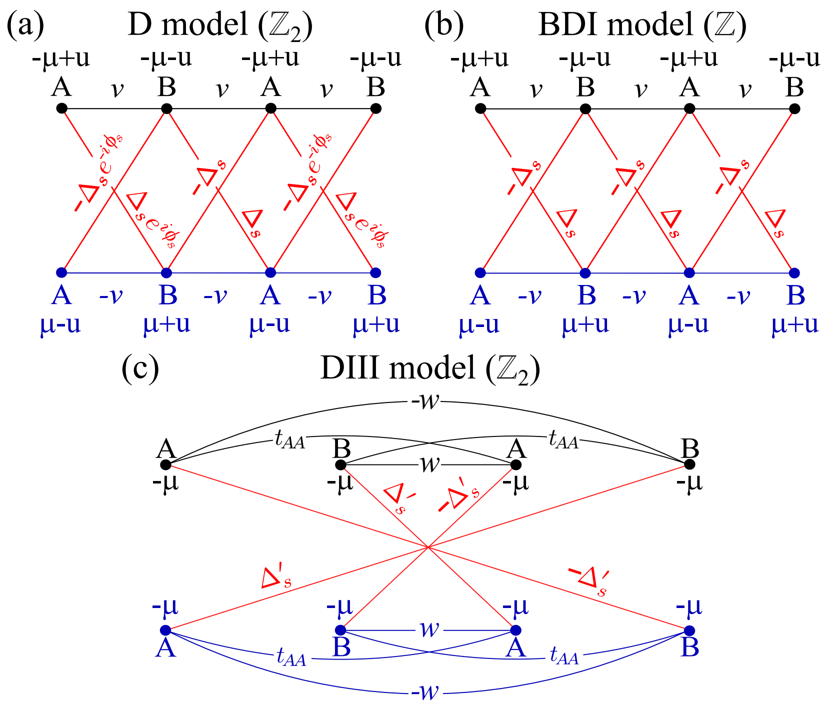

FIG. S1. Schematics of example symmorphic models in the BdG basis, shown with intracell spacing $s = a/2$. (a) Schematic for a system in the D class with constant chemical potential $\pm\mu$ and nearest-neighbor hopping $\pm v$, alternating onsite energy $\pm u$, and a nearest-neighbor s-wave order parameter of constant magnitude Δ_s that alternates between being real and complex with phase ϕ_s. (b) Shows the same system but with $\phi_s = 0$, transforming the model to the BDI class. (c) DIII model with constant chemical potential, intercell nearest-neighbor hopping $\pm w$ and third nearest-neighbor hopping of the same magnitude but opposite sign, next nearest neighbor hopping $\pm t_{AA}$, a nearest-neighbor real s-wave order parameter of constant magnitude Δ'_s, and a third nearest-neighbor order parameter of the same magnitude.

where, from the Rice-Mele Hamiltonian (Eq. (3) in the main text), we have set $w = v$ and $\Delta'_s = \Delta_s$. Note that setting the alternating onsite energy to zero results allows for the block diagonalization of the Hamiltonian into that of the two-band Kitaev chain, as discussed in Sec. IX in the main text. In general, the band structure for the first quantized Hamiltonian is an insulator, with energy eigenvalues

$$\begin{aligned} E^2 &= \mu^2+u^2+f(k)+S(k)\pm\sqrt{\mu^2 f(k)+u^2 S(k)+\mu^2 u^2}, \\ f(k) &= 2v^2(\cos(k)+1), \\ S(k) &= 2\Delta^2(1-\cos(k)). \end{aligned}$$

An example band structure is given in Fig. S2(b). The topology of this model is explored in the main text in Sec. V using a Q-matrix. It is also possible to calculate a Majorana number for this class, which determines the presence or absence of MZM. In this case we find that

$$M = \mathrm{sgn}((\mu^2 - u^2 - 4v^2)(\mu^2 - u^2 + 4\Delta_s^2)), \tag{S22}$$

which is in agreement with the winding number calculations from the main text.

C. Symmorphic DIII class with $\mathbb{Z}_2$ index and $T^2 = -1$, $C^2 = 1$, $S^2 = 1$

We write a minimal example model in which the time-reversal operator $U_T = \tau_0\sigma_y$ and the chiral operator $U_S = \tau_x\sigma_y$. This example includes a third-nearest neighbor hopping and order parameter to preserve the TRS. From the generalized Rice-mele Hamiltonian (Eq. (3) in the main text) we set $t_{BB} = t_{AA}$, $t_3 = -w$, and $\check{\Delta}_s = -\Delta'_s$, resulting

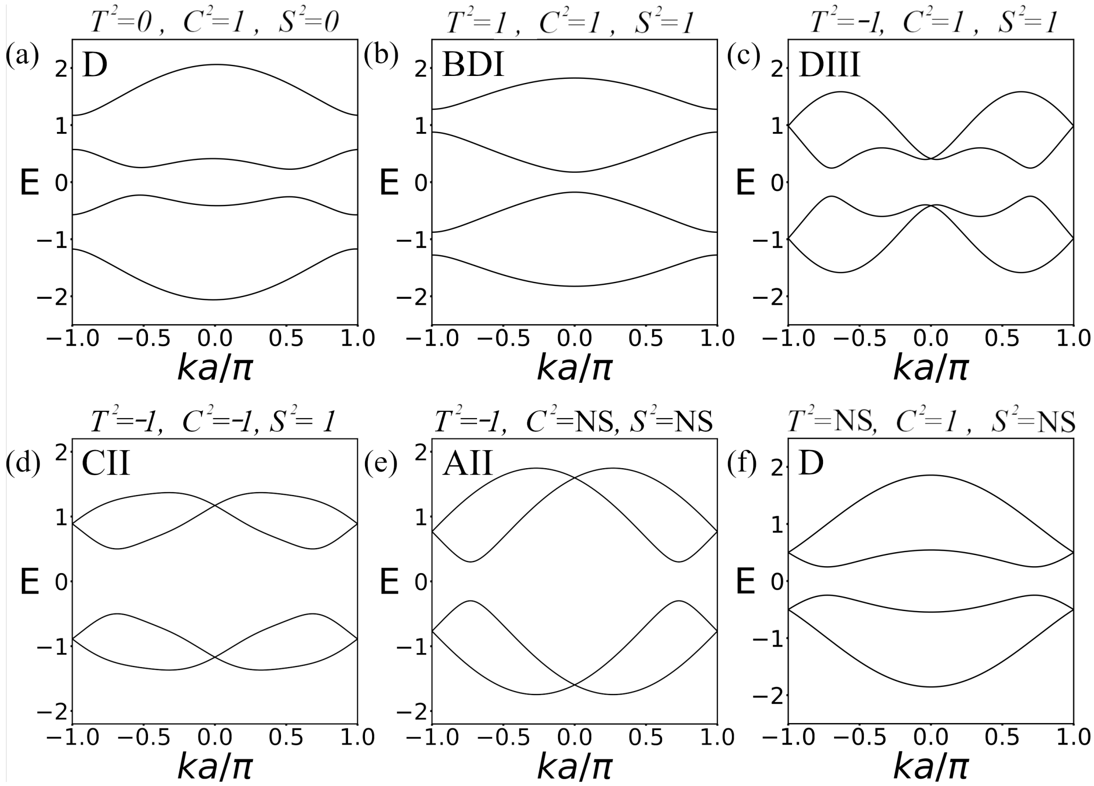

FIG. S2. Example Bulk band structures with charge conjugation symmetry and no additional unitary symmetry. (a) Symmorphic D class system described by Hamiltonian (S8) with parameter values $\mu = 0.8$, $u = 0.3$, $v = 0.6$, $\Delta_s = 0.2$, and $\phi_s = \pi/3$. (b) Symmorphic BDI class system described by Hamiltonian (S19) with parameter values $\mu = 1$, $u = 0.2$, $v = 0.4$, and $\Delta_s = 0.2$. (c) Symmorphic DIII class system described by Hamiltonian (S23), with parameter values $\mu = 0.5$, $w = 0.5$, $t_{AA} = 0.2$, and $\Delta'_s = 0.2$. (d) Symmorphic CII class system described by Hamiltonian (S34), with parameter values $\Gamma = 0.5$, $v = 0.7$, $w = 0.3$, $\phi_v = \phi_w = \pi/3$. (e) Nonsymmorphic AII class system described by Hamiltonian (28) in the main text, with parameter values $u = 0.3$, $\Gamma = 0.5$, $v = 0.7$, and $\phi_v = \pi/4$. (f) Nonsymmorphic D class system described by Hamiltonian (31) in the main text, with parameter values $\mu = 0.4$, $v = 0.6$, $\Delta_s = 0.3$, and $\phi_s = \pi/3$. The introduction of TRS with $T^2 = -1$ induces Kramer's degeneracy in the DIII band structure at the time-reversal invariant points $k = 0$ and $k = \pi/a$, while the D class with nonsymmorphic time-reversal symmetry only has Kramer's degeneracy at $k = \pi/a$.

in

$$H(k) = \begin{pmatrix} \hat{h}(k) & \hat{\Delta}(k) \\ \hat{\Delta}^\dagger(k) & -\hat{h}^T(-k) \end{pmatrix}, \tag{S23}$$

$$\hat{h}(k) = \begin{pmatrix} -\mu+2t_{AA}\cos(ka) & -2iw\sin(ka) \\ 2iw\sin(ka) & -\mu+2t_{AA}\cos(ka) \end{pmatrix}, \tag{S24}$$

$$\hat{\Delta}(k) = \begin{pmatrix} 0 & 2\Delta'_s\cos(ka) \\ -2\Delta'_s\cos(ka) & 0 \end{pmatrix}, \tag{S25}$$

where, if we consider sites A and B to be spin indices, setting $t_3 = -w$ effectively mimics the role of Rashba spin-orbit coupling in related models [S5]. A schematic of the model is shown in Fig. S1(c). In general, the band structure for the first quantized Hamiltonian is an insulator, with energy eigenvalues

$$\begin{aligned} E^2 &= \mu + \Delta'^2_s\cos^2(k) + 4S^2(k) + 4f^2(k) - 4\mu S(k) \pm (4\mu f(k) - 8vS(k)) \\ f(k) &= v\sin(k), \\ S(k) &= t_{AA}\cos(k). \end{aligned}$$

The band structure for this model displays Kramer's degeneracy at the time-reversal invariant points $k = 0$ and $k = \pi/a$, such that the two positive energy bands are degenerate at these points, and, similarly, the two negative energy bands are also degenerate at these points. In position space this manifests as every energy level being doubly degenerate. An example band structure is given in Fig. S2(c). Unlike the BDI class we can not immediately define a winding number by plotting $E_q(k)$, as, by direct calculation, the winding number can be shown to always be zero [S6]. This is not purely a result of the different form of TRS, as we show in Sec.VI of the main text that nonsymmorphic models with $T^2 = -1$ in the AII class can have an associated winding number equivalent. Due to the Kramer's degeneracy we can also not simply use the Majorana formula, Eq. (S11), and instead must use a different form of Fermi surface topological invariant. To calculate the corresponding $\mathbb{Z}_2$ topological index we must first use the chiral symmetry to off-block diagonalize the Hamiltonian (S23) into the Q-matrix (Eq. (23) in the main text) where $Q(k) = U^\dagger_{xy}\mathcal{H}(k)U_{xy}$ with

$$q(k) = \begin{pmatrix} f(k) & g(k) \\ g^*(k) & f(k) \end{pmatrix}, \tag{S26}$$

where

$$\begin{aligned} f(k) &= -\mu - 2t_{AA}\cos(ka), & \text{(S27)} \\ g(k) &= -2iw\sin(ka) - 2i\Delta'_s\cos(ka)\,. & \text{(S28)} \end{aligned}$$

The eigenvalues of the Hamiltonian take values $\pm\lambda_n(k)$ where $n = 1, 2$ with corresponding eigenfunctions of $Q(k)$ defined as $(\chi_n^\pm(k), \rho_n^\pm(k))^T$. It can be shown [S5] from the eigenvalue equation that the eigenfunctions of $Q^2(k)$ are

$$|\Psi_n, \pm\rangle = \begin{pmatrix} \chi_n^\pm \\ \rho_n^\pm \end{pmatrix} = \frac{1}{\sqrt{2}}\begin{pmatrix} u_n \\ \pm q^\dagger(k)u_n/\lambda_n \end{pmatrix}, \tag{S29}$$

where u_n are the normalized eigenfunctions of $q(k)q^\dagger(k)$. This allows us to define the flat band Hamiltonian as

$$\tilde{Q}(k) = \begin{pmatrix} 0 & \tilde{q}(k) \\ \tilde{q}^\dagger(k) & 0 \end{pmatrix} = \sum_{n=1,2}\begin{pmatrix} 0 & u_n u_n^\dagger \frac{q(k)}{\lambda_n} \\ \frac{q^\dagger(k)}{\lambda_n}u_n u_n^\dagger & 0 \end{pmatrix}, \tag{S30}$$

which, when expanded, results in

$$\tilde{q}(k) = \frac{1}{2}\begin{pmatrix} \Upsilon_-(k) + \Upsilon_+(k) & i\Upsilon_-(k) - i\Upsilon_+(k) \\ -i\Upsilon_-(k) + i\Upsilon_+(k) & \Upsilon_-(k) + \Upsilon_+(k) \end{pmatrix} \tag{S31}$$

and

$$\Upsilon_\pm(k) = \frac{-\mu - 2t_{AA}\cos(ka) \pm 2w\sin(ka) + 2i\Delta'_s\cos(ka)}{\sqrt{[-\mu - 2t_{AA}\cos(ka) \pm 2w\sin(ka)]^2 + [2\Delta'_s\cos(ka)]^2}}. \tag{S32}$$

From $\tilde{q}(k)$ we can define the Fermi surface topological invariant as

$$N^{\rm S}_{\rm DIII} = \frac{{\rm Pf}(T^\dagger\tilde{q}(\pi))}{{\rm Pf}(T^\dagger\tilde{q}(0))}\exp\!\left(-\frac{1}{2}\int_0^\pi dk\,{\rm Tr}[\tilde{q}^\dagger(k)\partial_k\tilde{q}(k)]\right), \tag{S33}$$

where $N^{\rm S}_{\rm DIII} = \pm1$ and $T = i\sigma_y$[S5, S7–S9]. From this it can be shown that the system is topologically non-trivial with $N^{\rm S}_{\rm DIII} = -1$ for $|\mu| < 2v$, in which case doubly degenerate MZM are present for a finite system. Otherwise the system is topologically trivial with $N^{\rm S}_{\rm DIII} = 1$ for $|\mu| > 2v$, in which case there are no MZM.

D. Symmorphic CII class with $2\mathbb{Z}$ index and $T^2 = -1$, $C^2 = -1$, $S^2 = 1$

The C classes are defined by their charge conjugation symmetry $C^2 = -1$. In one dimension classes C and CI with $T^2 = 0$ and $T^2 = 1$ are topologically trivial, and have been cataloged for two-band models [S10]. Class CII with $T^2 = -1$ displays Kramer's degeneracy and requires four bands to realize the $2\mathbb{Z}_2$ index. The addition of nonsymmorphic symmetries does not change the topology of any of the C classes, with the exception of an additional unitary symmetry U_+ that anticommutes with the chiral symmetry operator of the CII class [S11], resulting in trivial topology as discussed in Sec. IV of the supplementary material. We write a generic Hamiltonian with two coupled SSH chains such that $C^2 = -1$, the chains are described by staggered hoppings $\pm v$ and $\pm w$ with phases ϕ_v and ϕ_w, and we introduce a coupling parameter Γ between the chains to distinguish from the parameter Δ_s used in previous models. This Hamiltonian corresponds to two coupled SSH chains with complex hopping parameters, with symmetries represented by operators $U_T = \tau_y\sigma_z$, $U_C = \tau_y\sigma_0$, and $U_S = \tau_0\sigma_z$. The bulk Hamiltonian for this system can be written as

$$H(k) = \begin{pmatrix} \hat{h}(k) & \hat{\Delta}(k) \\ \hat{\Delta}^\dagger(k) & -\hat{h}^T(-k) \end{pmatrix}, \tag{S34}$$

$$\hat{h}(k) = \begin{pmatrix} 0 & ve^{i\phi_v} + we^{-ika-i\phi_w} \\ ve^{-i\phi_v} + we^{ika+i\phi_w} & 0 \end{pmatrix}, \tag{S35}$$

$$\hat{\Delta}(k) = \begin{pmatrix} 0 & \Gamma + \Gamma e^{-ika} \\ \Gamma + \Gamma e^{ika} & 0 \end{pmatrix}. \tag{S36}$$

An example band structure of the CII class is given in Fig. S2(d) alongside example band structures of the nonsymmorphic AII and D classes as described by Hamiltonian (28) and Hamiltonian (31) in the main text, respectively. The $2\mathbb{Z}$ index is defined by a winding number. A Q-matrix may be defined by swapping the second and third components, and a winding number defined as the path of the product of its eigenvalues in the complex plane between $-\pi/a < k \leq \pi/a$, denoted $E_q(k)$. The path circles the origin an even number of times, resulting in the $\mathbb{Z}_2$ index. In the case of this minimal model we find that

$$N^{\mathrm{S}}_{\mathrm{CII}} = \begin{cases} 0 & \text{if} \quad |v| > |w|\,, \\ 2 & \text{if} \quad |v| < |w|\,, \end{cases} \tag{S37}$$

which is simply the sum of the winding number of each individual SSH chain [S6].

III. CALCULATION OF $\mathbb{Z}_4$ INDEX IN THE PRESENCE OF HIGHER ORDER PARAMETERS

A. Superconducting order parameter Δ_p

In contrast to the minimal $\mathbb{Z}_4$ model the introduction of further parameters significantly complicates the analytical calculation of the phase transition points between phases $N^{\mathrm{NS}}_{\mathrm{D}} = 1$ and $N^{\mathrm{NS}}_{\mathrm{D}} = 3$, and between phases $N^{\mathrm{NS}}_{\mathrm{D}} = 2$ and $N^{\mathrm{NS}}_{\mathrm{D}} = 4$. However, the Majorana boundary remains unchanged from the minimal model. To see this we take the approach described for the minimal model in Sec. VII of the main text by utilizing the chiral symmetry to create a Q-matrix. The Hamiltonian with the addition of p-wave pairing can be written

$$\mathcal{H}(k) = \begin{pmatrix} \hat{h}(k) & \hat{\Delta}(k) \\ \hat{\Delta}^\dagger(k) & -\hat{h}^T(-k) \end{pmatrix}, \tag{S38}$$

$$\hat{h}(k) = \begin{pmatrix} -\mu & 2v\cos(ka/2) \\ 2v\cos(ka/2) & -\mu \end{pmatrix}, \tag{S39}$$

$$\hat{\Delta}(k) = \begin{pmatrix} 2i\Delta_p\sin(ka) & 2i\Delta_s\sin(ka/2+\phi_s) \\ 2i\Delta_s\sin(ka/2-\phi_s) & 2i\Delta_p\sin(ka) \end{pmatrix}. \tag{S40}$$

We find the resulting Q-matrix (Eq. (23) in the main text) to be $Q(k) = U^\dagger_{xx}\mathcal{H}(k)U_{xx}$ with

$$q(k) = \begin{pmatrix} f(k) & g(k) \\ g(k) & f^*(-k) \end{pmatrix}, \tag{S41}$$

where

$$f(k) = \mu - 2i\Delta_s\sin(ka/2+\phi_s), \tag{S42}$$

$$g(k) = -2v\cos(ka/2) + 2i\Delta_p\sin(ka)\,. \tag{S43}$$

We again characterize the topology by plotting the product of the eigenvalues of $q(k)$ in the complex plane across the Brillouin zone, i.e. for $-\pi \leq ka < \pi$, where, for this system, the product can be written as

$$\begin{aligned} E_q(k) = {} & 4\cos^2(ka/2)(4\Delta_p^2\sin^2(ka/2) + 4i\Delta_p v\sin(ka/2) + \Delta_s^2 - v^2) \\ & + 4i\Delta_s\mu\sin(ka/2)\cos(\phi_s) - 4\Delta_s^2\cos^2(\phi_s) + \mu^2. \end{aligned} \tag{S44}$$

From this, the Majorana number can be found by setting $k = 0$ and determining whether $E_q(0)$ is greater than or less than zero. As expected this yields the same Majorana phase transition as the minimal model. The other phase transitions are not found as simply as those described in Sec VII of the main text, as the complex part of $E_q(k)$ is no longer zero across the Brillouin zone in the cases of $\mu = 0$ or $\cos(\phi_s) = 0$, such that we must consider the value of k when calculating the phase transition points.

To calculate the topology we can utilize the symmetry of $E_q(k)$ about the real axis and consider only one half of the path, between $k = 0$ and $k = \pi$. Separating Eq. (S44) into its complex and imaginary parts we can recognize that both these parts must be equal to zero at the phase transition as they pass through the origin, i.e. $\mathrm{Im}[E_q(k_T)] = 0$ and $\mathrm{Re}[E_q(k_T)] = 0$, where k_T is the value of k at the transition point. As we are only interested in a transition that is dependent on the physical parameters of the system, we rearrange both $\mathrm{Im}[E_q(k_T)] = 0$ and $\mathrm{Re}[E_q(k_T)] = 0$ for k_T and equate them to one another. Rearranging for k_T results in multiple solutions which arise from its periodicity, but discarding solutions with negative k values and squaring each of these solutions results in two equations that can be written as $S_\pm = 0$, where

$$S_\pm = \frac{-2\Delta_s^2+8\Delta_p^2+2v^2\pm2\sqrt{f}}{2\Delta_s^2+8\Delta_p^2-2v^2\mp2\sqrt{f}} + \frac{\Delta_s\mu\cos(\phi_s)+4\Delta_p v}{\Delta_s\mu\cos(\phi_s)}, \tag{S45}$$

where

$$f = -16\Delta_s^2\cos^2(\phi_s)\Delta_p^2 + 16\Delta_p^4 + (8\Delta_s^2 + 4\mu^2 - 8v^2)\Delta_p^2 + (v - \Delta_s)^2(v + \Delta_s)^2. \tag{S46}$$

Solutions to these equations that correspond to real k values in the range $0 \le k < \pi$ correspond to points of topological phase transition between phases $N_{\mathrm{D}}^{\mathrm{NS}} = 2$ and $N_{\mathrm{D}}^{\mathrm{NS}} = 4$, and between phases $N_{\mathrm{D}}^{\mathrm{NS}} = 1$ and $N_{\mathrm{D}}^{\mathrm{NS}} = 3$ in the $\mathbb{Z}_4$ model. In the limit $\Delta_p \to 0$, these solutions approach the minimal model transitions of $\mu = 0$ and $\cos\phi_s = 0$ depending on whether the Majorana number is 1 or -1. We find that

$$S_\pm = \begin{cases} S_+ & \text{if} \quad \lim_{k\to k_T} \mathrm{Re}[E_q(k)] = 0^+ \,, \\ S_- & \text{if} \quad \lim_{k\to k_T} \mathrm{Re}[E_q(k)] = 0^- \,, \end{cases} \tag{S47}$$

while traversing the path from $k = 0$ to $k = \pi$. We note that an identical solution can be obtained through the integral calculation (Eq. (33) in the main text) by tracking the path of the integral and calculating at which point it first crosses the discontinuity at the origin.

B. Hopping parameter t_{AA}

Using a similar methodology as we did for Δ_p we now calculate the topological phase transitions in the presence of an additional hopping parameter between same sites in neighboring unit cells t_{AA}. The resulting Q-matrix (Eq. (23) in the main text) is $Q(k) = U_{xx}^\dagger \mathcal{H}(k) U_{xx}$ with a $q(k)$ of the same form as Eq. (S41), where now

$$f(k) = \mu + 2i\Delta_s\sin(ka/2 + \phi_s) - 2t_{AA}\cos(ka) \tag{S48}$$
$$g(k) = -2v\cos(ka/2)\,. \tag{S49}$$

We again characterize the topology by plotting the product of the eigenvalues of $q(k)$ in the complex plane across the Brillouin zone, i.e. for $-\pi/a \le k < \pi/a$, where, for this system, the product can be written as

$$\begin{aligned} E_q(k) &= 16t_{AA}\cos^4(ka/2) + 4\cos^2(ka/2)(\Delta_s^2 - v^2 - 2\mu t_{AA} - 4t_{AA}^2 - 4i\Delta_s t_{AA}\sin(ka/2)\cos(\phi_s)) \\ &- 4\Delta_s\cos^2(\phi_s) + (\mu + 2t_{AA})^2 + 4i\Delta_s\cos(\phi_s)(\mu + 2t_{AA})\sin(ka/2). \end{aligned} \tag{S50}$$

Unlike for the addition of parameter Δ_p, we find that t_{AA} does change the Majorana number transition. This transition can be found by setting $E_q(0) = 0$, resulting in

$$16t_{AA} + 4(\Delta_s^2 - v^2 - \mu t_{AA} - 4t_{AA}^2) - 4\Delta_s\cos^2(\phi_s) + (\mu + 2t_{AA})^2 = 0\,, \tag{S51}$$

which reduces to the minimal model solution (Eq. (35) in the main text) for $t_{AA} = 0$. The other transition points can be calculated in the same way as described for Δ_p in Sec III A of the supplementary material with solutions $S_\pm$=0, where here

$$S_\pm = \frac{-2\Delta_s^2+8t_{AA}^2+4\mu t_{AA}+2v^2\pm2\sqrt{f}}{2\Delta_s^2+8t_{AA}^2-4\mu t_{AA}-2v^2\mp2\sqrt{f}} + \frac{\mu^2+4t_{AA}^2+4\mu t_{AA}}{\mu^2-4t_{AA}^2}, \tag{S52}$$

where

$$f = (v^2 - \Delta_s^2)(-2\Delta_s^2 + 8t_{AA}^2 + 4\mu t_{AA} + 2v^2) + 16\Delta_s^2 t_{AA}^2 \cos^2\phi_s\,. \tag{S53}$$

Solutions to these equations that correspond to real k values in the range $0 \le k < \pi$ correspond to points of topological phase transition between phases $N_{\mathrm{D}}^{\mathrm{NS}} = 2$ and $N_{\mathrm{D}}^{\mathrm{NS}} = 4$, and between phases $N_{\mathrm{D}}^{\mathrm{NS}} = 1$ and $N_{\mathrm{D}}^{\mathrm{NS}} = 3$ in the $\mathbb{Z}_4$ model. In the limit $t_{AA} \to 0$, these solutions approach the minimal model transitions of $\mu = 0$ and $\cos\phi_s = 0$, depending on whether the Majorana number is 0 or 1. The determining factor on which of the two equations are used is identical to the case for the inclusion of Δ_p pairing, Eq. (S47). We note that an identical solution can be obtained through the integral calculation (Eq. (33) in the main text) by tracking the path of the integral and calculating at which point it first crosses the discontinuity at the origin.

IV. C CLASSES WITH ADDITIONAL NONSYMMORPHIC UNITARY SYMMETRY

By setting the components of Hamiltonian (S34) as $w = v$ and $\phi_w = \phi_v$ we obtain the Hamiltonian

$$H(k) = \begin{pmatrix} \hat{h}(k) & \hat{\Delta}(k) \\ \hat{\Delta}^\dagger(k) & -\hat{h}^T(-k) \end{pmatrix}, \tag{S54}$$

$$\hat{h}(k) = \begin{pmatrix} 0 & ve^{i\phi_v} + ve^{-ika-i\phi_v} \\ ve^{-i\phi_v} + ve^{ika+i\phi_v} & 0 \end{pmatrix}, \tag{S55}$$

$$\hat{\Delta}(k) = \begin{pmatrix} 0 & \Gamma + \Gamma e^{-ika} \\ \Gamma + \Gamma e^{ika} & 0 \end{pmatrix}. \tag{S56}$$

In addition to the symmorphic symmetries with $U_T = \tau_y\sigma_z$, $U_C = \tau_y\sigma_0$, and $U_S = \tau_0\sigma_z$ this Hamiltonian also has a nonsymmorphic unitary symmetry $U_+ = U_k(k,s)(\tau_z\sigma_x)$, resulting in a path

$$\begin{aligned} E_q(k) &= -v^2 - \Gamma^2 - (\Gamma^2 + v^2)\cos(2ka) \\ &+ 2(\Gamma^2 - v^2\cos(2\phi_v))\cos(ka) + i(\Gamma^2 + v^2)\sin(2ka) \\ &- 2i(\Gamma^2 - v^2\cos(2\phi_v))\sin(ka)\,. \end{aligned} \tag{S57}$$

Solving $\mathrm{Re}[E_q(k)] = 0$ and $\mathrm{Im}[E_q(k)] = 0$ for k we find that they share an identical solution

$$k_T = \pm\frac{v^2(1 - \cos(2\phi_v)) + 2\Gamma^2 + v^2}{v^2(1 + \cos(2\phi_v))}, \tag{S58}$$

which guarantees a crossing of the origin at $k = k_T$, forcing a band gap closing and eliminating the winding number.

This may also be understood by the block diagonalization of the Hamiltonian (S54) through the unitary transformation $H_{\mathrm{BD}} = U_{zx}(k)^\dagger H(k) U_{zx}(k)$ where

$$U_{zx} = \frac{1}{\sqrt{2}}\begin{pmatrix} 0 & -e^{-ika/2} & 0 & e^{-ika/2} \\ 0 & 1 & 0 & 1 \\ e^{-ika/2} & 0 & -e^{-ika/2} & 0 \\ 1 & 0 & 1 & 0 \end{pmatrix}, \tag{S59}$$

such that

$$H_{\mathrm{B}}(k) = \begin{pmatrix} H_1(k) & 0 \\ 0 & H_2(k) \end{pmatrix}, \tag{S60}$$

$$H_1(k) = \begin{pmatrix} 2v\cos(ka/2 - \phi_v) & -2i\Gamma\sin(ka/2) \\ 2i\Gamma\sin(ka/2) & 2v\cos(ka/2 + \phi_v) \end{pmatrix}, \tag{S61}$$

$$H_2(k) = \begin{pmatrix} -2v\cos(ka/2 - \phi_v) & 2i\Gamma\sin(ka/2) \\ -2i\Gamma\sin(ka/2) & -2v\cos(ka/2 + \phi_v) \end{pmatrix}. \tag{S62}$$

The eigenvalues for $H_1(k)$ and $H_2(k)$ are degenerate with each other, and both Hamiltonians have $T^2 = -1$ with $U_T = \sigma_y$ such that Kramer's degeneracy forces the band gap to close and ensuring trivial topology.

[S1] C. Chiu, J. C. Y. Teo, A. P. Schnyder, and S. Ryu, Classification of topological quantum matter with symmetries Rev. Mod. Phys. **88**, 035005 (2016).

[S2] M. Sato and Y. Ando, Topological superconductors: a review, Rep. Prog. Phys. **80**, 076501 (2017).
[S3] H.-M. Guo, A brief review on one-dimensional topological insulators and superconductors, Sci. China Phys. Mech. **59**, 637401 (2016).
[S4] A. Y. Kitaev, Unpaired Majorana fermions in quantum wires, Phys.-Usp. **44**, 131 (2001).
[S5] C. L. M. Wong and K. T. Law, Majorana Kramers doublets in $d_{x^2} - d_{y^2}$-wave superconductors with Rashba spin-orbit coupling, Phys. Rev. B **86**, 184516 (2012).
[S6] P. Matveeva, T. Hewitt, D. Liu, K. Reddy, D. Gutman, and Sam T. Carr, One-dimensional noninteracting topological insulators with chiral symmetry Phys. Rev. B **107**, 075422 (2023).
[S7] X. L. Qi, Taylor, L. Hughes, and S. C. Zhang, Topological invariants for the Fermi surface of a time-reversal-invariant superconductor, Phys. Rev. B **81**, 134508 (2010).
[S8] J. C. Y. Teo and C. L. Kane, Topological defects and gapless modes in insulators and superconductors, Phys. Rev. B **82**, 115120 (2010).
[S9] A. P. Schnyder and S. Ryu, Topological phases and surface flat bands in superconductors without inversion symmetry, Phys. Rev. B **84**, 060504(R) (2011).
[S10] E. McCann, Catalog of noninteracting tight-binding models with two energy bands in one dimension, Phys. Rev. B **107**, 245401 (2023).
[S11] K. Shiozaki, M. Sato, and K. Gomi, Topology of nonsymmorphic crystalline insulators and superconductors, Phys. Rev. B **93**, 195413 (2016).